EXCITATION OF PICOSECOND MAGNETISATION DYNAMICS BY SPIN TRANSFER TORQUE

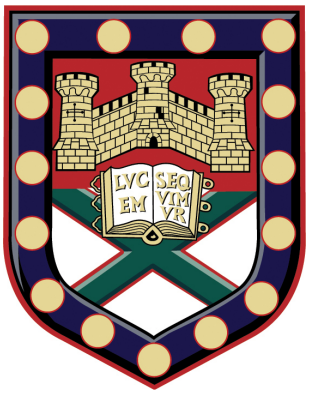

Submitted by

CHLOE MICHELLE SPICER

to the

UNIVERSITY OF EXETER

as a thesis for the degree of

DOCTOR OF PHILOSOPHY IN PHYSICS

in

AUGUST 2018

I certify that all material in this thesis which is not my own work has been identified and that no material has previously been submitted and approved for the award of a degree by this or any other University.

. . . . . .

Chloe Michelle Spicer

Following publication the author of this thesis underwent a name change. While the authorship here is in her preferred name, published articles have been unchanged and are referenced as they appear with the publishers.

Abstract

This thesis presents the results from investigations of ultrafast magnetisation dynamics driven by pure spin currents. Spin orbit coupling in heavy metal layers - such as tungsten, tantalum or platinum - allows for the generation of pure spin currents, whereby spin up and spin down electrons move in opposite directions. Hence, a flow of angular momentum can be controlled through the manipulation of charge current through a heavy metal layer. When a spin current is injected into a ferromagnet, a torque is exerted on its magnetisation, with the potential to induce a wide variety of ultrafast dynamics. The experimental investigation of these phenomena employed a variety of high-frequency electrical techniques and time-resolved scanning Kerr microscopy (TRSKM) methods. In addition, various simulative and analytical approaches were used to gain insight into the underlying mechanisms.

Spin Hall nano-oscillators (SHNOs) have recently been shown to support a tunable GHz spin wave 'bullet' under injection of direct current (DC), making it an exciting candidate for microwave communication applications. This thesis will show how TRKSM can be used to measure the torques within these devices, revealing that radio frequency (RF) current does not possess the same distribution as the DC. The competition between self-inductance and focusing within the device geometry results in a modified distribution of spin current. Further TRSKM measurements show the modified torque landscape to promote the mobility of the 'bullet' within the magnetic layer.

Devices that exploit spin currents for magnetisation reversal have received interest from academia and industry for their potential use as memory elements. The perpendicular magnetic anisotropy present in Ta/CoFeB/MgO leads to lower write currents and higher thermal stability. However, ultrafast processes have not been previously observed in such devices. TRSKM measurements of Hall bar devices were compared with a macrospin model to understand the underlying torques, and to investigate the conditions required to promote switching. Square elements built from the same stack structure exhibited contrasting static and dynamic behaviour. Pulsed currents drove differing dynamics at the edge and center of the device, while enabling the realignment of magnetic domains. The domains themselves could be driven directly by the spin current leading to domain wall dynamics. Measurements with a bipolar electrical pulse demonstrated that meta-stable switching can be achieved in micron-scale elements.

Acknowledgements

I must first extend my gratitude to the efforts of my first supervisor Prof. Rob Hicken, not only for his offer of a PhD but also for his unwavering support. His patience and encouragement in everything from presentations to papers have been vital to my work, and simply i don't think i could have had a better supervisor. I am also thankful for the opportunity he has provided to present at conferences and attend research trips. I would also like to thank my second supervisor Prof. Volodymyr Kruglyak for his knowledge and sense of humour, without whom this journey would have been far more difficult.

I would also like to acknowledge the assistance and influence of several individuals from the Exeter magnetic materials group. To Dr Paul Keatley I am thankful for his guidance in all experimental and academic matters. To Dr Tom Loughran I'm grateful for his help with all things programming and simulation, as well as being a great source of ideas and jokes on matters academic or otherwise. To Dr Rémy Soucaille for his assistance with literature and analysis, as well as his sociable attitude. Dr Rob Valkass for his help with all kinds of technical matters, as well as his sense of humour. Dr Chris Durrant for his patience with allowing me to work on his own samples, as well as his support. To Nick Bukin, Cameron Gallagher, and Dr Erick Burgos I'm grateful for their continued friendship and allowing me to 'vent' about a number of problems over the years. Outside of the group I would also like to thank Dr Ian Hooper, Dr Anja Roeding of the Metamaterials CDT for their assistance and support on the various challenges that arose over the last 4 years. I am also thankful to Rosie Dixon, for her help with various administrative matters

as well as her level headed and amiability. I am also grateful to the efforts of Nick Cole, Adam Woodgate, Richard Taylor and all members of the workshop team for dealing with all manner of requests and absurd turnarounds, while maintaining their cheerfulness.

It is also important I thank the various collaborators who have made this work possible. The university of Gothenburg who very kindly fabricated the SHNOs and for accommodating me and permitting use of their Ragnarök cluster. In particular to Dr Mykola Dvornik, Dr Ahmad Awad, and Prof. Johan Åkerman for their continued support in understanding these samples. In addition I would like to thank Professor Gang Xiao and his research group at Brown University, for the fabrication of the various Ta/CoFeB/MgO samples used in this thesis.

Finally I must take time to thank all those who while they made little direct contribution to this work, made the world of difference to my time at Exeter. While it is impossible to itemise every highlight of my time at Exeter and give credit, I believe it is equally a disservice not to try. I would be remiss not to thank my parents Alan and Clare for their support during my PhD, when I've struggled with keeping on top of life they've always found a way to help. I have also had the privilege to make a multitude of friends from all walks of life. In particular I need to thank those who have put up living with me over the last 8 years, who gave distractions when I needed distractions and laughs when I needed laughs. To the Rotten Apple Orchestra, 7 years is too short a time to play with such fine musicians, but you would think by now we would at least be able to keep rehearsals on track. To the Aftermath film group, thank you for trusting me to hold a boom over all of your heads, and for being such great creative people to work with. Last but no means least my long time friend John (or Selly, depending who you ask), who tactfully employed computer games and wit to put any troubles I've had into perspective.

I gratefully acknowledge financial support from the Engineering and Physical Sciences Research Council (EPSRC) of the United Kingdom, via the EPSRC Centre for Doctoral Training in Metamaterials (Grant No. EP/L015331/1).

All data created during this research are available from the University of Exeter's institutional repository.

Contents

Contents 11

List of Figures 15

List of Tables 29

List of Publications 35

List of Acronyms 38

List of Symbols 40

1 Introduction 43

2 Background material 49

2.1 Introduction 49

2.2 A Semi-classical Origin of Magnetism 49

2.3 Ferromagnetic free energy contributions 51

2.3.1 Exchange Energy 52

2.3.2 Zeeman Energy 55

2.3.3 Magnetostatic Energy 56

2.3.4 Magnetic Anisotropy 57

2.4 Magnetic Domains 58

2.5 Precessional Dynamics 60

2.5.1 Ferromagnetic Resonance 60

2.5.2 Spin waves . . . 62
2.6 Anisotropic Magneto-resistance . . . 63
2.7 Spin-Orbit torques . . . 64
2.7.1 Anomalous Hall Effect . . . 64
2.7.2 Spin Hall Effect . . . 64
2.7.3 Rashba Effect . . . 67
2.7.4 Spin Transfer Torque & its Application . . . 68

3 Experimental Techniques **71**
3.1 Measurement of Spin-Torque FMR . . . 71
3.2 Analytical Expressions for FMR . . . 74
3.3 Magneto-transport techniques . . . 78
3.4 Magneto-Optical Kerr Effect . . . 79
3.5 Time-Resolved Scanning Kerr Microscopy . . . 82
3.5.1 Optical Setup . . . 82
3.5.2 Electrical Equipment . . . 85
3.5.3 Discussion & Summary . . . 89
3.6 Methods for Micromagnetic simulations . . . 91
3.6.1 Introduction . . . 91
3.6.2 Calculating Current and Oersted field distributions . . . 93
3.6.3 Calculating the magnetic response . . . 94
3.7 X-ray Photo-Emission Electron Microscopy . . . 95

4 Spatial Mapping of Torques within a Spin Hall Nano-oscillator **97**
4.1 Introduction . . . 97
4.2 Methodology . . . 98
4.3 Results . . . 101
4.4 Discussion . . . 107
4.5 Summary . . . 108

5 Time resolved imaging of the non-linear bullet mode within an injection-locked spin Hall nano-oscillator **109**

5.1 Introduction . . . 109

5.2 Experimental method . . . 111

5.3 Results . . . 113

5.3.1 Electrical Characterization . . . 113

5.3.2 TRSKM Measurements of the full magnetic response . . . 115

5.3.3 Micromagnetics . . . 117

5.3.4 TRSKM Measurements with increased I_{DC} . . . 123

5.4 Summary . . . 125

6 Current-induced picosecond magnetisation dynamics in Ta/CoFeB/MgO Hall Bars **127**

6.1 Introduction . . . 127

6.2 Experimental Set-up . . . 129

6.3 Theoretical Framework . . . 129

6.4 Experiment and Modelling . . . 130

6.5 Summary . . . 140

7 Magnetisation Dynamics in Ta/CoFeB/MgO Elements driven by Unipolar and Bipolar Current Pulses **143**

7.1 Introduction . . . 143

7.2 Device Specification . . . 144

7.3 Static measurements . . . 145

7.4 Unipolar Pulse . . . 149

7.5 Bi-polar pulse . . . 160

7.6 XPEEM measurements . . . 164

7.6.1 Motivation . . . 164

7.6.2 Results . . . 165

7.6.3 Discussion . . . 169

7.7 Summary 171

8 Summary and Future Work **173**

Bibliography **177**

List of Figures

2.1 Classical schematic of an atom. Electron of charge $-e$ orbiting with distance r and velocity v, angular momentum l generating magnetisation m. 50

2.2 Schematic of Bloch and Néel walls present within materials of perpendicular and in-plane magnetic anisotropy. Domain wall is shown in the $\hat{\boldsymbol{y}} - \hat{\boldsymbol{z}}$ plane, for Bloch walls magnetisation rotates within this plane whereas rotation is normal to the plane for Néel walls. 59

2.3 a) Simulated vortex domain structure within a disk (5 nm thick, and 4 μm diameter) from Mumax3, colourscale and arrows represent the in-plane direction of magnetisation. b) Wide field Kerr microsopy image of magnetic domains in a Garnet film, grayscale representing the out of plane component of $\boldsymbol{M}$, reproduced from [23]. 60

2.4 Schematic representation of a spin wave. A line of spins (represented with arrows) with successive increase in phase of precession about the dashed line, for an separation of a between each moment. The wavelength depicted is $9a$. 62

2.5 Schematic depicting mechanisms that contribute to both the Spin Hall and Anomalous Hall effects. a) Spin Skew Scattering, the spin orbit coupling gives rise to an effective field gradient, represented by the green arrows. b) Side jump occurs due to spin-dependant acceleration and deceleration (represented by green arrows) during scattering from spin-orbit coupled impurities. c) Intrinsic Spin Hall Effects, which occur between scattering events. Reproduced from [52] 66
2.6 Depiction of the terms in equations (2.40) and (2.41), indicating the direction of spin and field torques acting on the magnetisation. 69
2.7 Schematic of a SHE device, consists of bi-layer of heavy metal and ferromagnet and electrical contacts. Charge current (J_{charge}) flowing through the heavy metal layer undergoes the SHE generating a vertical spin current (J_{spin}) into the ferromagnet layer. 70

3.1 Plot of terms in equation (3.2) for a general case, a) showing the separate contributions of Spin Torque and Oersted Field, and b) a curve with the terms combined. For A = B = 1, Δ = 75 Oe, and H_0 = 400 Oe. 72
3.2 Experimental setup for the measurement of Spin-torque FMR. Microwave Synthesiser supplies RF current to sample generating both spin torques and an Oersted field, DC mixing voltage can be simultaneously read via a bias tee by a lock-in amplifier. Signal generator supplies a reference frequency of 3.14... kHz, RF current undergoes amplitude modulated at this frequency. 73

3.3 Diagram of a microwave spectroscopy setup for simultaneously supplying and measuring both DC and RF currents, with an electromagnet to drive a bias field. Nano-volt meter and current source are both connected to the inductive (DC) arm of the bias tee and grounded, enabling the injection of current and measurement of DC voltage across the sample. A circulator separates the flow of RF current, such that emission from the microwave synthesiser is passed to the device, while any emission from the sample is passed on to a spectrum analyser (via a +25 dB amplifier). 79

3.4 Diagram of the three MOKE geometries. a) Polar MOKE, where the magnetisation points along the surface normal, is maximised for small angles of incidence. b) Longitudinal MOKE, where magnetisation lies parallel to the surface and *within* the plane of incidence. c) Transverse MOKE, where magnetisation is also parallel to the surface but *perpendicular* to the plane of incidence, is also maximised for large angles of incidence. It is only observed for P-polarised light, where a change in amplitude can be measured. Reproduced from [71]. 81

3.5 Schematic for the optical components in the TRSKM. Laser pulses are monitored with a laser spectrum analyser. Second harmonic generator crystal provides two wavelengths for measurement, separate colours are used to show the path of blue (400 nm) and 'red' (800 nm) beams. Delay stage allows the laser pulses to be delayed relative to electrical pulses. Wavelength splitter, beam stop, and flip mirrors allow the wavelength to be selected before beam enters a beam expander (in this figure the 'red' beam has been selected). Beam expander, aperture and neutral density filter prepare the beam's power and spot size before entering the microscope. Within the microscope, the beam passes through a polariser and is focused onto the sample. The beam is positioned on the sample using a piezoelectric stage, and a bridge detector measures the change in polarisation of the reflected light. 83

3.6 Diagram of focused optical probe for resolving in-plane magnetisation. Beam is divided into four quadrants, a, b, c, and d. Upon reflection these quadrants undergo the longitudinal Kerr rotation due to $M_{\perp}$ and $m_{||}$ componants of magnetisation $\boldsymbol{M}$. Reproduced from [72] 85

3.7 Diagram of optical and electrical equipment for TRSKM to drive and observe injection locked spin torque oscillators. Electrical equipment is similar to the magneto-transport in section 3.3. In addition, the RF current from the synthesiser can be monitored on an oscilloscope for phase drift and amplitude. The laser and synthesiser are locked to the same clock, while a reference frequency is supplied by a function generator (not shown) at 3.1415... kHz. 87

3.8 Diagram of TRSKM electrical equipment to inject electrical pulses into a sample. Pulse generator is synchronised to the laser with a clock, and modulated (or gated) at the reference frequency. The injected pulse is monitored on an Oscilloscope. 88

3.9 Diagram of additional optics and electrical equipment required to observe dynamics induced by bi-polar electrical pulse with large time delay. Laser repetition rate is reduced by a pulse picker to a specified number of pulses, synchronised to the pulsed laser. A photodiode serves as a new clock to trigger electronics. The electrical delay generator is gated at the reference frequency, and subsequently triggers a pulse generator. The electrical pulse is converted into a bi-polar pulse with the components shown in the inset (a). 90

3.10 Comparison of GPUs, for a SHNO with 400 $\times$ 400 cells of increasing DC (leading to increased the magnetisation dynamics) 93

4.1 (a) SEM image of an SHNO showing electrode separation d, directions of the DC charge current I_{DC}, average polarization $\hat{\sigma}$ of the spin current injected into the Py layer, and field $\boldsymbol{H}$ orientated at angle θ_H relative to the x axis. COMSOL simulations for I_{DC} = 4 mA and d= 200 nm are shown for (b) current density $\boldsymbol{J}$ within the Pt layer, (c) in-plane Oersted field within the Py layer that has magnitude $\sqrt{h_x^2 + h_z^2}$, and (d), out of plane Oersted field h_y within the Py layer. The arrows and grayscale indicate the direction and normalized magnitude respectively. 99

4.2 (a) Dependence of mixing voltage V_{mix} upon field H_{ext} applied at $\theta_H = 150^\circ$. The continuous curve is fit to equation 4.2. (b) Polar Kerr rotation curves recorded with the optical spot between the tips of the NC for three values of the phase φ. (c) Polar Kerr (closed circles) and V_{mix} (open squares) resonance curves recorded with the optical probe 1μm to the right of centre, for different values of θ_H. (d) Polar Kerr rotation and intensity images for $\theta_H = 90^\circ$ and $H_{ext} = 75$ Oe for φ values in the range 0 to 180°. The current had frequency of 2 GHz and amplitude of 2.8, 1.3, 3.2 and 4.0 mA in (a), (b), (c) and (d) respectively. The NC separation $d =$ 240 nm in (a) and (b), and 140 nm in (c) and (d) 103

4.3 Optical resonance curves acquired with the optical spot positioned 1 μm to either side of the NCs. The phase set on the microwave synthesizer φ_{RF}, and the phase of the current at the sample φ are shown next to the curves. The external field was applied in the vertical direction ($\theta_H = 90°$), while the current had frequency of 2 GHz and amplitude of 1.3 mA. The curves have been offset in the vertical direction for clarity. 105

4.4 a) Spatial variation of $H_\perp$ and $H_{||}$ along the horizontal line passing through the middle of the disk. Values obtained from electrical STT-FMR are shown by the dashed line with the error indicated by the gray shading. The injected RF current had frequency f = 2 GHz and amplitude I_{RF} = 1.3 mA, while the static field was applied at θ_H = 90°. b) $H_\perp$ and the antisymmetric/symmetric parts of $H_{||}$ are plotted together with the current and Oersted field from Figure 4.1. c) Polar Kerr image acquired for $\varphi = 0°$, I_{RF} = 4 mA and H_{ext} = 75 Oe is presented next to the calculated distribution of h_x. Symmetric and antisymmetric parts of the polar Kerr data acquired at $\varphi = 90°$, are presented next to the vertical component of the current density J_z and the out of plane Oersted field h_y. The calculated images were convolved with a Gaussian profile of 870 nm half maximum diameter. The NC separation d was 240 nm for a and b, and 140 nm for c. 106

5.1 a) SEM image of a typical SHNO, where I is the injected current, σ the corresponding spin polarization, d the NC separation, and H the magnetic field applied at angle θ_H. b) Voltage Spectral Density (VSD) of microwave emission from a SHNO with $d = 240$ nm at fixed magnetic field H = 650 Oe and $\theta_H = 210°$ for different values of I_{DC}. c) Emission excited from a SHNO with $d = 180$ nm for I_{DC} = 18 mA, with magnetic field H orientated at θ_H =150°. Red squares show resonance fields from STT-FMR, solid black curve shows the fit to the Kittel equation, acquired from the same device. d) Emission for a device with d = 240 nm when I_{DC} = 18.5 mA and I_{RF} has amplitude of 3.5 mA and frequency of 12 GHz. Enhancement of locking region shown as inset. 112

5.2 Magneto-transport measurements illustrating the symmetry of the bullet mode, emission shown for a) positive I_{DC} and b) negative I_{DC}. Excitation of the bullet mode requires the external field to be applied close to 90° to the direction of current. In addition, the vanishing AMR and angles θ_H ~0° and 180° suppresses the RF emission, hence precession is only observed for intermediate field angles. 114

5.3 Microwave emission observed when Injection locking at 6 GHz for different I_{RF} values (shown at top left of each plot). The red dashed line shows the maximum emission for I_{RF} = 0 mA. 115

5.4 a) TRSKM images acquired from the polar (out of plane), horizontal, vertical and reflected intensity channels of the vector bridge detector for a SHNO with d = 200 nm, H = 650 Oe, $\theta_H = 210°$, and I_{RF} = 1.4 mA at 6 GHz frequency. $I_{DC} = 16$ mA and 0 mA in the upper and lower panels respectively. (b) The difference of the upper and lower images from (a) is shown, revealing contrast due to the presence of I_{DC} only. Each image shows a 5 μm square region. 116

5.5 a) TRSKM images acquired for different values of the phase of the injected RF current for a SHNO device with tip separation d = 240 nm. In each case an image acquired at I_{DC} = 15 mA has been subtracted from an imaged acquired at I_{DC} = 18 mA. In each case I_{RF} = 0.8 mA, while a static field of H = 650 Oe was applied at an angle θ_H=210° as defined within the main text. Each image shows a 4 μm square field of view. 116

5.6 a) Typical time trace from a simulation of the spatially averaged horizontal magnetisation component. Vertical red lines indicate periods of instability. b) Selected time resolved images of the out of plane magnetisation component from the period of instability shown in (a). . 118

5.7 Power spectrum of the spatially averaged out of plane component of magnetisation for a SHNO with a field of 1 kOe applied θ_H=210°. . . . 120

5.8 Spectral images of both bullet and field localized modes with cross-sections through the images (blue dashed lines). 120

5.9 a) Simulated magnetisation profile at different phase values within the cycle of auto-oscillation. The arrows indicate the projection of the magnetisation within the plane, while the grayscale represents the out of plane component. The images show the bullet mode with $\sim$ 70 nm diameter at the centre of the device. Lower right panel contains the time-averaged and indicates two areas of interest, (i) the area immediately outside the bullet, and (ii) the bullet mode's core. b) Trajectories of the magnetisation for different points on the x axis as indicated in (a), arrows show direction of precession over 1 cycle of oscillation. Trace for x = -35 nm presented in both (i) and (ii) to aid comparison between precession inside and outside of the bullet. 121

5.10 Schematic to illustrate the artefact that generates contrast in the horizontal and vertical channels. Arrows indicate the direction of propagation of rays. 121

5.11 a) Polar TRSKM images acquired for different I_{DC} values with the phase of I_{RF} fixed. b) Maximum absolute values of polar Kerr rotation extracted from the images in (a). (c) TRSKM images from (a) after subtraction of the $I_{DC} = 0$ mA image. All images were recorded from a SHNO with d = 240 nm, with I_{RF} = 0.8 mA, H = 650 Oe and $\theta_H = 210°$. 123

5.12 a) Cross sections through figure 5.11c b) estimated horizontal FWHM of the observed bullet, gray box indicates the optical beam spot size. . 124

6.1 a) Schematic of the Hall bar and co-ordinate system used, with beam spot position and direction of positive current indicated. Individual and averaged measured hysteresis loops for b) $\boldsymbol{H}||\hat{\boldsymbol{x}}$, and c) $\boldsymbol{H}||\hat{\boldsymbol{y}}$. d) Calculated loops are shown for $\boldsymbol{H}$ canted out of the plane by an angle of 5°, assuming M = 1000 emu/cm^3, K_1 = 7.0 $\times 10^6$ erg/cm^3, and K_2 = 0 and 0.15$\times 10^6$ erg/cm^3. 131

6.2 a) Pulse reflected from the Hall bar device (right), and from the end of the open circuit connecting cable when detached from the device (left). b) Time dependent polar MOKE for static field $\boldsymbol{H}||\hat{\boldsymbol{x}}$ and $\boldsymbol{H}||\hat{\boldsymbol{y}}$. The black dots are the experimental points while the black line is a guide to the eye composed of a transient background (blue line) and a damped oscillation (red line). The black curve has the form $f_{pulse}(t)[asin(2\pi ft + \phi) + b]$ with amplitudes a and b, frequency f, and phase ϕ. The pulse profile has the form $f_{pulse}(t) = erf(t/T_1)exp(-t/T_2)$ with rise and decay times T_1 = 50 ps and T_2 = 290 ps respectively. For $\boldsymbol{H}||\hat{\boldsymbol{y}}$, $a = 0.08$, $b = 0.06$, and $\phi = 42°$, while for $\boldsymbol{H}||\hat{\boldsymbol{x}}$, $a = 0.06$, $b = 0.12$, and $\phi = -145°$. . 133

6.3 Comparison of experimental (red) and simulated (blue) out of plane magnetisation component with a static field H = 900 Oe, applied along either the $\hat{\boldsymbol{x}}$ or $\hat{\boldsymbol{y}}$ axes, for all possible combinations of field and current polarity. The parameter values used within the simulations are described within the main text. 135

6.4 Comparison of simulated and experimental normalized out of plane magnetisation component m_z for different values of H, the static applied field. a) experiment and b) simulation for $\boldsymbol{H}||\hat{\boldsymbol{x}}$. c) experiment and d) simulation for $\boldsymbol{H}||\hat{\boldsymbol{y}}$ direction. The simulations assume the same material parameter values as used in figure 6.3, and that are described within the main text. 137

6.5 Schematic depicting orientation of slow transient background (which lies in the $\boldsymbol{M} \times \hat{\boldsymbol{y}}$ direction), for high and low H in both the $\hat{\boldsymbol{x}}$ and $\hat{\boldsymbol{y}}$ directions. Demonstrating that significant out-of-plane slow transient only occurs for high fields close to the $\hat{\boldsymbol{x}}$ axis. Oersted field from pulsed current is also shown, and lies in the the $-\hat{\boldsymbol{y}}$ direction for all cases. . . 138

6.6 Macrospin simulations of current-induced magnetisation reversal. a) Minimum current density required for magnetisation reversal for the case of no bias field (black circle), $\boldsymbol{H}||\hat{\boldsymbol{x}}$ (red triangles), and $\boldsymbol{H}||\hat{\boldsymbol{y}}$ (blue squares). b) Switching times $t_{switch,1}$ and $t_{switch,2}$ associated with the minimum current density in (a). Magnetisation trajectories are plotted for the case of c) no bias field, (d) H = 250 Oe applied parallel to $\hat{\boldsymbol{x}}$ and (e) H = 250 Oe applied parallel to $\hat{\boldsymbol{y}}$. Open symbols are placed at intervals of 0.2 ns. 138

6.7 Macrospin simulations of current-induced magnetisation reversal, for the injection of a second electrical pulse with the same temporal profile. Solid blue line shows the m_z component of magnetisation, dashed black line shows the amplitude of spin current injected. Simulations were carried out for three static field configurations a) H = 0 Oe, b) $\boldsymbol{H}||\hat{\boldsymbol{x}}$ with a magnitude of 250 Oe, and c) $\boldsymbol{H}||\hat{\boldsymbol{y}}$ with a magnitude of 250 Oe. 140

6.8 Schematic depicting the direction of effective fields due to anti-damping STT and Oersted fields. For two stable states (m_{state1} and m_{state2}) canted away from the vertical due to a static field applied in the a) $\hat{\boldsymbol{x}}$, and b) $\hat{\boldsymbol{y}}$ directions. 141

7.1 Stack structure where Au contacts overlap with the Ta under layer to ensure a low resistance electrical connection. Wafers were fabricated for all combinations of Si resistivity and Ta underlayer thickness, as described within main text. 145

7.2 Schematic of the device on which TRSKM measurements were made. Large gold tracks connect to high frequency probes to deliver current to the CoFeB elements (inset). For this device, elements consist of squares of different length. 146

7.3 Magnetic domain nucleation and expulsion in 10×10 μm square element for increasing and decreasing fields applied in the a) $\hat{\boldsymbol{x}}$ and b) $\hat{\boldsymbol{y}}$ directions. Prior to measurement, a saturation field of -1500 Oe was applied in the same direction. Dashed arrows indicated the order of applied field values. (Also found in reference [149]) 147

7.4 Vector resolved hysteresis loops for the 10 μm element, where the CPW signal line lies in the $\hat{\boldsymbol{x}}$ direction. For a, b & c $\boldsymbol{H}$ lies in the $\hat{\boldsymbol{y}}$ direction, whereas in c) d) & e) $\boldsymbol{H}$ lies in the $\hat{\boldsymbol{x}}$ direction. Measurements were carried out with the optical spot in the center of the device. (Also found in reference [149]) 149

7.5 Remanent domain states observed in nominally square shaped elements of different size. Multi-domain states can be observed for elements down to 2.8 μm length, after which the magnetisation appears uniform. 149

7.6 Vector TRSKM measurements for the beam positioned at a) the center, b) top edge and c) left edge of the element. With a static field of 500 Oe applied in the $\hat{x}$ direction. For for d the field was applied in the $\hat{y}$ direction with the laser probe at the center of the element. Dashed lines indicate time delays corresponding to TRSKM images in figure 7.7. (Also found in reference [149]) 151
7.7 TRSKM observations of the dynamics present within 10 $\times$ 10 μm CoFeB elements at the fixed time delays shown (in ns) for a field of 500 Oe applied parallel to a) $\hat{x}$ and b) $\hat{y}$. (Also found in reference [149]) 152
7.8 TRSKM measurments from the center of the 10 $\times$ 10 μm element for a field of 100 Oe || $\hat{y}$. This measurement was used to identify noteworthy features (dashed lines) for later TRSKM imaging measurements in figure 7.9. (Also found in reference [149]) 154
7.9 Static and dynamic magnetic images of Ta/CoFeB/MgO 10$\times$10 μm elements at the stated delay times (in ns) also indicated in figure 7.8, for a 100 Oe field applied parallel to a) $\hat{x}$ and b) $\hat{y}$. For each time delay, a static polar Kerr image was simultaneously obtained showing the domain structure present during measurement. (Also found in reference [149]) 155
7.10 Schematic representation of torques calculated within table 7.1. 158
7.11 TRSKM measurements at a time delay of 0.43 ns, from figure 7.11, for $\boldsymbol{H}$ || $\hat{x}$ & $\hat{y}$. The static domain structure is highlighted in red within all images. (Also found in reference [149]) 158
7.12 a) Electrical pulse profile determined by measurement of the transmitted pulse, with calculated current density and Oersted field. The resulting magnetisation dynamics were measured for static fields of b) 150 Oe, c) 200 Oe, d) 300 Oe, e) 400 Oe, f) 500 Oe applied in the $\hat{x}$ direction. 160

7.13 Simulations to replicate meta-stable state behaviour, assuming K_1=7.0$\times$10^6 erg/cm^3, K_2=1$\times$10^4 erg/cm^3 for H = 1.3 kOe applied parallel to the the $\hat{x}$ direction. a) hysteresis loop with dashed line to indicate 1.3 kOe, b) change of m_z in response to bi-polar pulse of twice the amplitude in figure 7.12a. The gray line shows the full time-dependant response, with the red line showing a moving average, c) dynamic response projected onto a sphere. 162

7.14 TRSKM images of the out-of-plane dynamics within the 10 μm element for a field of 300 Oe applied in the $\hat{x}$ direction. 163

7.15 Polar MOKE signals acquired from elements of different size in response to the bi-polar pulse, with a static field of 150 Oe applied parallel to $\hat{x}$, and with the optical probe in the center of each element. 164

7.16 XPEEM data from samples grown on a high resistivity Si wafer. a) Difference of images acquired at x-ray energies of 700 eV and 707 eV. Square elements can be seen at the edge of a gold track b) cross-section taken along the long red line in a. 166

7.17 Data obtained from the sample grown on a low resistivity Si wafer. a) image at 707 eV depicting square elements. X-ray absorption spectrum at b) the Fe edge and c) Co edge (for two regions, inside the square element and from the circled regions in a. Spectra were obtained from the 8.4 μm square element. 167

7.18 Preliminary XMCD images with 1 s exposure at the a) Co L_{III} b) Fe L_{III} edges. X-rays at normal incidence, sensitive to the out of plane magnetisation. Measurements for the 8.4 μm square element. 168

7.19 XPEEM images aquired at the Fe L_{III} edge with a 5 s exposure time. a) X-ray absorption image of larger square element with b) showing the corresponding XMCD image. c) X-ray absorption image of smaller elements and d) the corresponding XMCD image. 170

List of Tables

3.1 Specification table of GPUs employed in figure 3.10. Showing Release Year, Memory Size, number of CUDA cores, and Computation Capability. 92

4.1 The value of the phase of the current at the sample, φ, obtained from the fits in Figure 4.2, is tabulated with the nominal phase at the synthesizer φ_{RF}, and the difference of the two values $\Delta\varphi$. 104

4.2 Mean and standard deviation of the effective field parameters extracted from the fits shown in Figure 4.3. Root Mean Square Error (RMSE) is defined as $\sqrt{\frac{\Sigma_{i=1}^{n}(\bar{X}_i - X_i)^2}{n}}$, where $X_i$and $\bar{X}_i$ are the fitted quantity and its mean value, and n is the number of measured values. 106

7.1 Orientation of initial field-like and anti-damping torques for representative values of $\hat{\boldsymbol{m}}$ (canted 30° from $\hat{\boldsymbol{z}}$), when a small static field is applied parallel the $\hat{\boldsymbol{x}}$ and $\hat{\boldsymbol{y}}$ directions. (Adjusted from reference [149]) 157

Author's Declaration

Chapter 2: Background material

This chapter covers the relevant background theory to this thesis, as such it is not the result of my own work but only compiled by myself. Some of the images are taken from the previously published works of other authors, where this is the case I have referenced the authors accordingly.

Chapter 3: Experimental Techniques

The theory of the experimental techniques has not been developed in this thesis, with reference material used for each discussion has been acknowledged. The STT-FMR system described in section 3.1 with corresponding computer software were both set up by myself.

The analytical theory for STT-FMR in section 3.2 was compiled by Prof. R. J. Hicken, the inclusion of Oersted field was proposed by Prof. V. V. Kruglyak and carried out by myself. The remaining derivation to obtain the equations in chapter 4 was carried out by myself under supervision of Prof. R. J. Hicken.

Time-resolved measurements detailed in section 3.5 have been developed at Exeter by Prof. R. J. Hicken, Dr Jing Wu, Dr Ralph Wilks, Dr Anjan Barman, Dr Volodymyr Kruglyak, Dr Paul Keatley, Dr Leigh Shelford and Dr Wei Yu before my arrival in the group. Data acquisition software was written by Prof. R. J. Hicken, Dr Ralph Wilks, Dr Anjan Barman, Dr T. Loughran and myself. The majority of

measurements carried out in this thesis required a modification of the microscope to accommodate low profile probes, the design of which was carried out by myself.

Within the methods used for macrospin modelling, the general procedure was developed under the supervision of Dr M. Dvornik. COMSOL modelling was carried out by myself with assistance from Dr T. Loughran, Dr A. A. Awad and Dr M. Dvornik where necessary. MuMax simulations were carried out primarily on the Ragnarök computing cluster at Gothenburg university, with additional simulations on the Exeter CDT computer cluster. The analysis and interpretation conducted by myself. The technical details for COMSOL and MuMax have been referenced accordingly.

XPEEM measurements were carried out at the BESSY II synchrotron and have been referenced accordingly, in collaboration with Dr Florian Kronast.

Chapter 4: Spatial Mapping of Torques within a Spin Hall Nano-oscillator

The SHNO's fabricated for these measurements were provided from a collaboration with Gothenburg university, from the work of Dr P. Dürrenfeld, Dr A. Houshang, Dr M. Ranjbar, and Prof. J. Åkerman. The STT-FMR and TRSKM measurements and analysis shown here were carried out by myself.

Chapter 5: Time resolved imaging of the non-linear bullet mode within an injection-locked spin Hall nano-oscillator

As previously the devices obtained here were obtained from a Gothenburg collaboration. The mageto-transport and TRSKM measurements and analysis shown here were carried out by myself.

Chapter 6: Current-induced picosecond magnetisation dynamics in Ta/CoFeB/MgO Hall Bars

The CoFeB Hall bars were fabricated by Wenzhe Chen under the supervision of Prof. Gang Xiao at Brown University. Optical sample characterisation and TRSKM experiments were performed by Dr C. Durrant. Analysis and further measurements were carried out by myself, employing a macrospin model developed by Prof. R. J. Hicken.

Chapter 7: Magnetisation Dynamics in Ta/CoFeB/MgO Elements driven by Unipolar and Bipolar Current Pulses

The samples studied in this chapter were designed by Dr C. Durrant and fabricated by Dr C. Durrant and Wenzhe Chen, with assistance from Shu-tong Wang, under the supervision of Prof. Gang Xiao, at Brown University. TRSKM experiments were performed by both myself and Dr C. Durrant. XPEEM measurements were carried out by myself with Dr Florian Kronast and assistance from Prof. R. Hicken, Dr T. Nakano and Jacob Roth.

List of Publications

Papers produced as part of this work, submitted papers are available on arXiv open access repository.

R. A. J. Valkass, T. M. Spicer, E. Burgos Parra, R. J. Hicken, M. A. Bashir, M. A. Gubbins, P. J. Czoschke, and R. Lopusnik, "Time-resolved scanning Kerr microscopy of flux beam formation in hard disk write heads", Journal of Applied Physics **119**, 233903 (2016).

T. M. Spicer, P. S. Keatley, T. H. J. Loughran, M. Dvornik, A. A. Awad, P. Dürrenfeld, A. Houshang, M. Ranjbar, J. Åkerman, V. V. Kruglyak, and R. J. Hicken, "Spatial mapping of torques within a spin Hall nano-oscillator", Physical Review B **98**, 214438 (2018).

T. M. Spicer, P. S. Keatley, M. Dvornik, T. H. J. Loughran, A. A. Awad, P. Dürrenfeld, A. Houshang, M. Ranjbar, J. Åkerman, V. V. Kruglyak, and R. J. Hicken, "Time resolved imaging of the non-linear bullet mode within an injection-locked nano-contact spin Hall nano-oscillator", Applied Physics Letters **113**, 192405 (2018).

T. M. Spicer, C. J. Durrant, P. S. Keatley, V. V. Kruglyak, W. Chen, G. Xiao, and R. J. Hicken, "Current-induced picosecond magnetization dynamics in a

Ta/CoFeB/MgO hall bar", Journal of Physics D: Applied Physics **52**, 355003 (2019).

Acronyms

AC	Alternating Current	AHE	Anomalous Hall Effect
BLS	Brillouin Light Scattering	CMOS	complimentary metal-oxice semiconductor
CPW	Coplanar Waveguide	CUDA	Compute Unified Device Archetecture
DC	Direct Current	DMI	Dzyaloshinskii-Moriya interaction
DRAM	Dynamic Random Access Memory	FMR	Ferromagnetic Resonance
FWHM	Full Width Half Maximum	GMR	Giant Magneto-Resistance
GPU	Graphical Processing Unit	LLG	Landau-Lifshitz-Guilbert equation
MOKE	Magneto-Optical Kerr Effect	MR	Magnetoreistance
MRAM	Magnetic Random Access Memory	MTJ	Magnetic Tunnel Junction
NC	Nano-contact	PMA	Perpendicular Magnetic Anisotropy
RE	Rashba Effect	RF	Radio Frequency
SHE	Spin Hall Effect	SHNO	Spin Hall Nano-Oscillator
STT	Spin Transfer Torque	STT-FMR	Spin Transfer Torque Ferromagnetic Resonance
TMR	Tunnel Magnetoresistance	TRSKM	Time-Resolved Scanning Kerr Microscopy
XMCD	X-ray Magnetic Circular Dichroism	XPEEM	X-ray Photoemission Microscopy

Symbols

A_{ex}	Exchange stiffness	α	Guilbert damping parameter
a and b	magnetic precession amplitudes	$\boldsymbol{B}$	magnetic field
$\boldsymbol{B}_{eff}$	Effective Magnetic Field	χ	spin wave function
c	speed of light	Δ	field linewidth
$\boldsymbol{D}$	electric displacement vector	e	electron charge
ϵ_0	permittivity of free space	ϵ_z	Zeeman energy
$\boldsymbol{\epsilon}$	generalized permittivity tensor	$\boldsymbol{E}$	electric field
$\boldsymbol{F}_{Lor}$	Lorentz force	FT	Amplitude of field-like STT
f	RF frequency	g	angular momentum g-factor
γ	gyromagnetic ratio	$\hbar$	reduced Plank's constant
$\boldsymbol{H}_{eff}$	Effective Magnetic Field	$\mathcal{H}$	Hamiltonian
$\mathcal{H}_{spin}$	Spin Hamiltonian	$\mathcal{H}_{eff}$	Effective Hamiltonian
$\boldsymbol{H}$	Magnetic field	$\boldsymbol{H}_d$	demagnetising field
$\boldsymbol{H}_0$	time-static magnetic field	$\boldsymbol{h}_{\sim}$	time-varying magnetic field
$\mathcal{H}_{SO}$	Spin Orbit Hamiltonian	$\boldsymbol{H}_{rf}$	RF Oersted Field
H_{ext}	External magnetic field	I	electric current
$\boldsymbol{j}$	combined angular momentum	J	Exchange constant
J and J_{Charge}	Charge current density	J_{Spin}	Spin current density
K_{c1} and K_{c2}	Cubic anisotropy constants	$\boldsymbol{l}$	orbital angular momentum
m_e	electron mass	$\boldsymbol{m_o}$	orbital magnetic moment

μ_B	Bohr Magneton	$\boldsymbol{m_s}$	spin magnetic moment
$\boldsymbol{M}$	Magnetisation	$\boldsymbol{m}$	Magnetisation unit vector
w_{ms}	magnetostatic energy per unit volume	M_{sat}	saturation magnetisation
$\boldsymbol{M}_0$	time-static magnetisation	$\boldsymbol{m}_{\sim}$	time-varying magnetisation
N	total number of electrons	$\tilde{\boldsymbol{N}}$	demagnetising tensor
$\boldsymbol{n}$	vector normal to sample plane	ω_0	precession frequency
ψ	electron wave function	Ψ	combined wave function
φ	spatial wave function	$\boldsymbol{p}$	electron momentum
Q_V	Voigt material constant	Q	Magneto-optical constant
$\boldsymbol{r}$	radius	$\boldsymbol{r}_1$ and $\boldsymbol{r}_2$	Electron positions
ρ	electrical resistivity	$\rho_\perp$	perpendicular resistivity
$\rho_\parallel$	parallel resistivity	ΔR	AMR constant
$\boldsymbol{s}$	spin angular momentum	$\boldsymbol{s}_1$ and $\boldsymbol{s}_2$	Electron spins
σ_{xy}	transverse charge conductivity	σ_{xx}	longitudinal charge conductivity
$\boldsymbol{\sigma}$	electron spin polarisation	$\hat{\boldsymbol{s}}_{free}$	spin unit vector of free layer
$\hat{\boldsymbol{s}}_{pin}$	spin unit vector of pinned layer	ST	amplitude of anti-damping STT
t	time	θ	magnetisation angle
Θ_{SH}	Spin Hall Angle	$\boldsymbol{\tau}_{STT}$	Spin Transfer Torque
T	layer thickness	$\boldsymbol{v}$	velocity
V	electrical voltage	W	free energy density
w_{ex}	exchange energy per unit volume	w_Z	Zeeman energy per unit volume
w_{Kc}	Crystal anisotropy per unit volume		

CHAPTER 1

Introduction

"The use of computers is permeating every aspect of our lives and this, with their rapidly increasing use of telecommunication channels for the automatic exchange of data, is bound to exert significant influence on the organization and conduct of most of our activities."

F. J. M. Laver in 1975[1]

Within the modern world, many tasks demand vast amounts of computational power and an ever-expanding communications network. While these areas have observed extraordinary growth over the last few decades, the continued development of key electrical components for such systems is required. The majority of electronic processing systems are built on CMOS (complementary metal-oxide-semiconductor) logic gates. However, with increasing operating speeds, charge currents requirements and the need for further miniaturization, this technology is approaching its limits. The research of magnetic materials has already played a key part in this advancement by improving systems for data storage. Now, it is hoped the control of magnetic devices with spin-polarised currents can yield improved performance over their charge-based counterparts. As a result, the field of spin electronics (or spintronics) has garnered much academic and industrial interest.

The aim of spintronics is to develop devices that work by the transport of electron spin (rather than their charge) and describe the new physics that arises. Devices built on such principles are expected to consume less power than conventional electronics and may solve existing problems (such as difficulties with thermal management). The first passive spintronic device, the spin valve, consisted of two magnetic layers with a non-magnetic spacer. These devices exhibit the Giant Magneto Resistance effect (GMR),[2] in which the electrical resistance of a spin valve depends on the relative orientation of the magnetisation in the two ferromagnetic layers. This device was incorporated into hard disk drives in the late 1990's, leading to a sharp increase in storage density.[3,4]

Within active spintronics, the magnetic layer can be controlled directly through spin transfer torque (STT). While the generation of spin currents suitable to exert STT require other physical phenomena, this process allows magnetic materials to be exploited for their useful magnetic properties (such as a low damping constant or high magnetisation). From a technological standpoint, two key areas of interest can be seen: 1) construction of memory elements, and 2) high-frequency oscillators.[5] In both areas, the field of spintronics is expected to confer specific advantages over existing systems, while also demonstrating the potential for post-CMOS computing.[6]

In order to generate sufficient STT, potential systems require the efficient generation of spin current. This can simply be achieved by passing a charge current through a ferromagnet, a process known as spin filtering. Such structures, however, are more sensitive to thermal effects (such as Joule heating), leading to increased linewidth (in oscillators) and reduced thermal stability (in memory elements), among other issues. To overcome this, there has been considerable interest in utilizing Spin Hall (SHE) and Rashba effects (RE), whereby the flows of charge and angular momentum have been decoupled.

In order to compete with existing electronics, it is imperative that spintronic devices must function on the similar time-scales. Key questions in this field concern

the observation and understanding of dynamics on the GHz or ns scale. Fortunately, the planar geometries employed by SHE and RE devices lend themselves to observation by optical techniques, allowing optical access to the active regions and surrounding structure.

Time-resolved scanning Kerr microscopy (TRSKM) has proved a powerful tool for the investigation of ultrafast magnetisation dynamics. In this thesis, it will be employed along with numerical and simulation techniques to understand the process within spintronic devices. This work will first consider oscillators driven by SHE spin currents (dubbed spin Hall nano-oscillators, or SHNOs) and memory element devices (known as magnetic tunnel junctions or MTJs) with the goal of probing the underlying torques present on the ns timescale.

Chapter 2 outlines the principles of magnetism relevant to this thesis. Beginning from a semi-classical origin of magnetism, the key contributions to the free energy of a ferromagnetic material are discussed. Following this is a description of key static and dynamic phenomena common to many magnetic systems: magnetic domains, ferromagnetic resonance, anisotropic magneto-resistance and spin wave modes. Finally, the origin of spin-orbit effects will be addressed, relating to SHE and RE. This chapter will aim to provide a general background with a focus on the literature of immediate relevance.

Chapter 3 describes the experimental and numerical methods employed throughout. Beginning with ferromagnetic resonance (FMR), an experimental approach for its measurement within spintronic devices is described (STT-FMR) followed by a full analytical derivation for the interpretation of resonance curves obtained. From anisotropic magneto-resistance, it is possible to electrically observe the change in magnetic states in response to AC and DC excitations. Such measurements require high-frequency electronic equipment, for which a general purpose set-up is described. A phenomenological description of magneto-optical effects is provided, to aid the understanding of TRSKM measurements. Three configurations of TRSKM measurements are considered within this thesis, while the

optics largely remain unchanged each set-up considers different electrical excitations. Detailed diagrams & descriptions are included in this chapter for reference throughout. For some chapters, it was necessary to employ simulations to aid the interpretation of TRSKM observations. While not the focus of this thesis, the simulation of magnetisation dynamics within spintronic devices is non-trivial and hence the methodology employed has been outlined. Finally, for ground state measurements employed in chapter 7 the XPEEM station at the BESSY II synchrotron was used, a brief description of this technique and the underlying phenomena will be provided with direction to further references.

Chapter 4 aims to uncover the distribution of torques present within SHNOs driven at high frequency. To do so, TRSKM is employed in a new way to optically detect SHNOs undergoing FMR in a manner similar to the STT-FMR technique. By careful analysis of the resonance curves using the analytical theory outlined in section 3.2, the in-plane and out-of-plane STT and Oersted field within the device can be mapped. By comparison with the calculated DC distribution it is clear that a different distribution is present for RF current, an effect not previously observed in spintronics.

Chapter 5 continues the work on SHNOs by considering the injection of DC, thereby exciting an auto-oscillating mode immediately below the frequency of FMR. This spin wave 'bullet' has garnered much interest due to its highly tunable microwave oscillation with a low spectral linewidth. The injection of DC and RF current excites both the bullet mode and an off-resonance FMR mode in superposition. Further measurement demonstrated that the bullet's localization is reduced for higher DC, due to either some interaction with the FMR mode or modified torque landscape.

Chapter 6 progresses to consider the torques involved in current-induced magnetisation reversal, as expected to be present in spintronic memory elements. CoFeB exhibits perpendicular magnetic anisotropy when adjacent to a layer of MgO, promoting low switching currents and high thermal stability (properties well

suited to memory applications) Hall bars constructed from this material have previously been shown by scanning Kerr microscopy to switch via domain wall mechanisms in response to continuous electrical current. Here, TRSKM measurements of the dynamics induced by sub-ns pulses will be interpreted with the aid of macrospin modelling, indicating conditions that favour the switching process.

Chapter 7 considers micron-scale elements of the same stack structure considered in the previous chapter. In order to test the devices' suitability for data storage applications, they were subjected to TRSKM measurements with two types of electrical pulses. Firstly, sub-ns uni-polar pulses were used to explore the spatial character of dynamic magnetisation. Secondly, a bi-polar pulse aims to 'write' and 'reset' the magnetic state, thereby elucidating the mechanisms present in the ultrafast switching process. To understand the magnetic ground state in elements, XPEEM measurements were carried out on a nominally identical sample.

Chapter 8 will provide a summary of the work carried out within this thesis. In addition, open questions will be raised and opportunities for future work outlined.

CHAPTER 2

Background material

2.1 Introduction

This chapter will cover many of the theoretical concepts and physical phenomena encountered in the study of spintronics. Much of what is written here has its origins within the interaction of the electron spin and orbital angular momentum, a detailed description of which requires an extensive quantum mechanical treatment. While this origin is not forgotten, such a description is beyond the scope of this thesis. Instead, a semi-classical description will be presented with key points from quantum mechanics highlighted.

Starting from a description of static magnetisation, interactions leading to and resulting from dynamic magnetic processes will be discussed. This will lead to a summary of the experimental techniques used throughout.

2.2 A Semi-classical Origin of Magnetism

In order to discuss the origin of magnetism, one must begin with the fundamental constituent of ordinary matter, the atom. Considering a classical model of the atom, a negative point charge orbits a positive point charge as depicted in figure 2.1. The angular momentum l due to the circular orbit is described by[7–9]

$$\boldsymbol{l} = -m_e \boldsymbol{v} \times \boldsymbol{r}, \tag{2.1}$$

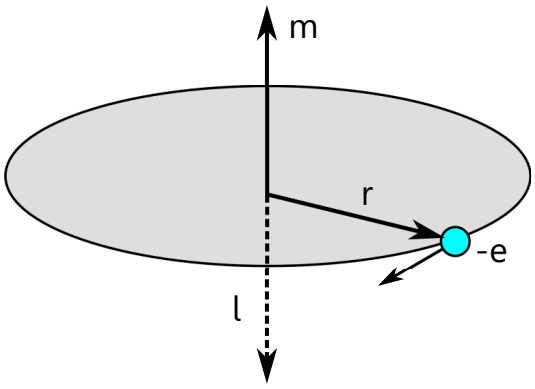

Figure 2.1: Classical schematic of an atom. Electron of charge $-e$ orbiting with distance r and velocity v, angular momentum l generating magnetisation m.

where, m_e is the electron mass, and $\boldsymbol{v}$ and $\boldsymbol{r}$ the velocity and radius of orbit respectively. The electric current I is the rate of flow of charge, given by

$$I = -\frac{ev}{2\pi r}, \tag{2.2}$$

where e is the magnitude of electron charge. The resulting magnetic moment (m_o) is the electrical current multiplied by the area (from Ampère's law)

$$|\boldsymbol{m_o}| = I\pi \boldsymbol{r}^2, \tag{2.3}$$

which lies in the direction normal to the plane of the current loop. This can be expressed in terms of the orbital angular momentum[10]

$$\boldsymbol{m_o} = -\frac{e\boldsymbol{v} \times \boldsymbol{r}}{2} = -\frac{e}{2m_e}\boldsymbol{l}. \tag{2.4}$$

Within the Bohr model of the atom, there exist discrete orbits available to electrons. As a result angular momentum is quantized with the lowest allowed quantum number equal to $\hbar$. Such that,

$$|\boldsymbol{m_o}| \rightarrow -\frac{e}{2m_e}\hbar = -\mu_B, \tag{2.5}$$

where μ_B is the Bohr magneton, used as the fundamental magnetic moment. Quantum mechanical calculations confirm this for the orbital moment. However, quantum mechanics also predicts a contribution from the electron spin which is twice as large as the orbital moment

$$\boldsymbol{m_s} = -\frac{e}{m_e}\boldsymbol{s} \tag{2.6}$$

for $\boldsymbol{s}$ intrinsic angular momentum of the electron. As electron spin is quantum mechanical in origin there is no classical explanation for this behaviour.

The total magnetic moment of an atom is due to a combination of orbital and spin moments. Allowing the total magnetic moment to be written as

$$\boldsymbol{m} = -g\frac{e}{m_e}\boldsymbol{j} \tag{2.7}$$

for $\boldsymbol{j}$ the combined orbital and spin angular momentum, and g accounting for the contributions from orbital and spin moments. Such that $g = 1$ for pure orbital atomic moment, $g = 2$ for pure spin moments, or for a combination it would lie somewhere between these values.

2.3 Ferromagnetic free energy contributions

The ground state and dynamic magnetisation of a ferromagnet are determined by the contributions to its total free energy. In principle, the vector field of magnetisation directions is chosen so that the total (free) energy reaches an absolute or relative minimum. In this case, the torque due to effective fields is zero, as described by Brown's differential equation[11]

$$\boldsymbol{M} \times \boldsymbol{H}_{eff} = 0, \tag{2.8}$$

where $\boldsymbol{M}$ represents magnetisation, and $\boldsymbol{H}_{eff}$ the effective magnetic field. When the magnetisation aligns with the effective field there is no torque present, yielding

an equilibrium or static magnetic state. $\boldsymbol{H}_{eff}$ can be written in terms of the free energy density W functional derivative,[12]

$$\boldsymbol{H}_{eff} = -\frac{\delta W}{\delta \boldsymbol{M}}. \tag{2.9}$$

Here the free energy density can be written as the sum of energy contributions due to the exchange interaction, Zeeman energy, magnetostatic, and magnetocrystalline anisotropy. Additional terms may be included where suitable, for example, magneto-mechanical terms for materials which change magnetisation under mechanical stress or strain.[13]

2.3.1 Exchange Energy

Section 2.2 outlined how a single atom may possess a magnetic moment, however, this does not account for the spontaneous magnetisation of a ferromagnetic material. At the beginning of the 19th century, Weiss proposed that in the absence of a strong external magnetic field the neighboring molecular moments could generate a field, significant enough as to affect the sample's magnetisation.[14] Initially referred to as the *molecular field* this was later identified by Heisenberg as the quantum mechanical exchange interaction, arising from the interplay of the Coulomb interaction, and the Pauli exclusion principle. An abridged description will be presented here, while a detailed description can be found in references [15] and [16].

In essence, this effect results from the coupling of the spins of two electrons in order to minimize their energy. Considering two adjacent hydrogen atoms (as in a H_2 molecule), the electrons associated with each atom can be assigned wave functions ψ_1 & ψ_2, positions $\boldsymbol{r}_1$ & $\boldsymbol{r}_2$, and spin $\boldsymbol{s}_1$ & $\boldsymbol{s}_2$. The combined wave function is given by

$$\Psi(\boldsymbol{r}_1, \boldsymbol{s}_1, \boldsymbol{r}_2, \boldsymbol{s}_2) = \psi_1(\boldsymbol{a})\psi_2(\boldsymbol{b}) = \Psi(\boldsymbol{a}, \boldsymbol{b}), \tag{2.10}$$

where states $\boldsymbol{a}$ and $\boldsymbol{b}$ represent both position and spin orientations. By simply exchanging electrons, an equivalent wave function can be written as

$$\Psi(\boldsymbol{a},\boldsymbol{b}) = \psi_1(\boldsymbol{b})\psi_2(\boldsymbol{a}), \tag{2.11}$$

whereby the subscripts denoting spin and position have been exchanged. A solution can be written in terms of single particle wave functions

$$\Psi(\boldsymbol{a},\boldsymbol{b}) = \frac{1}{\sqrt{2}}[\psi_1(\boldsymbol{a})\psi_2(\boldsymbol{b}) \pm \psi_1(\boldsymbol{b})\psi_2(\boldsymbol{a})], \tag{2.12}$$

where $\Psi(\boldsymbol{a},\boldsymbol{b})$ may be a symmetric (plus sign) or antisymmetric (minus sign) wave function. During the exchange of electrons, a symmetric function is unchanged ($\Psi_{sym}(\boldsymbol{a},\boldsymbol{b}) = +\Psi_{sym}(\boldsymbol{b},\boldsymbol{a})$) while an asymmetric function must change sign ($\Psi_{asym}(\boldsymbol{a},\boldsymbol{b}) = -\Psi_{asym}(\boldsymbol{b},\boldsymbol{a})$). As electrons are fermions, the overall wave function must be antisymmetric. To achieve this, either the spin state or spatial state must be antisymmetric with respect to exchange, leading to two possible wave functions. By further separating the spin (χ) and spatial (φ) wave functions, the singlet state is given by

$$\Psi_S(\boldsymbol{r}_1,\boldsymbol{s}_1,\boldsymbol{r}_2,\boldsymbol{s}_2) = \frac{1}{\sqrt{2}}[\varphi_1(\boldsymbol{r}_1)\varphi_2(\boldsymbol{r}_2) + \varphi_1(\boldsymbol{r}_2)\varphi_2(\boldsymbol{r}_1)]\chi_S(\boldsymbol{s}_1,\boldsymbol{s}_2), \tag{2.13}$$

and the triplet state is given by

$$\Psi_T(\boldsymbol{r}_1,\boldsymbol{s}_1,\boldsymbol{r}_2,\boldsymbol{s}_2) = \frac{1}{\sqrt{2}}[\varphi_1(\boldsymbol{r}_1)\varphi_2(\boldsymbol{r}_2) - \varphi_1(\boldsymbol{r}_2)\varphi_2(\boldsymbol{r}_1)]\chi_T(\boldsymbol{s}_1,\boldsymbol{s}_2). \tag{2.14}$$

The names of these states arise from the number of possible values of the spin state. Since the spin state of a single electron can be either 'up' ($\chi^{\uparrow}$) or 'down' ($\chi^{\downarrow}$), the singlet spin state can be written as

$$\chi_S(\boldsymbol{s}_1,\boldsymbol{s}_2) = \frac{1}{\sqrt{2}}(\chi_1^{\downarrow}\chi_2^{\uparrow} - \chi_1^{\uparrow}\chi_2^{\downarrow}). \tag{2.15}$$

While in the triplet state there are three spin states, owing to the three eigenvalues of the spin quantum number (S_z = -1, 0, or +1) , which can be written as

$$\chi_T(\boldsymbol{s}_1, \boldsymbol{s}_2) = \begin{cases} \chi_1^{\uparrow}\chi_2^{\uparrow} \\ \frac{1}{\sqrt{2}}(\chi_1^{\downarrow}\chi_2^{\uparrow} + \chi_1^{\uparrow}\chi_2^{\downarrow}) \\ \chi_1^{\downarrow}\chi_2^{\downarrow}. \end{cases} \tag{2.16}$$

It can be seen that χ_S is antisymmetric with respect to exchange, while χ_T is symmetric with respect to exchange. In order to describe the energy arising from exchange, we will consider the electron-electron interaction with the Hamiltonian

$$\mathcal{H} = \frac{e^2}{4\pi\epsilon_0 r_{12}}, \tag{2.17}$$

where e is the electron charge, ϵ_0 the permittivity of free space and r_{12} the separation of the electrons. The singlet and triplet state energies are

$$E_S = \iint \Psi_S^* \, \mathcal{H} \, \Psi_S \, d\boldsymbol{r}_1 d\boldsymbol{r}_2 \quad and \quad E_T = \iint \Psi_T^* \, \mathcal{H} \, \Psi_T \, d\boldsymbol{r}_1 d\boldsymbol{r}_2, \tag{2.18}$$

with Ψ_S^* & Ψ_T^* the complex conjugates of Ψ_S & Ψ_T respectively. The exchange constant J is defined by

$$J = \frac{E_S - E_T}{2} = \int\int \varphi_a^*(\boldsymbol{r}_2)\varphi_b^*(\boldsymbol{r}_1) \, \mathcal{H} \, \varphi_a(\boldsymbol{r}_2)\varphi_b(\boldsymbol{r}_1) \, d\boldsymbol{r}_1 d\boldsymbol{r}_2, \tag{2.19}$$

providing the spin states have been normalized. Spin can now be incorporated within a spin-dependant effective Hamiltonian,

$$\mathcal{H}_{spin} = -2J\boldsymbol{s}_1 \cdot \boldsymbol{s}_2. \tag{2.20}$$

Equations (2.19) and (2.20) give spin- and space-dependant energies for two electrons within a single H_2 molecule. This has been generalized for a many-atom system, giving the effective Heisenberg Hamiltonian

$$\mathcal{H}_{eff} = \sum_{i \neq j}^{N} J_{ij} \boldsymbol{s}_i \cdot \boldsymbol{s}_j = -2 \sum_{i<j}^{N} J_{ij} \boldsymbol{s}_i \cdot \boldsymbol{s}_j, \tag{2.21}$$

for a total of N electrons, and J_{ij} the exchange integral given as,

$$J_{ij} = \int \int \varphi_i(\boldsymbol{r}_1) \varphi_j(\boldsymbol{r}_2) \frac{e^2}{4\pi\epsilon_0 r_{12}} \varphi_i^*(\boldsymbol{r}_2) \varphi_j^*(\boldsymbol{r}_1) d\boldsymbol{r}_1 d\boldsymbol{r}_2. \tag{2.22}$$

From equation (2.21), the energy is minimized for spins close to parallel. In addition, the exchange integral falls off rapidly as the separation of electrons increases, hence only the exchange interaction between neighbouring atoms is typically considered.

However, for the macrospin length scales ($\sim 1 - 10$ nm) it is more useful to consider the exchange stiffness expression given by[14]

$$E_x = A_{ex} \int (\nabla \boldsymbol{m})^2 dV \tag{2.23}$$

where $\boldsymbol{m}$ is the unit vector parallel to $\boldsymbol{M}$ and A_{ex} is the exchange stiffness constant, which is a material parameter, and in general temperature-dependant. This can be rearranged for the exchange energy per unit volume

$$w_{ex} = A_{ex} (\nabla \boldsymbol{m})^2. \tag{2.24}$$

The exchange interaction plays a significant role in magnetic structure for both static and dynamic phenomena.

2.3.2 Zeeman Energy

The Zeeman interaction is the term used to describe the interaction between the magnetic moments of atoms within a material and an external magnetic field. An energy minimum is achieved when the magnetisation and applied field are parallel, with an increase in potential energy proportional to the angle between the two. The Zeeman energy per unit volume is given by

$$w_Z = -\boldsymbol{M} \cdot \boldsymbol{H}. \tag{2.25}$$

It should be noted that $\boldsymbol{H}$ may take many forms, such as a static bias field or a time-varying pulsed field.

2.3.3 Magnetostatic Energy

Magnetostatic energy (also known as the dipolar or stray field energy) relates to the magnetic field generated by the magnetic body itself.[14] This effect is much weaker than the exchange interaction but acts on a larger length scale, as such, atoms may interact as an array of magnetic dipoles. The energy density is given by[12]

$$w_{ms} = -\frac{1}{2}\boldsymbol{H}_d \cdot \boldsymbol{M}, \tag{2.26}$$

where the demagnetising field $\boldsymbol{H}_d$ is often written as

$$\boldsymbol{H}_d = -\tilde{\boldsymbol{N}}(\boldsymbol{r})\boldsymbol{M}, \tag{2.27}$$

where $\tilde{\boldsymbol{N}}$ is the demagnetising tensor. Since $\tilde{\boldsymbol{N}}$ is sensitive to the shape of the sample under investigation, it follows that different sample shapes give rise to stronger or weaker demagnetising fields. This effect gives rise to magnetic shape anisotropy, where a preferred magnetisation is given from the shape of a sample.

The focus of this thesis is thin films. For a uniformly magnetised thin film the energy density takes the form

$$w_{ms} = 2\pi M_{sat}^2(\boldsymbol{m} \cdot \boldsymbol{n}), \tag{2.28}$$

for $\boldsymbol{n}$ the vector normal to the sample plane. In this case the energy is minimised when the magnetisation lies within the plane of the sample.

While the magnetostatic interaction is far weaker than the exchange interaction, it acts on a longer range and is therefore an important contribution to the free energy. The minimisation of magnetostatic energy may require magnetic domains to develop, and will be discussed further in section 2.4.

2.3.4 Magnetic Anisotropy

Crystallographic axes present within a material can give rise to preferred magnetisation directions. The most energetically favorable directions are dubbed the "easy" axes, while the least favorable directions are referred to as the "hard" axes. Specifically, magnetocrystalline anisotropy is the energy required to rotate the magnetisation between these axes.[14] The origin of this effect is non-trivial and involves the interplay of the exchange interaction and the spin–orbit interaction among other effects.[16] This however, sets magnetocrystalline anisotropy apart from shape anisotropies, which arises from the stray field.

The specific form of the energy density depends on the crystal structure, for cubic crystals (such as iron)[17]

$$w_{Kc} = K_{c1}(m_1^2 m_2^2 + m_1^2 m_3^2 + m_2^2 m_3^2) + K_{c2} m_1^2 m_2^2 m_3^2, \tag{2.29}$$

where K_{c1} and K_{c2} the first and second order anisotropy terms, and m_i the component of magnetisation along the [1]cubic axis. In this case energy is minimized when the magnetisation lies along any of the axes (1, 2 or 3) as all terms will equal zero. Conversely, it costs energy to align the magnetisation at some intermediate angle between crystal axes.

The relative amplitudes and sign of K_{c1} and K_{c2} dictate the position of easy axes. For example, if the higher order K_{c2} term is neglected and K_{c1} positive, magnetisation in the $\langle 100 \rangle$, $\langle 010 \rangle$, and $\langle 001 \rangle$ directions represent energy minima.

[1] In a primitive cubic crystal, the nearest atoms lie in the $\langle 100 \rangle$, $\langle 010 \rangle$, and $\langle 001 \rangle$ directions.

Conversely if K_{c1} is negative, these directions represent energy maxima, with the $\langle 111 \rangle$ directions now the preferred orientations.

2.4 Magnetic Domains

In practice, there may be different and competing energy contributions within a sample. As a result, a uniform sample magnetisation is not always energetically favourable, instead discrete regions will have preferred orientations. The term magnetic domain is used to describe a region within a magnetic material within which the vector magnetisation is uniform.

In an order to reconcile all these energy contributions, the system can form a multi-domain state with non-parallel magnetisation between adjacent domains. To minimize exchange energy between domains there is a gradual change in magnetisation orientation between the two states. These structures are called *domain walls* with a thickness dictated by the material's exchange length. These structures have two methods of rotation available, rotation parallel to the domain wall plane (Bloch walls) and rotation normal to the same plane (Néel walls).

For thin films (i.e. film thickness comparable to the domain wall width, as primarily considered in this thesis) it is important to distinguish films with in-plane anisotropy and perpendicular anisotropy. Those with in-plane anisotropy will see the domains with magnetisation in the plane of the film, while those with perpendicular anisotropy will support domains with magnetisation out of the sample plane.

Figure 2.2 illustrates the structure of Bloch and Néel walls in materials with perpendicular and in-plane magnetic anisotropy. For in-plane anisotropy, it can be seen that a Néel wall requires lower energy to form due to a reduced stray field. However, for materials of perpendicular magnetic anisotropy (PMA) it becomes a little more complicated.

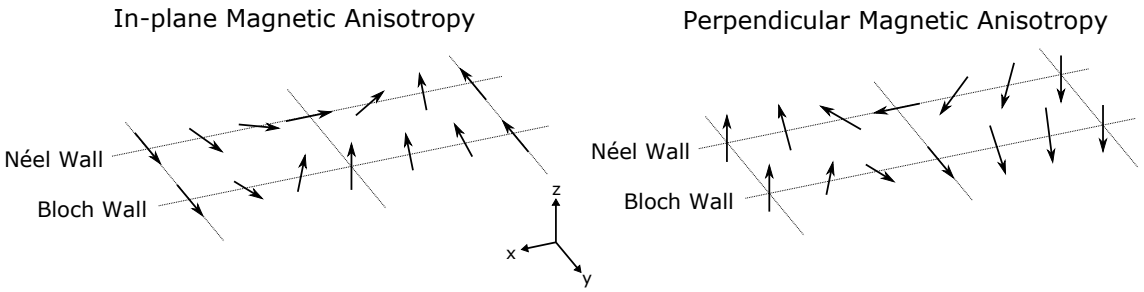

Figure 2.2: Schematic of Bloch and Néel walls present within materials of perpendicular and in-plane magnetic anisotropy. Domain wall is shown in the $\hat{y} - \hat{z}$ plane, for Bloch walls magnetisation rotates within this plane whereas rotation is normal to the plane for Néel walls.

Bubble domains are isolated cylindrical magnetic domains, typically observed in materials with PMA, these structures are of interest for data storage applications.[18,19] As neighbouring domains possess opposite out of plane magnetisation there is a significant stray field between the two. For thicker films (on order of μm), the domain wall magnetisation at the surface lies parallel to this field, in effect a Néel wall. However, as the stray field lies in the opposite direction on the opposite surface, the domain wall magnetisation for the upper and lower surfaces are anti-parallel. These *twisted* domain walls rotate through 180° between surfaces, such that a Bloch wall exists within the middle of the film.[14,20] For thin films (on order of nm) the twisting angle is reduced, for sufficiently thin films there is no twisting and instead a Bloch wall is present. This was predicted by micromagnetic analysis[21] and later confirmed by magnetic force Microscopy.[22]

The ways in which domains form depend heavily on a sample's shape and material. As a result specific domain patterns are not always repeatable. For example, a thin disk of Permalloy (a nickel iron alloy) will form a 'vortex' state in the absence of an external field, shown in figure 2.3a. The minimum energy state can be represented by either clockwise or anti-clockwise magnetisation. Similarly, thin films of Garnet favor a 'maze-like' domain structure, as shown in figure 2.3b. While some regions may 'seed' domain formation, the same sample can support an infinite number of domain structures all representing a local energy minimum.

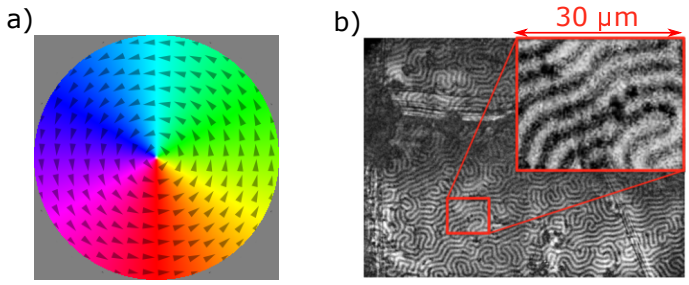

Figure 2.3: a) Simulated vortex domain structure within a disk (5 nm thick, and 4 μm diameter) from Mumax3, colourscale and arrows represent the in-plane direction of magnetisation. b) Wide field Kerr microsopy image of magnetic domains in a Garnet film, grayscale representing the out of plane component of $\boldsymbol{M}$, reproduced from [23].

Data can be stored in a magnetic material by manipulating the domain state, which can be done with a focused magnetic field. Hard disk drives store data as perpendicular magnetic domains, which can be written at high speed and remain stable for $\sim$ 10 years.[3] Furthermore, there is much interest in the concept of "racetrack" memory where a magnetic wire contains data within magnetic domains, which can be moved past a read-out sensor by an electrical current passing along the wire.[4,24]

2.5 Precessional Dynamics

2.5.1 Ferromagnetic Resonance

Ferromagnetic Resonance (FMR) is the collective motion of the magnetisation in a ferromagnet under the influence of both a static and time-varying magnetic field. FMR was first observed experimentally in 1946 by Griffiths,[25] with a theoretical description later provided by Kittel in 1948.[26]

The undamped precession of a magnetic dipole around a magnetic field can be given by the equation

$$\frac{d\boldsymbol{M}}{dt} = -\gamma \boldsymbol{M} \times \boldsymbol{H}, \tag{2.30}$$

where $\boldsymbol{M}$ represents the sample magnetisation, t represnts time, γ the gyromagnetic ratio, and $\boldsymbol{H}$ the total magnetic field.[27] For FMR both $\boldsymbol{M}$ and $\boldsymbol{H}$ can be given by the sum of static ($\boldsymbol{M}_0$ and $\boldsymbol{H}_0$) and alternating ($\boldsymbol{m}_\sim$ and $\boldsymbol{h}_\sim$) parts. It follows that for a small amplitude of precession driven by external fields, the dipole will precess at a frequency dependent on the magnitude of the applied field $\omega_0 = \gamma H_0$.

However this does not take into account the demagnetisation effects, which play an important role particularly in thin films. The following calculations will consider the simplest case, that of uniform oscillations within a small ferromagnetic ellipsoid. Here, we define $\hat{z}$ along the ellipse, which is parallel to $\boldsymbol{M}$. Given the demagnetisation field in equation (2.27), the static and alternating fields can be written as

$$\boldsymbol{H}_0 = \boldsymbol{H}_{0ext} - \tilde{\boldsymbol{N}}\boldsymbol{M}_0 \quad and \quad \boldsymbol{h}_\sim = \boldsymbol{h}_{\sim ext} - \tilde{\boldsymbol{N}}\boldsymbol{m}_\sim, \tag{2.31}$$

where $\tilde{\boldsymbol{N}}$ is the demagnetisation tensor, $\boldsymbol{H}_{0ext}$ and $\boldsymbol{h}_{\sim ext}$ the external static and alternating fields respectively. Including these effects Kittel obtained his famous equation for the frequency of FMR[26]

$$\omega_0 = \gamma\sqrt{[H_0 + (N_x - N_z)M_0][H_0 + (N_y - N_z)M_0]}, \tag{2.32}$$

where H_0 is applied in the plane of the sample, and is parallel to the magnetisation, N_i represent the [2]demagnetisation factors. This can be further simplified for considering the limiting case of an infinitely thin plane with in-plane magnetisation, where $N_x = N_z = 0$ and $N_y = 4\pi$. Therefore equation (2.32) reduces to

$$\omega_0 = \gamma\sqrt{H_0(H_0 + 4\pi M_0)}. \tag{2.33}$$

The experiments presented within this thesis were performed on non-ellipsoidal magnetic layers. The calculation of demagnetising factors for non-ellipsoids is

[2]In the present case, these come from the diagonalized form of the demagnetisation tensor.

non-trivial and lies beyond the scope of this thesis, further details can be found in [28].

2.5.2 Spin waves

A sample undergoing FMR possesses a spatially uniform precession. However it is possible for atomic moments to precess with a different phase to their neighbour, giving rise to non-uniform dynamics even in the presence of uniform excitation. A 1-dimensional schematic of this is represented in figure 2.4. Here a line of spins with successive advances in phase between spins forms a spin wave. This concept was first proposed by Bloch in 1930.[16,27]

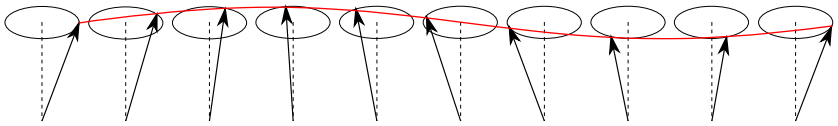

Figure 2.4: Schematic representation of a spin wave. A line of spins (represented with arrows) with successive increase in phase of precession about the dashed line, for an separation of a between each moment. The wavelength depicted is $9a$.

For spin waves of wavelength significantly larger than atomic separation, the exchange energy is negligible compared to the magnetostatic interaction. Such magnetostatic modes were first studied by Damon and Eshbach in 1961.[29] By assuming a small dynamic component they were able to linearise the equation of motion to obtain a spin wave spectrum. In contrast, a description of spin waves with wavelengths comparable to the atomic separation requires the inclusion of exchange energy. This was originally done by Bloch, Holstein and Primakoff who constructed a microscopic theory including the Zeeman interaction and dipole-dipole interaction.[30]

These calculations, however, are based on linear theory (i.e. the precession amplitude is small compared to the total magnetisation). There exist a number of phenomena which exhibit large amplitude precession and hence require a *nonlinear* description. While the linear theory applies to the FMR presented in

chapter 4, it does not apply to the spin wave 'bullet' as presented in chapter 5, nor does it apply to current-induced switching.

For the spin wave bullet, a non-linear theory has been presented by Slavin and Tiberkevich.[31] This approach provides a superior description of both the spatial and spectral character of the mode than that of linear calculations. Here, the authors employ a classical Hamiltonian method detailed in reference [32], however alternative approaches to similar cases can be found at reference [33].

Rather than derive non-linear equations of dynamics, this thesis will employ micromagnetic and macrospin simulations for comparison with theory.

2.6 Anisotropic Magneto-resistance

Anisotropic magneto-resistance (AMR) is the variation of electrical resistance in a ferromagnet as a function of the magnetisation direction relative to the current direction.[14] This phenomenon was discovered in 1856 by William Thompson (Lord Kelvin), who observed a change in the electrical resistance of nickel of $\sim 0.7\%$ under a transverse magnetic field.[34] The angle-dependent resistivity can be formulated as[35]

$$\rho(\theta) = \rho_{\perp} + (\rho_{\parallel} - \rho_{\perp})cos^2\theta, \tag{2.34}$$

where $\rho_{\parallel}$ is the resistivity observed when the magnetisation is parallel to the direction of current (where $\theta = 0$), and $\rho_{\perp}$ is the resistivity at $\theta = 90°$. It is typical for measurements to report the DC resistance V/I and the differential resistance dV/dI. Here the excitation of magnetisation dynamics can manifest as peaks or other features.[36–39] The value of $(\rho_{\parallel} - \rho_{\perp})$ varies between materials and possesses a small dependance on field amplitude and temperature.[40] This effect has seen application within magnetic sensors, enabling the bits on magnetic data storage media to be read electrically.

AMR is typically explained in terms of the spin-orbit interaction and its influence on s-d scattering processes. Spin-dependent scattering of the injected current

increases when the magnetisation is parallel to the direction of current. The origin of the AMR requires a full quantum mechanical description which lies beyond the scope of this thesis, but can be found in [16] and [41]. It should also be noted that many additional kinds of magneto resistance are known,[42] these include giant magnetoresistance[43] and tunnelling magneto resistance.[44]

2.7 Spin-Orbit torques

2.7.1 Anomalous Hall Effect

In 1879 Edwin Hall discovered that when an electrical conductor is placed within a magnetic field, a transverse voltage can be measured that is perpendicular to both the flow of current and field.[45] This phenomenon has become known as the ordinary Hall effect and can be described by a Lorentz force acting on the charge carriers within the conductor. It follows that this force acts in opposite directions for charge carriers of different sign.

Hall subsequently discovered a similar effect in ferromagnetic materials, whereby the transverse current is also dependent on the magnetisation of the material in which the current flows.[46] This has since become known as the Anomalous Hall Effect (AHE), and is seen to be larger than the ordinary Hall effect (sometimes orders of magnitude). The underlying mechanism for this effect is generally accepted as spin-orbit coupling, leading to a spin-dependant scattering. However much debate remains as to the intrinsic and extrinsic contributions.[47]

2.7.2 Spin Hall Effect

Nearly a century later in 1971, it was predicted that an unpolarised spin current could lead to a transverse spin current in materials with a strong spin-orbit interaction.[48] Here electrons can be separated based on the orientation of their spins, this is analogous to the way the Hall effect separates charge carriers. This phe-

nomenon has been come to be known as the Spin Hall Effect (SHE)[49] and was successfully measured in 2004 using Scanning Kerr Microscopy[50]and in a p-n junction device.[51]

The SHE of a material can be characterised by the so-called Spin Hall angle

$$\Theta_{SH} = \frac{J_{Spin}}{J_{Charge}} = \frac{\sigma^s_{xy}}{\sigma^c_{xx}} \frac{e}{\hbar}, \tag{2.35}$$

where σ^s_{xy} is the transverse Spin Hall conductivity (which represents the transverse spin current generated in response to an electric field) and σ^c_{xx} the longitudinal charge conductivity. Both of these properties are intrinsic to the material.[52] Typically, Spin Hall angles are given in percentages, where a positive angle indicates the spin accumulation follows the right hand rule.

The platinum Spin Hall angle is often quoted as 6%, despite a [3]range of reported values it is higher than that of many other commonly used metals.

This, together with the high conductivity and ease of synthesis, platinum is frequently used for exploiting the SHE. However, work continues to look for materials with higher Spin Hall angles, with angles as high as $|\Theta_{SH}| = 33\%$ being observed in tungsten.[53]

The SHE is purely a quantum mechanical phenomenon as it arises from the spin-orbit interaction. While still an active area of research, three underlying mechanisms have been described that can contribute to both the SHE and the anomalous Hall effect. These mechanisms are described below and illustrated in figure 2.5.[47,52]

Spin Skew Scattering - Spin-orbit coupling causes an effective magnetic field gradient, particles of opposite spins experience opposite forces and hence possess different *momentum*. This gives rise to spin Hall effects in isotropic media.

Side Jump Scattering - During scattering particles will experience both acceleration and deceleration, dependant on the orientation of their spin. Particles that undergo scattering from spin-orbit coupled impurities acquire a transverse

[3]measured values vary between 1-11%[52]

displacement.

Intrinsic Effects - This refers to mechanisms that result in spin-dependent particle velocities. Specifically these mechanisms originate from the effect that spin-orbit coupling has on the electronic band structure.

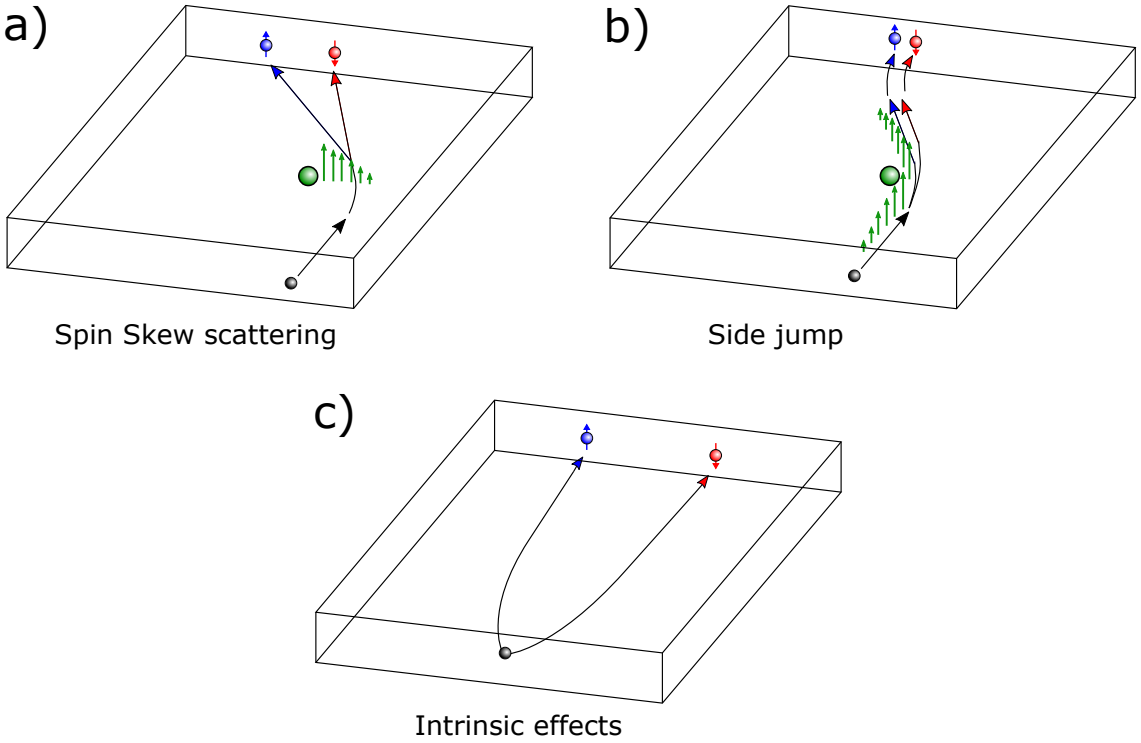

Figure 2.5: Schematic depicting mechanisms that contribute to both the Spin Hall and Anomalous Hall effects. a) Spin Skew Scattering, the spin orbit coupling gives rise to an effective field gradient, represented by the green arrows. b) Side jump occurs due to spin-dependant acceleration and deceleration (represented by green arrows) during scattering from spin-orbit coupled impurities. c) Intrinsic Spin Hall Effects, which occur between scattering events. Reproduced from [52]

Spin Skew and Side Jump Scattering are referred to as extrinsic effects that happen during particle scattering, while Intrinsic effects act on particles between scattering events.

A model has been used that compares the band structure with and without the spin-orbit interaction in 4d and 5d transition metals.[52,54] Here it has been shown that the spin-orbit interaction leads to a splitting of the band structure, resulting in an increased transverse conductivity σ^s_{xy}. It should be noted that the band structure is not spin split, and that there is no net spin polarisation on parts of the

band. These calculations reproduce the negative Spin Hall angle observed for materials with less than half filled d-orbitals, and the positive Spin Hall angle for materials with greater than half filled d-orbitals.

Furthermore, it is suggested that the Spin Hall conductivity is temperature dependent, whereby an increase in temperature results in a decrease in spin Hall conductivity due to different contributions from parts of the band structure. Such a dependence should be considered during the design of devices that exploit the SHE, as this may dictate a maximum temperature above which operation is not possible.

2.7.3 Rashba Effect

An alternative contribution for the AHE was proposed in 1984 by Bychkov and Rashba,[55] whereby two-dimensional systems with a lack of inversion symmetry[4] give rise to a transverse conductivity.[47] Electrons moving in an electric field experience a magnetic field in their frame of motion,[16] this field arises from the spin-orbit interaction and couples to the electron's magnetic moment.[56]

When an electron with momentum $\boldsymbol{p}$ moves in a magnetic field $\boldsymbol{B}$, it experiences a Lorentz force in the direction perpendicular to its motion

$$\boldsymbol{F}_{Lor} = \frac{-e}{m_e}\boldsymbol{p} \times \boldsymbol{B}, \tag{2.36}$$

and possesses Zeeman energy [5]

$$\epsilon_z = \mu_B \boldsymbol{\sigma} \cdot \boldsymbol{B}, \tag{2.37}$$

with $\boldsymbol{\sigma}$ the electron spin. If we instead consider an electron moving in a *electric* field $\boldsymbol{E}$, then by symmetry an effective field can be expected in the $\boldsymbol{p} \times \boldsymbol{E}$ direction. This translates into an effective field

[4] Molecules with inversion symmetry have the same structure when each atom is transposed through a single point. Broken inversion symmetry can arise within either bulk samples or at the interface of a film.

[5] note this is a conversion of equation (2.25) from CGS to SI units

$$\boldsymbol{B}_{eff} \sim \frac{1}{m_e c^2} \boldsymbol{E} \times \boldsymbol{p}. \tag{2.38}$$

This is the field experienced by the electron in its reference frame. By substitution of equations (2.38) into (2.37), the Zeeman energy induced by SO coupling can be formulated as a Hamiltonian

$$\mathcal{H}_{SO} \sim \frac{\mu_B}{m_e c^2} \boldsymbol{\sigma} \cdot (\boldsymbol{E} \times \boldsymbol{p}). \tag{2.39}$$

In the Rashba effect, broken inversion symmetry at the interface of two layers leads to an electric field close to the interface. In thin films, a significant portion of the charge current experiences the induced electric field, leading to the spin polarisation of the incident current. This effect has been demonstrated in many systems alongside the SHE.[57]

2.7.4 Spin Transfer Torque & its Application

It is possible for a current of spin-polarised electrons to transfer angular momentum to the magnetisation of a ferromagnet, this concept was proposed independently in 1996 by Berger[58] and Slonczewski.[59] The resulting torque on a magnetisation can be included in the Landau-Lifshitz-Gilbert equation[27,60,61]

$$\frac{d\boldsymbol{M}}{dt} = -\gamma(\boldsymbol{M} \times \boldsymbol{H}) + \frac{\alpha}{M_s} \boldsymbol{M} \times \frac{d\boldsymbol{M}}{dt} + \boldsymbol{\tau}_{STT}, \tag{2.40}$$

where $\boldsymbol{\tau}_{STT}$ represents the Spin Transfer Torque (STT). In general STT takes the form of “damping-like” and/or “field-like” torques. $\boldsymbol{\tau}_{STT}$ can be written as

$$\boldsymbol{\tau}_{STT} = A(\boldsymbol{M} \times [\boldsymbol{\sigma} \times \boldsymbol{M}]) + B(\boldsymbol{\sigma} \times \boldsymbol{M}), \tag{2.41}$$

for A and B amplitudes of the damping-like and field-like torques respectively. The names of these torques can be understood by comparing each torque to the field and damping terms in equation (2.40), and are also graphically represented in figure 2.6.

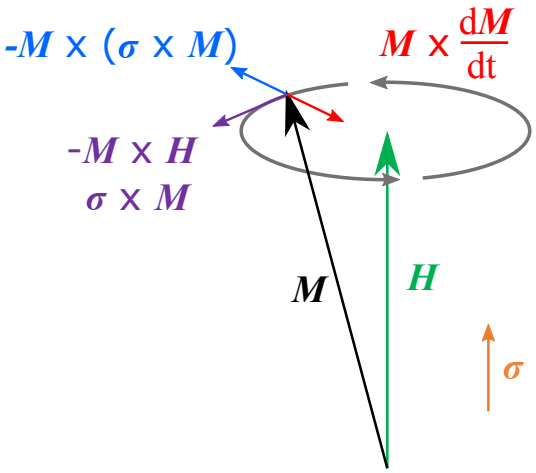

Figure 2.6: Depiction of the terms in equations (2.40) and (2.41), indicating the direction of spin and field torques acting on the magnetisation.

In order to exploit STT a large variety of device structures and measurement geometries have been considered, such as to drive spin currents into a magnetic layer sufficient to excite dynamic phenomena.[38] Initially tri-layer (or "Spin Valve") structures were used to explore the effects of STT. These structures consisted of two magnetic layers with a non-magnetic spacer layer in-between. One magnetic layer is designated the fixed layer which is maintained at a constant magnetisation. Electrical current passing vertically through the stack becomes spin polarised parallel to the fixed layer magnetisation (a process called spin filtering). For a sufficiently thin spacer layer (less than the spin diffusion length) this *spin polarised current* injects both charge and angular momentum into the free magnetic layer. The structure is designed such that the fixed layer magnetisation is static and that the free layer's magnetisation may be aligned non-parallel to the fixed layer. As a result, the spin polarised current transfers angular momentum to the free layer, the magnetisation of which will then begin to precess.

Oscillators based on such a method of generating STT have been studied since the late 1990's and continue to be of academic interest.[5,62] During the same period the SHE effect was being studied for generating STT, however, it was not until the late 2000's that the SHE and Rashba effects were exploited to drive

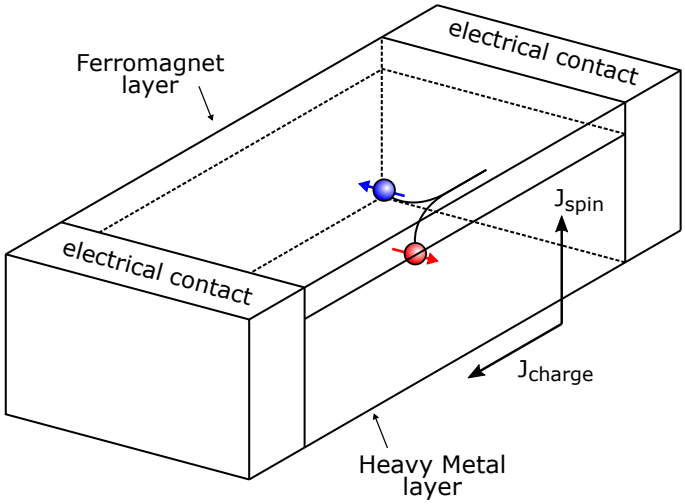

Figure 2.7: Schematic of a SHE device, consists of bi-layer of heavy metal and ferromagnet and electrical contacts. Charge current (J_{charge}) flowing through the heavy metal layer undergoes the SHE generating a vertical spin current (J_{spin}) into the ferromagnet layer.

precessional dynamics or current induced switching.[6,39,52,61] In these devices a current is applied along a thin heavy metal film, allowing a *pure spin current* to be injected vertically into an adjacent magnetic layer, carrying angular momentum without charge. Figure 2.7 demonstrates how the flows of charge and spin can be decoupled in this way. The SHE is thought to generate a damping-like torque (also known as "Slonczewski torque") and the Rashba effect is thought to produce a transverse field-like torque. Devices constructed in this way confer a number of advantages. They allow for direct optical access to the magnetic layer, a feature which was difficult in spin valve structures due to the placement of electrical contacts. In addition, since the material no longer needs to be conductive, materials can be selected purely for their magnetic properties.

CHAPTER 3

Experimental Techniques

3.1 Measurement of Spin-Torque FMR

In section 2.5.1 the excitation of Ferromagnetic resonance (FMR) by use of DC and AC magnetic fields was discussed. In addition, it is possible to excite FMR by the transfer of angular momentum from a spin current.[63–65] This spin current acts against the damping of magnetic precession at the onset of FMR. However, the generation of a spin current requires a large charge current, as such large Oersted fields are present in most applications. As a result the equation of motion for the precession of the magnetisation under the action of both a spin torque and an Oersted field is given by[66]

$$\frac{d\boldsymbol{m}}{dt} = -\gamma \boldsymbol{m} \times \boldsymbol{H}_{eff} + \alpha \boldsymbol{m} \times \frac{d\boldsymbol{m}}{dt} + \gamma \frac{\hbar}{2e\mu_0 M_S T} J_{S,rf} [\boldsymbol{m} \times (\hat{\boldsymbol{\sigma}} \times \boldsymbol{m})] - \gamma \boldsymbol{m} \times \boldsymbol{H}_{rf}, \quad (3.1)$$

where $\boldsymbol{m}$ is the unit vector of magnetisation, t is time, γ is the gyromagnetic ratio, $\boldsymbol{H}_{eff}$ is the effective magnetic field, α the Gilbert damping parameter, $\hbar$ the reduced Plank constant, e the charge of an electron, μ_0 the permeability of free space, M_S the saturation magnetisation, T the thickness of the magnetic layer, $J_{S,rf}$ the RF spin current density, $\hat{\boldsymbol{\sigma}}$ the unit vector for the direction of the injected spin moment, and $\boldsymbol{H}_{rf}$ the RF Oersted field.

AC current injected into the device results in an AC Oersted field and an AC spin torque, these two mechanisms cause the sample magnetisation to precess at the FMR frequency. In samples with magnetoresistive properties (such as AMR described in section 2.6), the precession of magnetisation can be observed as an RF emission. This emission mixes with the applied microwave current and (as $2cos^2(\theta) = cos(2\theta) + 1$) this yields a DC voltage that can be detected at the onset of FMR. This mixing voltage can be formulated as the sum of a symmetric and asymmetric Lorentzian function[63,66]

$$V_{mix} \propto A\frac{\Delta^2}{\Delta^2 + (H_{ext} - H_0)^2} + B\frac{\Delta(H_{ext} - H_0)}{\Delta^2 + (H_{ext} - H_0)^2}, \tag{3.2}$$

where A and B represent amplitudes for the symmetric and asymmetric functions respectively. Δ represents the linewidth of the resonance, H_0 the resonance field and H_{ext} the external field strength. In systems where there is no contribution from Spin-torque $A = 0$ and the mixing voltage takes the form of an asymmetric Lorentzian function. As a result, this provides a method for determining the relative strength of spin torque and the torque due to Oersted field. Figure 3.1 shows the contributions from both terms in equation (3.2) for a general case, with parameters listed in the figure caption.

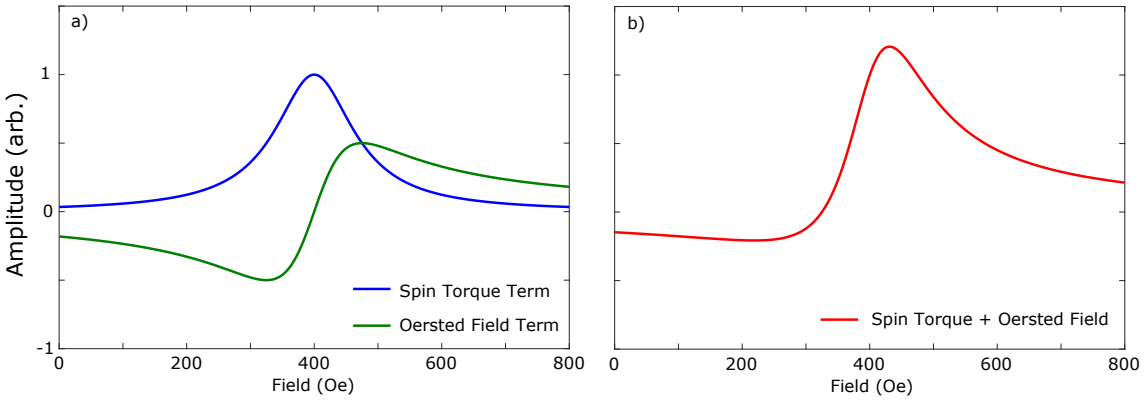

Figure 3.1: Plot of terms in equation (3.2) for a general case, a) showing the separate contributions of Spin Torque and Oersted Field, and b) a curve with the terms combined. For A = B = 1, Δ = 75 Oe, and H_0 = 400 Oe.

While devices that are purely driven by spin torque or Oersted fields may produce resonance curves like those in 3.1a, most realistic devices will exhibit

both mechanisms and produce a curve like that in 3.1b. This figure considers a device where the spin torque and Oersted fields are of equal proportion, this is not necessarily true for realistic devices. The magnitude of the mixing voltage can be observed to be on the order of a μV, and as a result measurements commonly employ lock-in techniques to improve the signal to noise ratio. A schematic of a typical experimental setup can be seen in figure 3.2.

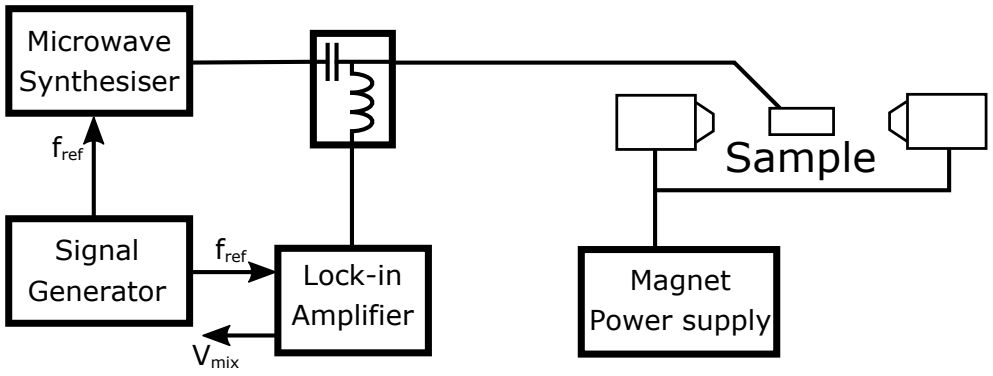

Figure 3.2: Experimental setup for the measurement of Spin-torque FMR. Microwave Synthesiser supplies RF current to sample generating both spin torques and an Oersted field, DC mixing voltage can be simultaneously read via a bias tee by a lock-in amplifier. Signal generator supplies a reference frequency of 3.14... kHz, RF current undergoes amplitude modulated at this frequency.

During experimentation the magnetisation is orientated so as to maximise the AMR signal generated. A microwave signal at a fixed frequency is passed through the sample, while the amplitude of the external field was allowed to vary. A bias-tee separates the AC and DC signals, and is setup such that a change in DC voltage at the modulation frequency can be detected by a lock-in amplifier. An additional current source can be used as a DC bias current for investigations of spin torque.[67]

This technique can be used to quantify the FMR of a spintronic device. As discussed in section 2.5.2, the FMR frequency vs field curve is useful in order to obtain material parameters, and hence is of significance in the characterisation of spintronic oscillators.

3.2 Analytical Expressions for FMR

As shown in section 3.1, STT-FMR is a powerful technique for measuring FMR and the torques present in spintronic devices. As will be shown in chapter 4 it is possible to perform similar measurements with TRSKM. By using the optical probe of the TRSKM the capabilities of STT-FMR can be expanded by adding spatial resolution to investigate local effects. This chapter required the derivation of analytical expressions for the resonance curves of the out of plane component of magnetisation. The derivations of these equations is detailed below.

Starting from the work outlined in reference [63], a spin valve is considered with a fixed layer (to generate spin polarised current through spin filtering) with orientation $\hat{\mathbf{s}}_{pin}$ and free layer (where precession is driven) with orientation $\hat{\mathbf{s}}_{free}$. The sample is orientated in the $\hat{\boldsymbol{x}} - \hat{\boldsymbol{z}}$ plane with the $\hat{\boldsymbol{y}}$ axis normal to the plane. From this the LLG equation with anti-damping and field-like STT takes the form

$$\frac{d\hat{\mathbf{s}}_{free}}{dt} = \gamma\hat{\mathbf{s}}_{free} \times \mathbf{H}_{eff} + \alpha\hat{\mathbf{s}}_{free} \times \frac{d\hat{\mathbf{s}}_{free}}{dt} + \gamma STI(\hat{\mathbf{s}}_{free} \times [\hat{\mathbf{s}}_{free} \times \hat{\mathbf{s}}_{pin}]) + \gamma FTI(\hat{\mathbf{s}}_{free} \times \hat{\mathbf{s}}_{pin}), \quad (3.3)$$

where t represents time, γ the gyromagnetic ratio, α the Gilbert damping constant, I the amplitude of RF current, ST and FT the amplitude of anti-damping and field-like STT respectively. $\boldsymbol{H}_{eff}$ is the total effective field acting upon the magnetisation, which can be written as

$$\mathbf{H}_{eff} = \mathbf{H}_{ext} + H_d(\hat{\boldsymbol{y}} \cdot \hat{\mathbf{m}})\hat{\boldsymbol{y}} + \mathbf{h}, \quad (3.4)$$

where $\mathbf{H}_{ext}$ is the static applied field, H_d is the out of plane demagnetising field, and $\mathbf{h}$ is the local Oersted field generated by the RF current.

For small driving fields we can assume a small amplitude of precession, and define $\hat{\mathbf{s}}^{(0)}_{free}$ as the free layer equilibrium orientation. The RF driving current can be written as

$$I = I_{RF}e^{i2\pi ft}, \quad (3.5)$$

and alternating Oersted field

$$\mathbf{h} = \mathbf{h}_0 e^{i2\pi ft}, \tag{3.6}$$

for f the RF frequency. It is convenient to consider three orthogonal unit vectors in terms of $\hat{\mathbf{s}}_{free}^{(0)}$ and $\hat{\mathbf{s}}_{pin}$, as opposed to Cartesian co-ordinates. Hence

$$\hat{\mathbf{e}}_1 = \hat{\mathbf{s}}_{free}^{(0)},\ \hat{\mathbf{e}}_2 = \frac{\hat{\mathbf{s}}_{free}^{(0)} \times \hat{\mathbf{s}}_{pin}}{sin(\theta)},\ and\ \hat{\mathbf{e}}_3 = \frac{\hat{\mathbf{s}}_{free}^{(0)} \times (\hat{\mathbf{s}}_{free}^{(0)} \times \hat{\mathbf{s}}_{pin})}{sin(\theta)}, \tag{3.7}$$

for θ as the angle between $\hat{\mathbf{s}}_{free}^{(0)}$ and $\hat{\mathbf{s}}_{pin}$. Given equations (3.5) and (3.7), an equation for $\hat{\mathbf{s}}_{free}$ can be constructed

$$\hat{\mathbf{s}}_{free} = \hat{\mathbf{e}}_1 + e^{i2\pi ft}(a\hat{\mathbf{e}}_2 + b\hat{\mathbf{e}}_3), \tag{3.8}$$

for a the amplitude of precession out of the plane ($\hat{\mathbf{e}}_2$ direction), and b the amplitude in-plane($\hat{\mathbf{e}}_3$ direction). Hence given equations (3.5),(3.6), and (3.8), each term in equation (3.3) can be calculated

$$\frac{d\hat{\mathbf{s}}_{free}}{dt} = i2\pi f e^{i2\pi ft}(a\hat{\mathbf{e}}_2 + b\hat{\mathbf{e}}_3) \tag{3.9}$$

$$\begin{aligned}\gamma\hat{\mathbf{s}}_{free} \times \mathbf{H}_{eff} = {} & \gamma i2\pi f e^{i2\pi ft}(a\hat{\mathbf{e}}_2 + b\hat{\mathbf{e}}_3) \cdot [\mathbf{H}_{ext} - H_d(\hat{\boldsymbol{y}} \cdot \hat{\mathbf{s}}_{free})\hat{\boldsymbol{y}} + \mathbf{h}_0]\hat{\mathbf{e}}_1 \\ & + \gamma(-\hat{\mathbf{e}}_3 + be^{i2\pi ft}\hat{\mathbf{e}}_1) \cdot [\mathbf{H}_{ext} - H_d(\hat{\boldsymbol{y}} \cdot \hat{\mathbf{s}}_{free})\hat{\boldsymbol{y}} + \mathbf{h}_0]\hat{\mathbf{e}}_2 \\ & + \gamma(\hat{\mathbf{e}}_2 - ae^{i2\pi ft}\hat{\mathbf{e}}_1) \cdot [\mathbf{H}_{ext} - H_d(\hat{\boldsymbol{y}} \cdot \hat{\mathbf{s}}_{free})\hat{\boldsymbol{y}} + \mathbf{h}_0]\hat{\mathbf{e}}_3\end{aligned} \tag{3.10}$$

$$\alpha\hat{\mathbf{s}}_{free} \times \frac{d\hat{\mathbf{s}}_{free}}{dt} = i2\pi\alpha f e^{i2\pi ft}(a\hat{\mathbf{e}}_3 - b\hat{\mathbf{e}}_2) \tag{3.11}$$

$$\begin{aligned}\gamma STI(\hat{\mathbf{s}}_{free} \times [\hat{\mathbf{s}}_{free} \times \hat{\mathbf{s}}_{pin}]) = {} & \gamma STI\{-be^{i2\pi ft}sin(\theta)\hat{\mathbf{e}}_1 \\ & + ae^{i2\pi ft}(cos(\theta) - be^{i2\pi ft}sin(\theta))\hat{\mathbf{e}}_2 \\ & + [sin(\theta) + be^{i2\pi ft}(cos(\theta) - be^{i2\pi ft}sin(\theta))]\hat{\mathbf{e}}_2\}\end{aligned} \tag{3.12}$$

$$\gamma FTI\{\hat{\mathbf{s}}_{free} \times \hat{\mathbf{s}}_{pin}) = \gamma FTI(-ae^{i2\pi ft} sin(\theta)\hat{\mathbf{e}}_1 + [sin(\theta) + be^{i2\pi ft} cos(\theta)]\hat{\mathbf{e}}_2 - ae^{i2\pi ft} cos(\theta)\hat{\mathbf{e}}_3\}. \quad (3.13)$$

Equations 3.9, 3.10, 3.11, 3.12, and 3.13 can be substituted into 3.3. After re-arranging and linearizing (i.e. ignoring terms quadratic in a or b) this yields the equation of motion

$$if \begin{bmatrix} a \\ b \end{bmatrix} = \begin{bmatrix} f_{11} & f_{12} \\ f_{21} & f_{22} \end{bmatrix} \begin{bmatrix} a \\ b \end{bmatrix} + \begin{bmatrix} 0 & -\alpha \\ \alpha & 0 \end{bmatrix} \begin{bmatrix} a \\ b \end{bmatrix} + \gamma' \begin{bmatrix} 0 & 1 \\ 1 & 0 \end{bmatrix} \begin{bmatrix} ST \\ FT \end{bmatrix} \begin{bmatrix} \gamma' \hat{\mathbf{e}}_2 \cdot \mathbf{h}_0 + STI_{RF} sin(\theta) \\ -\gamma' \hat{\mathbf{e}}_3 \cdot \mathbf{h}_0 + FTI_{RF} sin(\theta) \end{bmatrix} \quad (3.14)$$

where $\gamma' = \gamma/2\pi$,

$$f_{11} = \gamma' H_d (\hat{\mathbf{y}} \cdot \hat{\mathbf{e}}_2)(\hat{\mathbf{y}} \cdot \hat{\mathbf{e}}_3) \quad (3.15)$$

$$f_{12} = \gamma' \{\hat{\mathbf{e}}_1 \cdot \mathbf{H}_{ext} + H_d[(\hat{\boldsymbol{y}} \cdot \hat{\mathbf{e}}_3)^2 - (\hat{\boldsymbol{y}} \cdot \hat{\mathbf{e}}_1)^2]\} \quad (3.16)$$

$$f_{21} = \gamma' \{-\hat{\mathbf{e}}_1 \cdot \mathbf{H}_{ext} + H_d[(\hat{\boldsymbol{y}} \cdot \hat{\mathbf{e}}_1)^2 - (\hat{\boldsymbol{y}} \cdot \hat{\mathbf{e}}_2)^2]\} \quad (3.17)$$

$$f_{22} = -\gamma' H_d (\hat{\boldsymbol{y}} \cdot \hat{\mathbf{e}}_2)(\hat{\boldsymbol{y}} \cdot \hat{\mathbf{e}}_3) = -f_{11} \quad (3.18)$$

and with the static conditions

$$-\hat{\mathbf{e}}_3 \cdot \mathbf{H}_{ext} + H_d (\hat{\boldsymbol{y}} \cdot \hat{\mathbf{e}}_1)(\hat{\boldsymbol{y}} \cdot \hat{\mathbf{e}}_3) = 0 \quad (3.19)$$

$$\hat{\mathbf{e}}_2 \cdot \mathbf{H}_{ext} + H_d (\hat{\boldsymbol{y}} \cdot \hat{\mathbf{e}}_1)(\hat{\boldsymbol{y}} \cdot \hat{\mathbf{e}}_2) = 0. \quad (3.20)$$

These equations can be reduced by considering the case studied in chapter 4. Let the applied field be applied in the $\hat{\boldsymbol{z}}$ axis, it then follows that $\hat{\mathbf{e}}_1 = \hat{\boldsymbol{z}}$, $\hat{\mathbf{e}}_2 = \hat{\boldsymbol{y}}$,

and $\hat{\mathbf{e}}_3 = -\hat{\boldsymbol{x}}$. This immediately satisfies equations (3.19) and (3.20), and further reduces f_{11}, f_{12}, f_{21} and f_{22} to

$$f_{11} = 0 \tag{3.21}$$

$$f_{12} = \gamma'[H_{ext}] \tag{3.22}$$

$$f_{21} = -\gamma'[H_{ext} + H_d] \tag{3.23}$$

$$f_{22} = 0. \tag{3.24}$$

If the undriven and undamped case is considered (i.e. $|\mathbf{h}_0| = 0$ and $I_{RF} = 0$), one can re-arrange equation (3.14) to

$$\begin{bmatrix} (f_{11} - if) & f_{12} \\ f_{21} & (f_{22} - if) \end{bmatrix} \begin{bmatrix} a \\ b \end{bmatrix} = 0, \tag{3.25}$$

hence define for the present case

$$f_0^2 = -f_{11}^2 - f_{21}f_{12} = \gamma'^2 H_{ext}[H_{ext} + H_d], \tag{3.26}$$

returning to the equation of motion, equation (3.14) can be rearranged for the precession amplitudes a and b

$$\begin{bmatrix} a \\ b \end{bmatrix} = \frac{-1}{f_0^2 - f^2 + if\Delta} \begin{bmatrix} (if - f_{22}) & (f_{12} - if\alpha) \\ (f_{21} + if\alpha) & (if - f_{11}) \end{bmatrix} \begin{bmatrix} -\gamma'\hat{\mathbf{e}}_3 \cdot \mathbf{h}_0 + FTI_{RF}sin(\theta) \\ \gamma'\hat{\mathbf{e}}_2 \cdot \mathbf{h}_0 + STI_{RF}sin(\theta) \end{bmatrix}, \tag{3.27}$$

where

$$\Delta = -\gamma'\alpha(2H_{ext} + H_d), \tag{3.28}$$

which can be further re-arranged to

$$\begin{bmatrix} a \\ b \end{bmatrix} = -\frac{-f_0^2 - f^2 - if\Delta}{(f_0^2 - f^2)^2 + f^2\Delta^2} \begin{bmatrix} if\gamma' H_\perp + (\gamma' H_{ext} - if\alpha)\gamma' H_{||} \\ [-\gamma'(H_{ext} + H_d) + if\alpha]\gamma' H_\perp + if\gamma' H_{||} \end{bmatrix}, \tag{3.29}$$

for the effective fields

$$H_{\perp} = \hat{\mathbf{e}}_3 \cdot \mathbf{h}_0 + FTI_{RF}sin(\theta), H_{||} = \hat{\mathbf{e}}_2 \cdot \mathbf{h}_0 + STI_{RF}sin(\theta) \tag{3.30}$$

From here it is possible to obtain an expression for the voltage across a sample due to AMR. Equation (2.34) can be adjusted to the notation used here

$$R = R_{\perp} + \Delta R(\hat{\mathbf{s}}_{free} \cdot \hat{\mathbf{z}})^2 \tag{3.31}$$

While the time-varying voltage is given by

$$V = Re(I)Re(R). \tag{3.32}$$

By substitution of equations (3.8) and (3.31) into (3.32), one can calculate the time averaged voltage

$$\bar{V} = I_{RF}\Delta R|sin(\theta)|cos(\theta)Re(b) \tag{3.33}$$

Equations (3.29) and (3.33) are used later in chapter 4 to interpret the resonance curves from the out of plane component of magnetisation.

3.3 Magneto-transport techniques

For samples that possess magneto-resistive properties, it is possible to manipulate and characterise magnetic states through purely electrical methods. This allows for rapid characterisation of devices, without the need for optical apparatus. A schematic of a typical microwave spectroscopy setup for the excitation and measurement of spin waves is presented in figure 3.3. However, specific setups vary based on the device layout and the property to be measured.

A bias tee (AtlanTec AS3632) separates the AC and DC currents. The DC arm connects a current source (Keithley 6221) and nanovoltmeter (Keithley 2182A) to

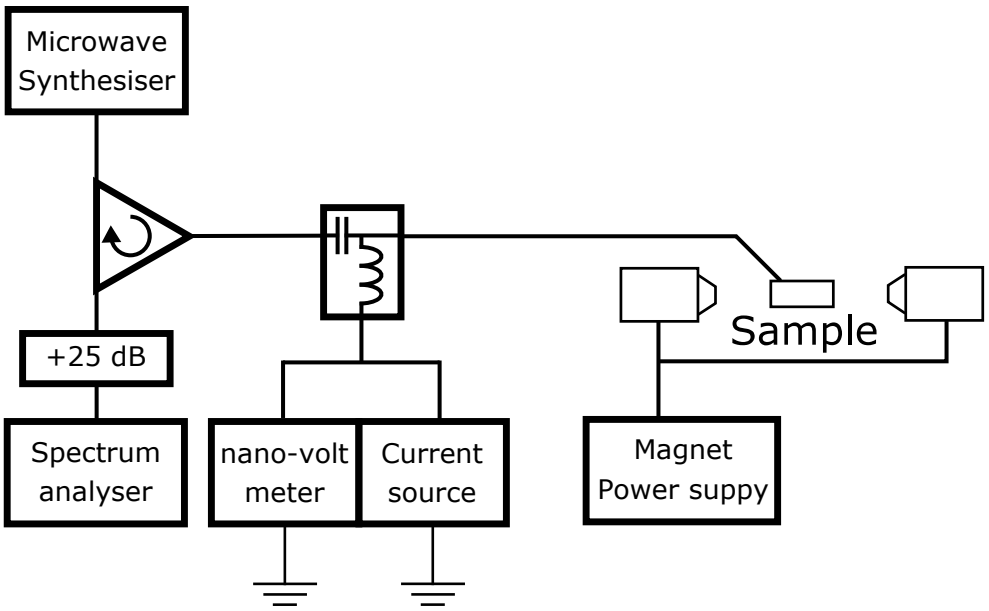

Figure 3.3: Diagram of a microwave spectroscopy setup for simultaneously supplying and measuring both DC and RF currents, with an electromagnet to drive a bias field. Nano-volt meter and current source are both connected to the inductive (DC) arm of the bias tee and grounded, enabling the injection of current and measurement of DC voltage across the sample. A circulator separates the flow of RF current, such that emission from the microwave synthesiser is passed to the device, while any emission from the sample is passed on to a spectrum analyser (via a +25 dB amplifier).

the device. The AC arm is connected to a circulator (AtlanTec ACC-20130-SF-SF-S), allowing the Microwave Synthesiser (Rohde and Schwarz SMF100A) to directly supply RF current to the sample while the Spectrum analyser (Agilent E4448A) simultaneously measures amplified emission (AtlanTec AS7265 +25 dB amplifier). A bespoke electromagnet supplies a bias field the magnitude and orientation of which can be controlled.

3.4 Magneto-Optical Kerr Effect

In 1846 Faraday observed that light passing through a magnetic material will undergo a rotation of the plane of its polarisation. The size and direction of this change in polarisation is dependent on the medium through which the light is transmitted and its magnetisation. This phenomenon is referred to the Faraday

effect,[68] and was rarely implemented as few magnetic materials are transparent. In 1876, John Kerr observed that the same was true of light reflected from a magnetic material.[69] While this allowed a much larger variety of materials to be studied it would take a further 75 years for the Magneto-Optical Kerr effect (or MOKE) to be used in the observation of magnetic structure in magnetic materials.[14,70]

Linearly polarised light can be described as the superposition of two circularly polarised modes. Linearly polarised light propagating within a magnetic medium undergoes a rotation in polarisation due to a phase shift between the two circularly polarised modes. However, light reflected from the surface of the ferromagnetic material may also become elliptically polarised, due the different reflection coefficients for the different circular modes. Both effects typically exist in a magnetic material.

Phenomenologically, the magneto-optical effects (including effects other than the Faraday and MOKE effects) arise due to the spin-orbit interaction, and can be described using a generalized permittivity tensor[14,71]

$$\boldsymbol{\epsilon} = \epsilon \begin{bmatrix} 1 & -iQ_V m_z & iQ_V m_y \\ iQ_V m_z & 1 & -iQ_V m_x \\ -iQ_V m_y & iQ_V m_x & 1 \end{bmatrix} + \begin{bmatrix} B_1 m_x^2 & B_2 m_x m_y & B_2 m_x m_z \\ B_2 m_x m_y & B_1 m_y^2 & B_2 m_y m_z \\ B_2 m_x m_z & B_2 m_y m_z & B_1 m_z^2 \end{bmatrix}, \tag{3.34}$$

where Q_V is the Voigt material constant and describes the magneto-optical rotation of the plane of polarisation, i.e. the Faraday and Kerr effects. m_x, m_y & m_z describe directional cosines of magnetisation, as such $m_x^2 + m_y^2 + m_z^2 = \boldsymbol{m}^2 = 1$ where $\boldsymbol{m}$ is the magnetisation unit vector. Constants B_1 and B_2 describe quadratic magneto-optical effects (such as the Voigt and Cotton-Mouton effects) that won't be discussed in this thesis, but have been included for completeness. These constants are not known for the majority of materials.

The resulting electric displacement vector $\boldsymbol{D}$ is related to the electric field $\boldsymbol{E}$ and permittivity tensor by

$$\boldsymbol{D} = \boldsymbol{\epsilon}\boldsymbol{E}. \tag{3.35}$$

It can be see from equations (3.34) and (3.35) that the nature of the Kerr effect is dependent on the relative orientations of $\boldsymbol{E}$ and $\boldsymbol{m}$. As a result the MOKE can be considered in three distinct geometries. Figure 3.4 depicts the geometries of the Polar, Longitudinal and Transverse MOKE. These geometries are defined by the

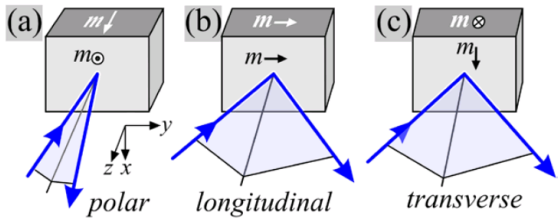

Figure 3.4: Diagram of the three MOKE geometries. a) Polar MOKE, where the magnetisation points along the surface normal, is maximised for small angles of incidence. b) Longitudinal MOKE, where magnetisation lies parallel to the surface and *within* the plane of incidence. c) Transverse MOKE, where magnetisation is also parallel to the surface but *perpendicular* to the plane of incidence, is also maximised for large angles of incidence. It is only observed for P-polarised light, where a change in amplitude can be measured. Reproduced from [71].

orientation of the magnetisation relative to the plane of incidence and that of the reflective surface. The effect of the spin-orbit interaction can be described as an effective magnetic field. This field mimics the Lorentz force where $\boldsymbol{F} = q\boldsymbol{v} \times \boldsymbol{B}$. Linearly polarised light incident on a material's surface causes the electrons to oscillate parallel to the plane of polarisation $\boldsymbol{E}$. The electrons in the material will experience a magnetic field from the material's magnetisation $\boldsymbol{m}$, and hence will experience a secondary motion in the direction of $\boldsymbol{E} \times \boldsymbol{m}$ (i.e. $\boldsymbol{v} \rightarrow \boldsymbol{E}$ and $\boldsymbol{B} \rightarrow \boldsymbol{m}$). In the case of Polar and Longitudinal geometries with incident light being S or P-polarised, this secondary motion results in the returning light possessing a degree of rotation and ellipticity. However for the transverse case, S-polarised light will experience no change while P-polarised light will exhibit a variation in amplitude. This variation does not produce a contrast large enough to be observed

conventionally (i.e. with the naked eye), but is observable experimentally. Each MOKE geometry has a dependence on the angle of incidence, that arises from the nature of the Lorentz force. The Longitudinal and Transverse MOKEs are maximized for a large angle of incidence, while the Polar geometry is largest when light is near to normal incidence. This dependence needs to be considered when using the MOKE in the measurement of magnetic materials.

3.5 Time-Resolved Scanning Kerr Microscopy

By using a pulsed laser the MOKE can be used to investigate dynamic magnetic phenomena, where the temporal resolution is limited by the laser pulse width. With further addition of a scanning stage, the spatial properties of such dynamics may be investigated with a resolution primarily limited by the size of the optical probe. Apparatus designed to exploit the MOKE in this way forms a Time-Resolved Scanning Kerr Microscope (or TRSKM), which is a powerful tool for furthering our understanding in magnetic processes on sub-nanosecond and sub-micron scales.

The description of this equipment will be divided into two parts, the first half will document the optical components, and the second half will encompass the three electrical setups used for experimentation in this thesis.

3.5.1 Optical Setup

The components responsible for directing and detecting the laser pulse are indicated in figure 3.5. A pump laser (Spectra-Physics Millennia Pro) produces a 5 W continuous wave beam at 532 nm that is directed into a laser oscillator (Spectra-Physics Tsunami), inducing a Ti:sapphire crystal to lase at 800 nm with a pulse width below 100 fs. The Tsunami is mode locked through Kerr lensing within the gain medium (note this phenomenon refers to the *optical* Kerr effect, as opposed to the MOKE), so that only the desired pulsed mode is transmitted.

The pulse frequency is synchronised to an external source at 80 MHz by use of a piezoelectric motor to manipulate one of the mirrors within the laser cavity (see section 3.5.2 for schematics of the electrical components). A flip-mirror can be used to divert the beam to a laser spectrum analyser for monitoring the Tsunami output and fine-tuning the cavity mirrors.

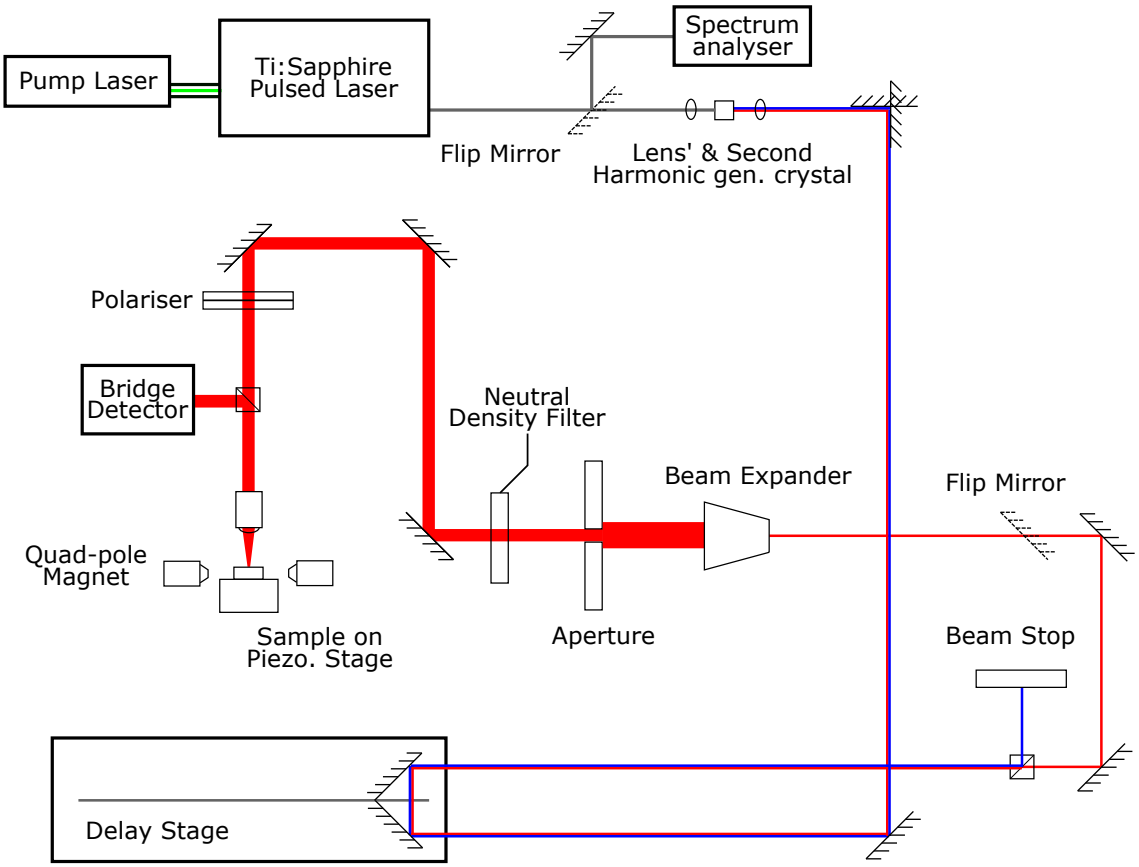

Figure 3.5: Schematic for the optical components in the TRSKM. Laser pulses are monitored with a laser spectrum analyser. Second harmonic generator crystal provides two wavelengths for measurement, separate colours are used to show the path of blue (400 nm) and 'red' (800 nm) beams. Delay stage allows the laser pulses to be delayed relative to electrical pulses. Wavelength splitter, beam stop, and flip mirrors allow the wavelength to be selected before beam enters a beam expander (in this figure the 'red' beam has been selected). Beam expander, aperture and neutral density filter prepare the beam's power and spot size before entering the microscope. Within the microscope, the beam passes through a polariser and is focused onto the sample. The beam is positioned on the sample using a piezoelectric stage, and a bridge detector measures the change in polarisation of the reflected light.

The laser beam is subsequently focused onto a second harmonic generator

crystal, this reduces the intensity of the 800 nm beam but produces an additional blue beam (400 nm). The desired wavelength can be selected by use of a wavelength splitter, flip-mirror and beam-stop later in the beam path. Results in this thesis were performed at a wavelength of 800 nm due to the higher intensity relative to the 400 nm output. The beam was subsequently directed onto a retro-reflector mounted on a translational stage, which acts as a delay line with a maximum delay of 4 ns. The laser pulse then passes through a beam expander, aperture and neutral density filter. These components allow the beam size and power to be configured prior to entering the microscope setup.

Once the beam enters the microscope setup it passes through a polariser to ensure linear polarisation. The pulse is then directed and focused through a microscope objective onto the sample. An objective with a large numerical aperture is preferred as this produces a high angle of incidence. This in turn allows for all three magnetisation components to be detected simultaneously (this will be discussed below). Reflected light is redirected through a beam splitter into the quadrant detector, which consists of a polarising beam splitter and two quadrant photo-diodes. Light incident on the detector is split by the beam splitter into orthogonal polarisation components, and each resulting beam is aligned onto a quadrant diode. By using quadrant photodiodes it is possible to infer the in-plane magnetisation, the mechanism for this will be described below.

In order to detect the Kerr rotation generated from three orthogonal components of magnetisation, we must consider the focused optical probe as depicted in figure 3.6. To recover the in-plane magnetisation one must consider the rotation experienced by different beam segments. For example, segments a & d $\rightarrow$ b & c will detect the longitudinal Kerr rotation due to $M_{\parallel}$ (the detector is insensitive to transverse Kerr effect due to $M_{\perp}$). Careful measurement of the polarisation change in each of these segments yields the in-plane magnetisation vector, while the out of plane (polar) magnetisation can be found by considering the reflection of the beam as a whole at normal incidence.

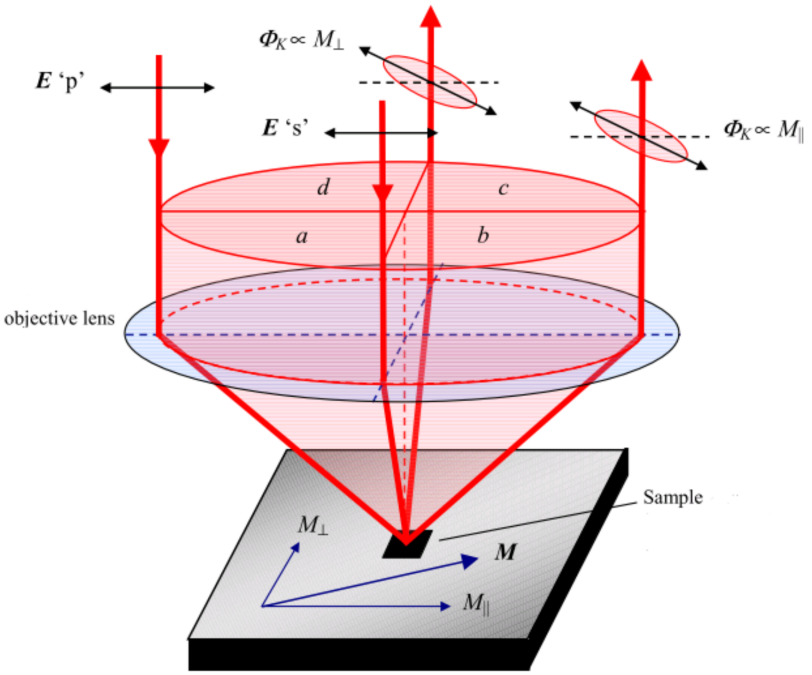

Figure 3.6: Diagram of focused optical probe for resolving in-plane magnetisation. Beam is divided into four quadrants, a, b, c, and d. Upon reflection these quadrants undergo the longitudinal Kerr rotation due to $M_\perp$ and $m_{||}$ componants of magnetisation $\boldsymbol{M}$. Reproduced from [72]

Hence to maximise the longitudinal Kerr effect a lens with a high numerical aperture is preferred, in order to increase the angle of incidence and hence better recover the in-plane magnetisation.

The sample is mounted on a Piezoelectric stage (Physik Instrumente E-515), by evaluating either static or time-resolved MOKE measurements at each point images of the static or dynamic magnetisation can be measured.

3.5.2 Electrical Equipment

Depending on the nature of the sample and experiment, various electronic configurations were utilized. Here, three setups will be considered for the observation of spin wave dynamics, pulsed excitation, and dynamics from a bi-polar pulse in an extended time-frame. As with all pump-probe experiments, each setup will feature a method for synchronising the driven dynamics to the laser repetition rate.

For observing dynamics driven by DC and RF currents

The configuration presented here can be used for the investigation of spintronic devices, though the principles discussed here apply to other experiments. Prior to TRSKM measurement, it must be demonstrated that the spin waves to be studied can be synchronised at a multiple of the laser repetition rate (80 MHz). To do this, magneto-transport methods are employed to identify the electrical current and magnetic field requirements to achieve synchronisation, a process referred to as injection locking (or phase locking).

Figure 3.7 illustrates the components required for delivering suitable DC and RF currents to a sample, as well as how each component is linked. To synchronise the laser and injected RF, a master clock (Atlantec low phase noise oscillation instrument) supplies RF to both the laser oscillator and an RF generator both of which lock to this signal. The RF generator subsequently produces synchronised RF at a frequency and amplitude determined from injection locking measurements.

However, there is one final step required in order to obtain time-resolved images. While static Kerr is sensitive to 10's of mDeg, lock-in amplifiers (EG& G Instruments 7265) can yield an order of magnitude improvement, as well as reduce background noise. To do this, the RF injected to the sample is modulated at a known frequency (3.14... KHz to avoid mains electricity or other noise). While it is sufficient to modulate amplitude (switching the RF between 'on' and 'off' states), phase modulation of π radians at the modulation frequency is preferred. This has the effect of alternating the device between displacements of $+ve$ and $-ve$ amplitude, effectively doubling the signal that can be obtained via the lock-in amplifiers.

The additional components depicted are mostly extensions of the magneto-transport experiments described earlier in section 3.3, allowing for injection and measurement of DC and AC currents. While the optical delay line is available (as shown in figure 3.5), the RF generator can induce an electrical delay without

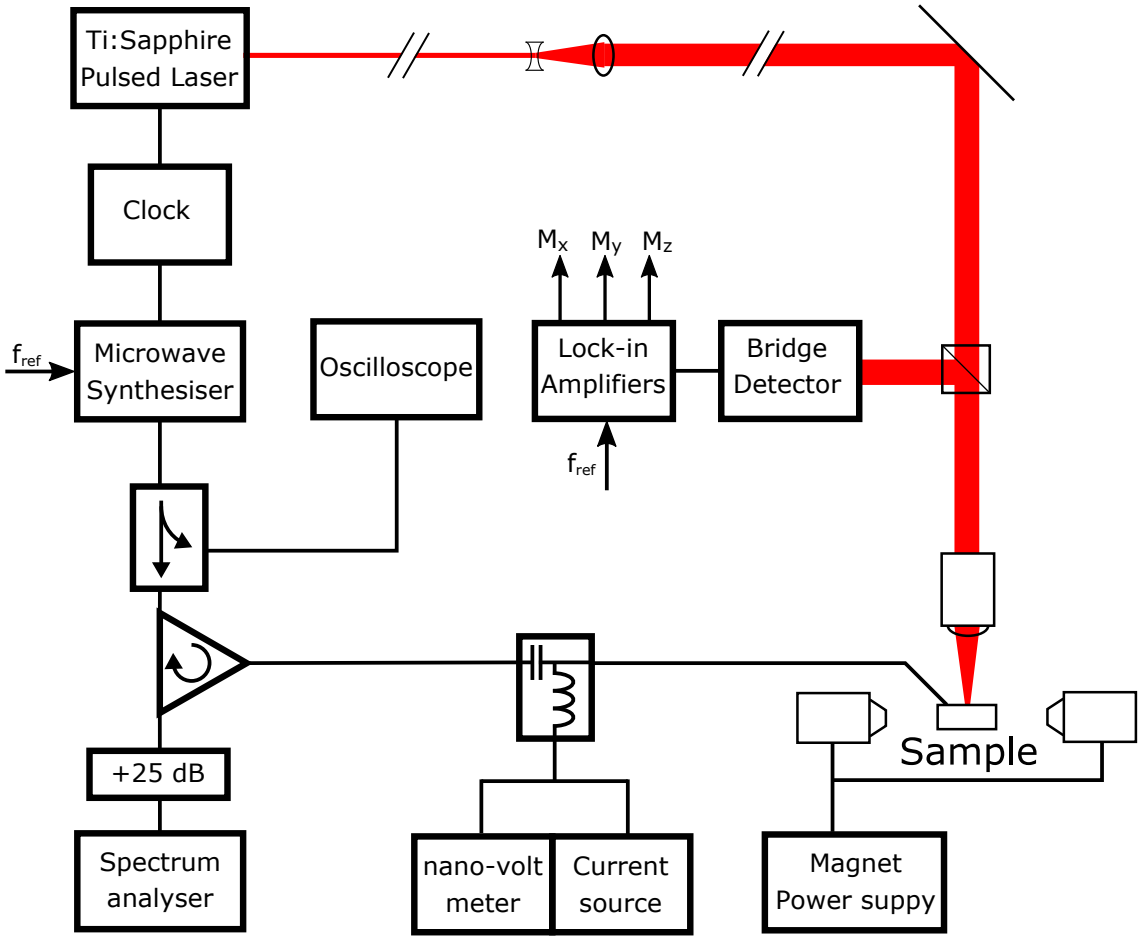

Figure 3.7: Diagram of optical and electrical equipment for TRSKM to drive and observe injection locked spin torque oscillators. Electrical equipment is similar to the magneto-transport in section 3.3. In addition, the RF current from the synthesiser can be monitored on an oscilloscope for phase drift and amplitude. The laser and synthesiser are locked to the same clock, while a reference frequency is supplied by a function generator (not shown) at 3.1415... kHz.

disturbing the optics. A sampling oscilloscope (Agilent Infinium DCA-J) takes a reduced signal from a directional coupler, allowing the injected signal to be monitored for phase drift.

For observing dynamics driven by ps electrical pulse

For other systems (for example hard drive write heads), it is more suitable to consider the magnetisation dynamics in response to an ultrafast electrical pulse. Such measurements can be performed with a setup described in figure 3.8. In

this case an electrical impulse generator (Pico Second Pulse Labs PSPL 3600) is synchronised to the laser clock and gated at the modulation frequency. The laser probe is delayed relative to the electrical pump by the optical delay line in figure 3.5.

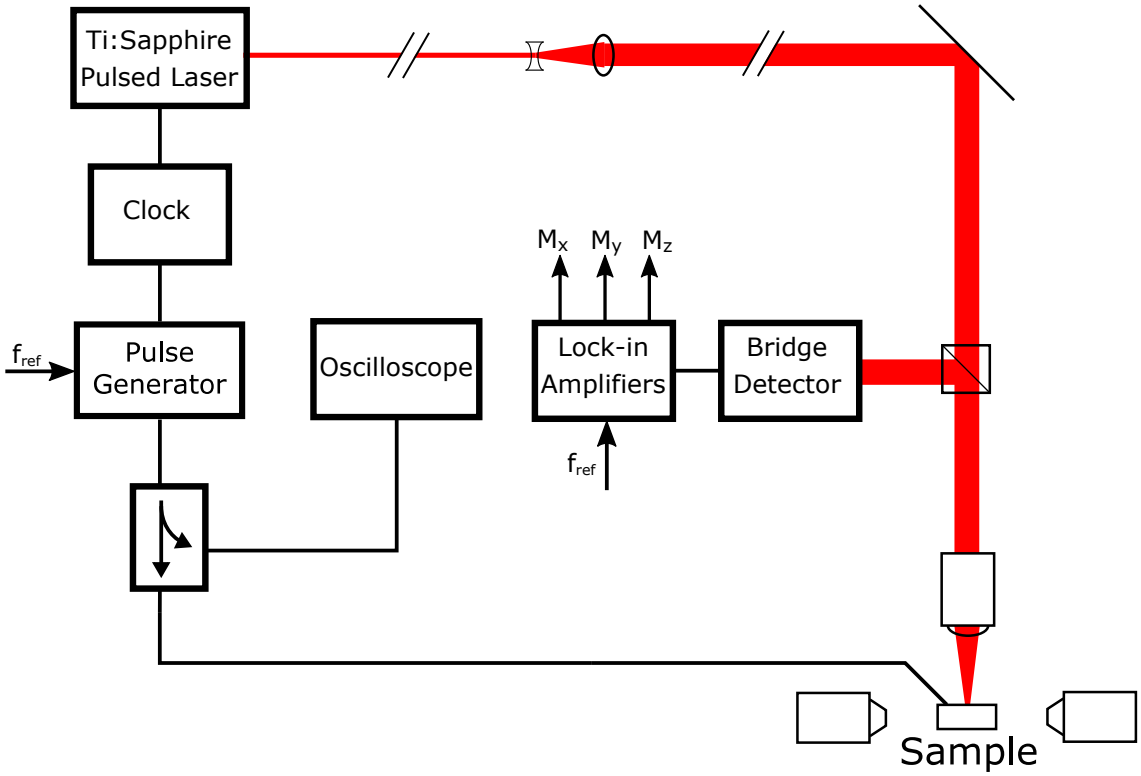

Figure 3.8: Diagram of TRSKM electrical equipment to inject electrical pulses into a sample. Pulse generator is synchronised to the laser with a clock, and modulated (or gated) at the reference frequency. The injected pulse is monitored on an Oscilloscope.

Laser pulse-picking and Bi-polar electrical pulses

For studying the switching of magnetic devices between two states with TRSKM, it is not suitable to inject a single electrical pulse. The stroboscopic nature of this experiment demands that in addition to a 'write' pulse a subsequent 'reset' pulse must be injected in order to return the device to its original state prior to the next laser pulse. For these measurements a setup similar to that shown in figure 3.9 is necessary.

To generate an sufficient ‘write’ and ‘reset’ pulse, an Avtech AVP-AV-HV3 Ultra High Speed Pulse Generator was used. The output is connected to a power divider, one pulse is unchanged and acts as the ‘write’ pulse, while the other passes through an electrical inverter and additional cable to create a delayed ‘reset’ pulse. The pulse transmitted from the sample is fed into an ultrafast oscilloscope for monitoring. The ‘write’ and ‘reset’ processes combined are expected to take longer than the repetition rate of the laser, hence it is necessary to reduce the repetition rate and trigger the pulse generator by some other means.

An ultrafast pulse picker (Con Optics 305 and 25D) serves to reduce the output of the laser system, such that only 1 in every 80 pulses are transmitted. This device takes the form of an electro-optic modulator with high-frequency electronics, when connected to the laser reference it will block all pulses except those at a specified multiple. In order to trigger the remaining electronics, a 90:10 beam splitter delivers a portion of the beam to an ultrafast photodiode. A directional coupler diverts part of the photodiode signal to the oscilloscope for monitoring, while the remainder is converted to a transistor-transistor logic (TTL) pulse, suitable for triggering the delay generator. The new laser repetition rate and bi-polar pulse necessitated the use of an electrical delay generator (Stanford Research Systems DG645), as it offered a significantly increased delay range over that of the optical delay line. A direct output was used to trigger the oscilloscope with a separate delayed output triggering the pulse generator. This approach allowed both the electrical and optical pulses to be simultaneously monitored, and suitable values for delay identified. In order to provide modulation, the delay generator output was gated using the reference frequency.

3.5.3 Discussion & Summary

TRSKM is not the only technique capable of observing dynamic magnetic phenomenon. Brillouin Light Scattering (BLS) allows the direct observation of spin

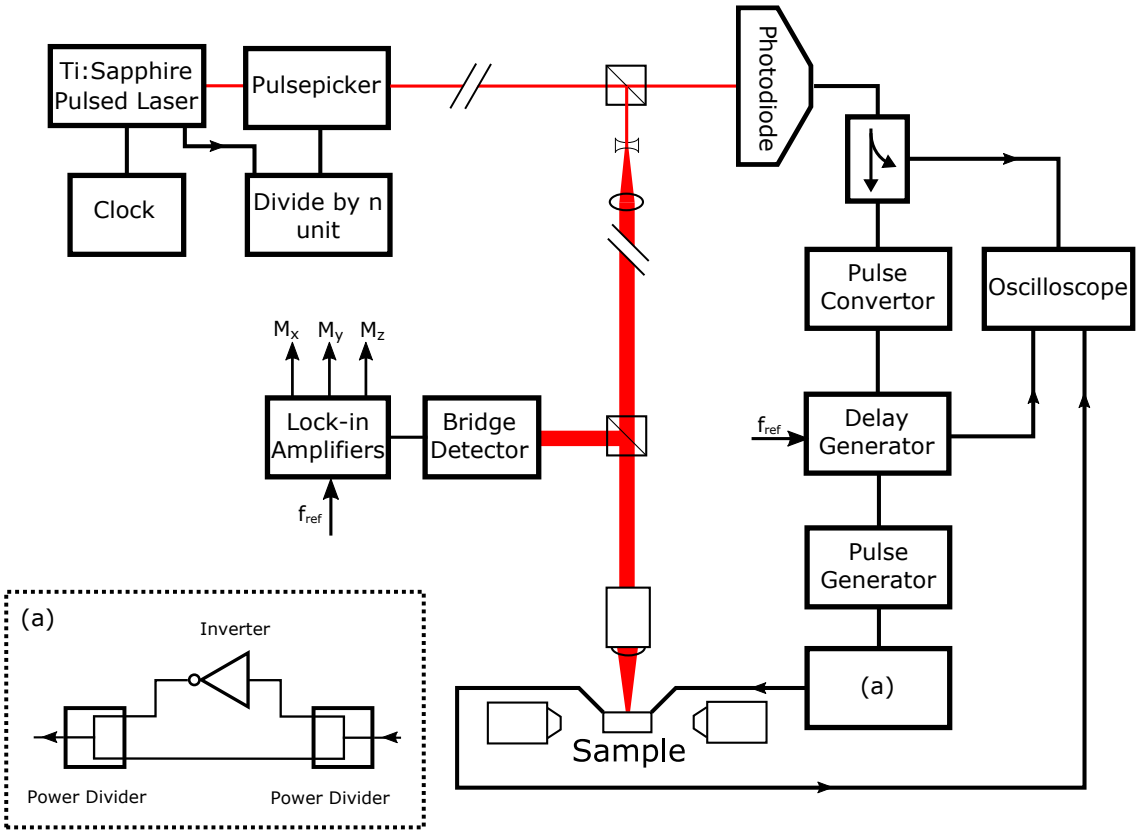

Figure 3.9: Diagram of additional optics and electrical equipment required to observe dynamics induced by bi-polar electrical pulse with large time delay. Laser repetition rate is reduced by a pulse picker to a specified number of pulses, synchronised to the pulsed laser. A photodiode serves as a new clock to trigger electronics. The electrical delay generator is gated at the reference frequency, and subsequently triggers a pulse generator. The electrical pulse is converted into a bi-polar pulse with the components shown in the inset (a).

waves by measuring the inelastic scattering of light from a magnon.[73] This method is highly sensitive to spin waves and capable of detecting thermal excitations, while retaining the ability to spatially map the spin wave modes (and is similarly limited by the focused beam spot size). X-ray microscopy is capable of imaging the magnetisation by recording the amount of X-rays absorbed in regions of a sample. While it has a lower temporal resolution, a spatial resolution of 100 nm or below can be achieved.[74] A distinct advantage that TRSKM has over these techniques is that it is capable of simultaneously detecting all three vector components of the magnetisation. This allows dynamics to be characterised in a way that is qualitatively different to either BLS or X-ray Spectroscopy.

The principle disadvantage of TRSKM is the typically long acquisition time, making it it vulnerable to drift and noise. Components heating up and shifting over time can result in changes in laser intensity due to beam drift, and sample drift can lead to disjointed or skewed images. Furthermore, sources of optical noise can lower the system sensitivity and disrupt the imaging process.

Despite these drawbacks TRSKM has become a powerful tool for observing magnetisation dynamics and is not limited to spin wave oscillations. This technique has long been used for aiding the development of read/write devices for magnetic storage[75,76] as well as investigating dynamics in a variety of magnetic nanostructures,[72] and the Spin Hall Effect.[50]

3.6 Methods for Micromagnetic simulations

3.6.1 Introduction

In recent years the simulation of static and dynamic magnetism has proved vital, not only for interpreting experimental results, but in predicting features or behavior that are not observable in experiment.[77,78] In the micromagnetic formalization, the magnetisation is discretized into computational cells, where the saturation magnetisation is assumed to be constant from cell to cell, and magnetisation unit vector ($\boldsymbol{m} = \boldsymbol{M}/M_s$) is calculated in each cell.

The typical length scales of samples used in this thesis (100's nm to 1's of μm) favour the use of micromagnetic simulations, however it should be noted that atomistic models are available for samples with smaller features.[79,80] While a variety of micromagnetic simulation packages are available, the work in this thesis employed MuMax3 GPU-accelerated micromagnetic simulation package (hereafter referred to as MuMax).[81] MuMax employs a finite-difference discretization with an adaptive time step in order to calculate dynamics for discrete computational cells.

The exchange interaction is incorporated as an effective field, specifically, by

Table 3.1: Specification table of GPUs employed in figure 3.10. Showing Release Year, Memory Size, number of CUDA cores, and Computation Capability.

Card Name	Release Year	Memory	CUDA Cores	Comp. Capability
Tesla K40c	2012	12 GB	2880	3.5
Quadro K5200	2014	8 GB	2304	3.5
GTX 970	2014	4 GB	1664	5.2

employing a 6-neighbour small angle approximation. Due to this approximation, the error between the simulated and exact exchange energy increases as the angle between neighbouring spins increases. In order to compensate for this, computational cells are typically of size smaller than the exchange length of that material, for systems of micron size cell counts can be expected to quickly reach the 1,000's or 10,000's. To reduce computation time, MuMax is accelerated by the use of Graphical Processing Units (GPUs), enabling calculations across large data sets to be carried out in parallel by use of the Compute Unified Device Architecture (or CUDA) developed by the Nvidia corporation. As a result, CUDA-enabled GPUs are required for MuMax.

The choice of GPU has a marked impact on simulation time. Within this thesis, two GPU clusters were employed, "Ragnarok" a system of GTX 970s, and "GPU Compute" with a Tesla K40c and Quadro K5200. Figure 3.10 compares the computation time for both systems with the same simulation, while the specification for each GPU is shown in table 3.6.1. Despite the fact that the GPU Compute system has cards with greater memory and more CUDA cores, Ragnarok yields improved simulation times, with a larger discrepancy observed for increased dynamics. CUDA-enabled GPUs are also assigned a Computation Capability score based on a number of factors, the higher score indicates improved throughput of cards for CUDA calculations.

While the GTX 970s have improved throughput, the higher memory of the Tesla and Quatro cards allows them to carry out simulations with a larger cell count. For the works presented here, the Ragnarok cluster was used to carry out

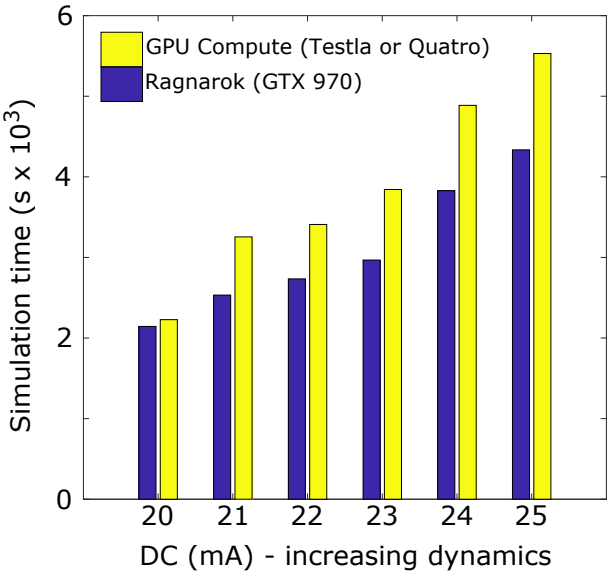

Figure 3.10: Comparison of GPUs, for a SHNO with 400 $\times$ 400 cells of increasing DC (leading to increased the magnetisation dynamics)

numerous simulations for a wide variety of parameters (current, magnetic field, spin Hall angle etc.) on a smaller sample. Once parameters of interest had been identified, the larger cards of the GPU Compute system were used to confirm the result for a larger sample.

3.6.2 Calculating Current and Oersted field distributions

For realistic micromagnetic simulations to be carried out, it is vital that the various torques within the magnetic layer are understood. In the case of Oersted fields and spin currents, COMSOL^{TM}finite element multiphysics package[82] can be used to calculate charge current distribution and the resulting Oersted field.

The construction of an idealised device geometry within COMSOL is relatively straight forward, however such an approach does not yield realistic results. To account for fabrication limitations it was necessary to apply rounding to the edges of electrical contacts. Similarly, for the accurate calculation of the Oersted field, it was necessary to encompass the simulated device within a cylinder of air. The vast majority of simulations carried out considered the effects of DC electrical currents injected into the device. A stationary solver was used in conjunction with

either the Electric Currents (ec) or Magnetic and Electric Fields (mef) modules. By applying an electric potential to opposing contact edges the static DC distribution and corresponding Oersted fields for DC currents were found.

A small number of simulations considered the effect of switching to a high frequency AC. For this, the Electron Waves (emw) module was used with a Frequency domain solver, with rectangular ports applied to the same electrical contacts. It should be noted that the results obtained in this way were highly dependent on material paramaters. Furthermore, it has been shown that for an accurate understanding of high frequency current within a device it is necessary to consider electrical loss due to all device components including the substrate.[83]

3.6.3 Calculating the magnetic response

The simulations employed consider a single thin magnetic layer exposed to spin currents and Oersted fields. While it is possible to incorporate additional layers in MuMax, it is significantly more efficient to consider a single magnetic layer one computation cell thick. To ensure accurate results the cell diameter was chosen to be smaller than the exchange length. Improved simulation run times were obtained for cell counts with a large number of factors (ideally base 2 numbers), resulting from memory allocation. Separate simulations were carried out to calculate the static magnetisation in the presence of any static field (bias fields and/or Oersted fields), which was subsequently imported as the start condition for subsequent dynamic simulations.

To exert STT, MuMax treats the system as a tri-layer spin-valve structure, with a pinned layer to polarise spin current passing vertically into the free layer. This spin current was given the spatial distribution found from COMSOL, with a polarisation predicted from the device geometry. In addition, the Oersted field obtained through COMSOL modelling was added to any static field. The simulation was configured

in order to control the spin current and Oersted field as either a DC excitation, or time-varying so as to mimic the injection of RF currents.

3.7 X-ray Photo-Emission Electron Microscopy

Just as scanning electron microscopes enable the imaging of structures below the limits of optical microscopy, X-ray photoemission microscopy (XPEEM) enables the measurement of magnetic structures at a spatial resolution below that of optical techniques. The technique relies on x-ray Magnetic Circular Dichroism (XMCD), whereby circularly polarised x-rays are preferentially absorbed by a magnetic sample based its magnetisation. The technique is element specific as absorption energies are specific to different chemical species, as a result the magnetic state of individual layers in multi-layer structures can be probed separately.

This technique requires intense polarised X-rays, the energy of which can be tuned. As a results these experiments are typically performed at a synchrotron light source, such as the BESSY II Synchrotron in Berlin.

In XPEEM, X-rays are focused onto the sample to a spot size on the order of $\sim$10s of μm, with a image resolution of $\sim$10s of nm. The spatial resolution of the electron microscope is limited by spherical aberration, chromatic aberration and diffraction, however in practice chromatic aberrations dominate.[16] Nevertheless a resolution of up to 4.1 nm can be achieved.[84] X-ray measurements do not form a major part of this thesis, a detailed description of the experimental setup goes beyond the scope of this thesis, for this references [84–86] should be reviewed. Suffice to say that electrons emitted from the sample are collected by an objective lens, pass through a contrast aperture and on to a detector. The objective lens in this case is a magnetic lens, while the aperture filters out electrons of too high energy. The detector itself can take the form of microchannel plates, a phosphor screen with CCD camera, or more recently solid state hybrid pixel

detectors (primarily the Medipix 2) which feature substantially lower background noise for measurements.[87] A variety of measurements can be carried out with this equipment. In addition to probing static magnetic configurations, the regular x-ray packets allow for time resolved measurements and x-ray detected ferromagnetic resonance.

CHAPTER 4

Spatial Mapping of Torques within a Spin Hall Nano-oscillator

4.1 Introduction

Spin torque oscillators (STOs)[5] are nanoscale magnetoresistive devices of great promise for use in microwave assisted magnetic recording,[4] microwave frequency telecommunications,[6] and neuromorphic computing.[88] Injection of DC current generates spin transfer torque (STT) that excites precessional oscillations of the constituent magnetic moments. The magnetoresistance (MR) therefore leads to an oscillatory voltage across the device. When STT suppresses damping a continuous oscillation is obtained, a process called auto-oscillation. Within spin Hall nano-oscillator (SHNO) devices, charge current is first converted into a pure spin current, by means of the spin Hall effect (SHE),[39,49,50,52] which subsequently exerts STT upon the active magnetic layer. Decoupling of spin and charge currents provides additional freedom in device design, in the choice of the magnetic materials used[89–92] (including electrical insulators[93]) and the precessional modes excited.[94] If the charge current flows parallel to the plane, without a top contact obscuring the active region, then optical techniques can probe the magnetisation dynamics

directly.[95,96] However as the structure is typically designed to concentrate electrical current in a finite region, by careful design of either electrical contacts or shape of the conductive layer,[96,97] it is expected that the spatial current distribution is highly non-uniform. Furthermore, thermal effects (such as Joule heating) may modify both the current distribution and the torques.[98–100] Knowledge of the Oersted torque and STT is critical for understanding the conditions under which auto-oscillations may be excited, or locked to a reference signal, and until now it has not been possible to probe their spatial distribution directly.

STT-ferromagnetic resonance (STT-FMR) is widely used to characterise spintronic devices. Radio frequency (RF) current is injected to excite the magnetisation, and mixes with the oscillatory MR response to generate a DC mixing voltage V_{mix}, which is recorded as the applied magnetic field or the frequency of the current is varied. Analysis of the resonance field, or frequency, and linewidth allows the torques acting upon the magnetisation to be determined.[61–63,65–67,101,102] However, V_{mix} vanishes for certain magnetic field configurations due to the symmetry of the MR mechanism, and represents a spatial average of magnetisation dynamics that may in fact be highly inhomogeneous.

In this chapter, time resolved scanning Kerr microscopy (TRSKM) is used to determine the torques generated by an RF current injected into an SHNO. The SHNO is formed on an extended magnetic disk, with the intention of concentrating the current and STT within a small central region. The spatial variation of both the STT and Oersted torques was mapped and found to diverge strongly from that expected for the DC current distribution, demonstrating that the reactance of the device geometry strongly modifies the RF current distribution.

4.2 Methodology

The SHNO devices shown in Figure 4.1 were fabricated on sapphire substrates by a combination of sputtering and electron-beam lithography.[90] Triangular Au (with

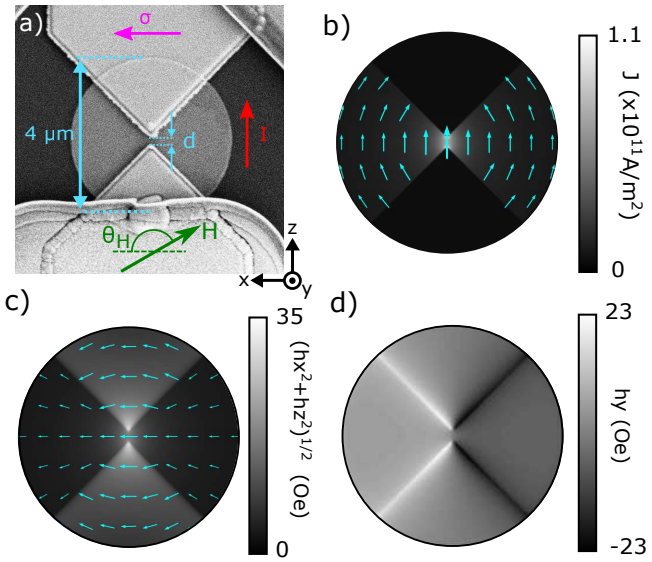

Figure 4.1: (a) SEM image of an SHNO showing electrode separation d, directions of the DC charge current I_{DC}, average polarization $\hat{\sigma}$ of the spin current injected into the Py layer, and field $\boldsymbol{H}$ orientated at angle θ_H relative to the x axis. COMSOL simulations for I_{DC} = 4 mA and d= 200 nm are shown for (b) current density $\boldsymbol{J}$ within the Pt layer, (c) in-plane Oersted field within the Py layer that has magnitude $\sqrt{h_x^2 + h_z^2}$, and (d), out of plane Oersted field h_y within the Py layer. The arrows and grayscale indicate the direction and normalized magnitude respectively.

a thicknesss of 150 nm) nano-contacts (NCs) with a tip separation of d = 140 - 240 nm were defined on a 4 μm diameter Py(5 nm)/Pt(6 nm) bi-layer disk. DC current I_{DC} from the gold NCs is concentrated within a small region of the Pt layer between the tips, and generates a spin current, by means of the SHE, that flows into the Py layer beneath. The injected spin polarization lies parallel to the +ve x direction along a horizontal line through the middle of the disk,[103] and exerts a STT on the Py magnetisation. The charge current also generates an Oersted field with both in and out of plane components. The distributions of the DC electric current and Oersted field plotted in figure 4.1 were calculated using COMSOL.[82] These calculations demonstrated that 80% of the current is expected to flow through the Pt, due to its higher conductivity. The STT amplitude is expected to have similar spatial distribution to the charge current within the Pt, while the Oersted field has a more complex structure that depends upon the current distribution in both the Pt and Au layers.

Conventional STT-FMR measurements were made by applying audio frequency modulation to an RF current I_{RF} injected through the capacitative arm of a bias-tee, while V_{mix} was measured through the inductive arm using a lock-in amplifier. The out-of-plane component of the dynamic magnetisation was also detected directly by means of TRSKM that has been described in detail in section 3.5.2.

Both the dynamic magnetisation and V_{mix} can be calculated in the macrospin limit. Section 3.2 contains a complete derivation, however the equations relevant to the interpretation of results are presented here. The equation of motion for the magnetisation of a thin film driven by an external field and STT is

$$\frac{d\hat{\boldsymbol{m}}}{dt} = -|\gamma|(\hat{\boldsymbol{m}} \times \boldsymbol{H}_{eff}) + \alpha\hat{\boldsymbol{m}} \times \frac{d\hat{\boldsymbol{m}}}{dt} - |\gamma|A\hat{\boldsymbol{m}} \times (\hat{\boldsymbol{m}} \times \hat{\boldsymbol{\sigma}}) + |\gamma|B(\hat{\boldsymbol{m}} \times \hat{\boldsymbol{\sigma}}), \quad (4.1)$$

where $\hat{\boldsymbol{m}}$ is the normalized magnetisation vector, γ is the gyromagnetic ratio, α is the Gilbert damping constant, $\hat{\boldsymbol{\sigma}}$ is the injected spin polarisation, and A and B are the amplitudes of the "anti-damping" and the "field-like" STT respectively. Given that the Py magnetisation lies within the sample plane, the anti-damping STT will act in-plane and field-like STT will act out of plane. A large anti-damping torque is expected due to the SHE. However, since the Py layer is relatively thick and the current is shunted through the Pt layer, negligible torque is expected due to the Rashba effect. $\boldsymbol{H}_{eff}$ is the total effective field acting upon the magnetisation, which may be written as $\boldsymbol{H}_{ext} + H_d(\hat{\boldsymbol{y}} \cdot \hat{\boldsymbol{m}})\hat{\boldsymbol{y}} + \boldsymbol{h}$, where $\boldsymbol{H}_{ext}$ is the static applied field, H_d is the out of plane demagnetising field, and $\boldsymbol{h}$ is the local Oersted field generated by the RF current. Other anisotropy fields are expected to be small and so have been neglected.

Equation (4.1) can be linearised to describe small amplitude precession, with the out of plane magnetisation component written as $m_y(\varphi) = Re(ae^{i\varphi})$ where φ represents the phase of the RF current and a is the complex amplitude. V_{mix} and the real and imaginary parts of a have the forms

$$V_{mix} = I_{RF}\Delta R sin\theta_H cos\theta_H \frac{|\gamma'|^2 H_\perp (f_0^2 - f^2)(H_{ext} + H_d) + |\gamma'| f^2 \Delta(\alpha H_\perp + H_{||})}{(f_0^2 - f^2)^2 + f^2\Delta^2}, \tag{4.2}$$

$$Re(a) = \frac{-|\gamma'|^2 H_{ext} H_{||}(f_0^2 - f^2) + f^2\Delta|\gamma'|(H_\perp - \alpha H_{||})}{(f_0^2 - f^2)^2 + f^2\Delta^2}, \tag{4.3}$$

$$Im(a) = \frac{f|\gamma'|(H_\perp - \alpha H_{||})(f_0^2 - f^2) + f\Delta|\gamma'|^2 H_{ext} H_{||}}{(f_0^2 - f^2)^2 + f^2\Delta^2}, \tag{4.4}$$

where

$$H_\perp = (sin\theta_H h_x + Bsin\theta_H)\,, H_{||} = \left(\frac{sin\theta_H}{|sin\theta_H|} h_y - Asin\theta_H\right), \tag{4.5}$$

$\gamma' = \gamma/2\pi$, f and I_{RF} are the frequency and amplitude of the RF current, θ_H is the angle between $\hat{\boldsymbol{m}}$ and $\hat{\boldsymbol{\sigma}}$, $H_\perp$ and $H_{||}$ represent effective fields, where the subscripts indicate the direction in which the associated torque acts, and A and B are defined in equation (4.1). Finally, the linewidth $\Delta = |\gamma'|\alpha(2H_{ext} + H_d)$, and the FMR frequency $f_0 = |\gamma'|\sqrt{H_{ext}[H_{ext} + H_d]}$. ΔR = 0.03 Ω[104] is the change in electrical resistance when the magnetisation is rotated from orthogonal to parallel to the current.

The above expressions yield m_y at different positions within the SHNO when the observed dynamical magnetisation is a response to local torques. This is a reasonable assumption when spin waves excited due to spatially varying STT and Oersted torques are similar in frequency.

4.3 Results

The stroboscopic nature of TRSKM requires that measurements are made at an RF frequency that is a multiple of the laser repetition rate as H_{ext} and hence f_0 are varied. From equations (4.3) and (4.4), the expressions for $Re(a)$ and $Im(a)$

are seen to contain a minimum in the denominator at the resonance field, and terms in the numerator that are either slowly varying or antisymmetric (due to the factor $f_0^2 - f^2$) about the resonance field. Hence both expressions consist of parts that are symmetric and antisymmetric about the resonance field. The microwave phase φ may be chosen in the experiment, so that m_y is a weighted sum of $Re(a)$ and $Im(a)$, and so m_y also appears as a sum of symmetric and antisymmetric terms. TRSKM measures the polar Kerr rotation that may be written as $QM\hat{m}_y$ where the constant Q is of order 0.1 mdeg cm^3 emu^{-1}. If the value of Q is known then, by recording the dependence of m_y upon H_{ext} for a number of values of φ, and fitting m_y to equations (4.3), (4.4) and (4.5), the values A and B can be determined at each position within the sample.

Conventional STT-FMR was first performed to obtain V_{mix}, as shown in figure 4.2a. The optical probe was then positioned between the NC tips and the polar Kerr signal recorded at three values of RF phase as a function of field, as shown in figure 4.2b. Both optical and electrical resonance curves are a superposition of components that are either symmetric or antisymmetric about the resonance field. The V_{mix} data, which does not depend upon φ, was fitted to equations (4.2) and (4.5), yielding values of $H_\perp = -6.1 \pm 0.8$ Oe and $H_{||} = 29.7 \pm 3$ Oe, while values of $|\gamma'| = 2.94$ MHz/Oe, $\alpha = 0.04$ and $H_D = 8000$ Oe were found to best describe both the V_{mix} and optical data within the present study. The relatively large value of α has been attributed to spin pumping effects.[98] Since the average out-of-plane Oersted field h_y is small due to the symmetry of the NCs, the large value of $H_{||}$ results from the anti-damping torque. From equation (4.5), if $\theta_H = 150°$, h_x has value of ~12.1 Oe, which has similar order of magnitude to the 10.2 Oe calculated by COMSOL at the centre of the disk for a DC current.

Due to the symmetry of the device, one may reasonably assume that the ratio $H_\perp/H_{||}$ determined from the optical measurements in figure 4.2b should be the same as that determined by fitting V_{mix}. Fixing this ratio and fitting the optical resonance curves then yields values for φ, that have been used to label each curve.

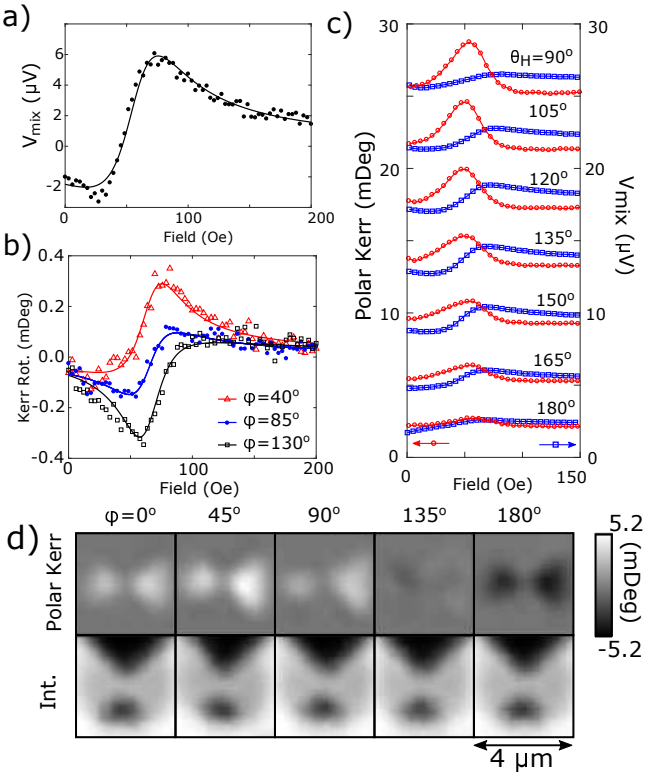

Figure 4.2: (a) Dependence of mixing voltage V_{mix} upon field H_{ext} applied at $\theta_H = 150°$. The continuous curve is fit to equation 4.2. (b) Polar Kerr rotation curves recorded with the optical spot between the tips of the NC for three values of the phase φ. (c) Polar Kerr (closed circles) and V_{mix} (open squares) resonance curves recorded with the optical probe 1μm to the right of centre, for different values of θ_H. (d) Polar Kerr rotation and intensity images for $\theta_H = 90°$ and $H_{ext} = 75$ Oe for φ values in the range 0 to $180°$. The current had frequency of 2 GHz and amplitude of 2.8, 1.3, 3.2 and 4.0 mA in (a), (b), (c) and (d) respectively. The NC separation $d = 240$ nm in (a) and (b), and 140 nm in (c) and (d)

The three phase values were found to be offset set by the same amount from the values set on the microwave synthesizer, shown in table 4.1. The consistency in offset found justifies the assumed value of $H_\perp/H_{||}$. An average value for the offset of $-50.3°$ was then assumed in all subsequent fitting. The fitting also yields an estimate of Q, but this is less reliable because the areas sampled by the electrical and optical measurements are different, as will be discussed further.

The dependence of optical and electrical signal strength upon θ_H is shown in Figure 4.2c. Maximum optical signal amplitude is observed for $\theta_H = 90°$, due to the $sin(\theta_H)$ factor in equation (4.5). In contrast V_{mix} vanishes for $\theta_H = 90°$

φ_{RF}	Fitted φ	$\Delta\varphi = \varphi - \varphi_{RF}$
$90°$	$37.7°$	$-52.5°$
$135°$	$87.9°$	$-47.1°$
$180°$	$128.6°$	$-51.4°$

Table 4.1: The value of the phase of the current at the sample, φ, obtained from the fits in Figure 4.2, is tabulated with the nominal phase at the synthesizer φ_{RF}, and the difference of the two values $\Delta\varphi$.

and $180°$, and is insensitive to the dynamics when $\theta_H = 90°$. Finally, polar Kerr images are plotted in figure 4.2d for different values of φ. Due to the symmetry of the current distribution about a vertical line though the centre of the device, A, h_x and hence $H_\perp$ are expected to be symmetric about this centre line. On the other hand h_y is antisymmetric so that $H_{||}$ has mixed symmetry. If terms in α are neglected in equations (4.3) and (4.4), then at resonance, when $f = f_0$, $Re(a)$ is symmetric about the centre line, while $Im(a)$ has mixed symmetry. Therefore, the most symmetric image is expected to occur for $\varphi = 0°$. The most striking feature of the images is the minimum between the NC tips, which is unexpected from the DC current calculations in Figure 4.1.

Preliminary investigations of the spatial distribution of torques were carried out by considering the effective fields present on opposite sides of the NCs. Figure 4.3 shows the field dependence of the polar Kerr rotation, obtained from positions 1 μm left and right of the NCs. Each resonance curve was fitted with its calculated value of phase, with the extracted effective fields plotted in table 4.2. Mechanical drift, experimental noise, and phase noise represent sources of experimental error. The standard deviation across each data set represents the uncertainty arising from this. The root mean square error provides a measure of the quality of fit. Despite some curves exhibiting a poor fit, the extracted values for $H_\perp$ are reasonably consistent across all phases and on both sides of the disk (within experimental error), justifying the method for extracting the phase offset. In contrast $H_{||}$ is significantly different between the two sides of the disk, which will be explored

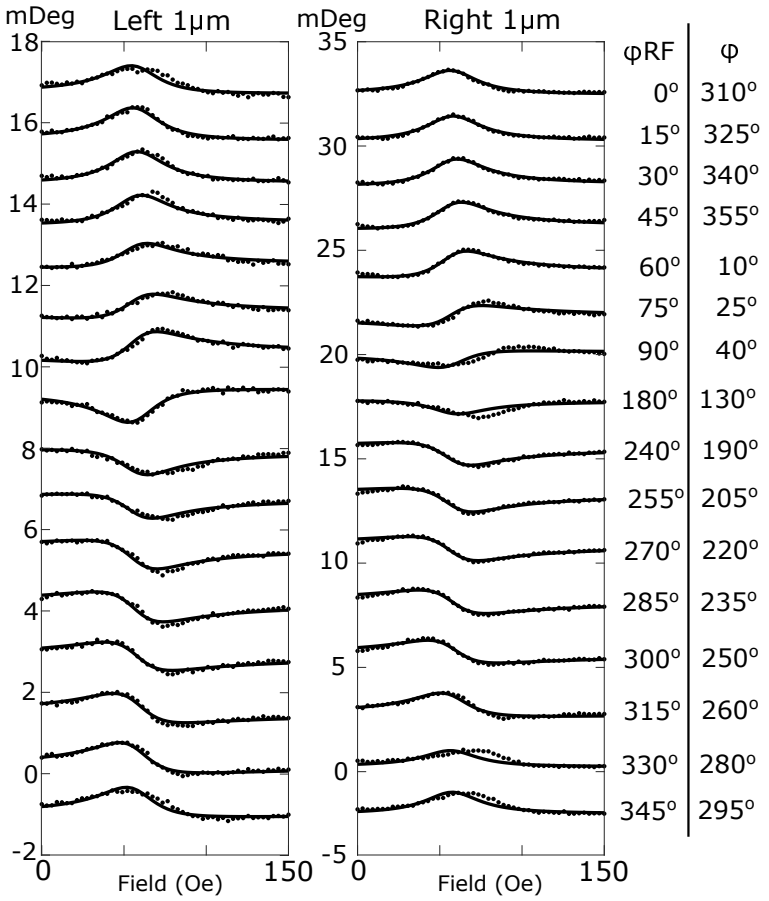

Figure 4.3: Optical resonance curves acquired with the optical spot positioned 1 μm to either side of the NCs. The phase set on the microwave synthesizer φ_{RF}, and the phase of the current at the sample φ are shown next to the curves. The external field was applied in the vertical direction ($\theta_H = 90°$), while the current had frequency of 2 GHz and amplitude of 1.3 mA. The curves have been offset in the vertical direction for clarity.

further.

In order to probe the spatial distribution of torques, polar Kerr resonance curves were measured at different points on a horizontal line through the middle of the disk, for values of $\varphi = 40°$, 85° and 130°. The extracted values of effective fields $H_\perp$ and $H_{||}$ are plotted as a function of position in figure 4.4a. The field values obtained for the three values of φ are in good agreement confirming that the absolute phase has been determined correctly.

Param. (Oe)	Mean $H_{\perp}$	St Dev $H_{\perp}$	Mean $H_{||}$	St Dev $H_{||}$	Mean RMSE
Left	0.8935	0.0997	-5.3400	0.8643	5.1×10^{-5}
Right	0.9141	0.4807	-13.4049	1.7338	9.3×10^{-5}

Table 4.2: Mean and standard deviation of the effective field parameters extracted from the fits shown in Figure 4.3. Root Mean Square Error (RMSE) is defined as $\sqrt{\frac{\Sigma_{i=1}^{n}(\bar{X}_i - X_i)^2}{n}}$, where $X_i$and $\bar{X}_i$ are the fitted quantity and its mean value, and n is the number of measured values.

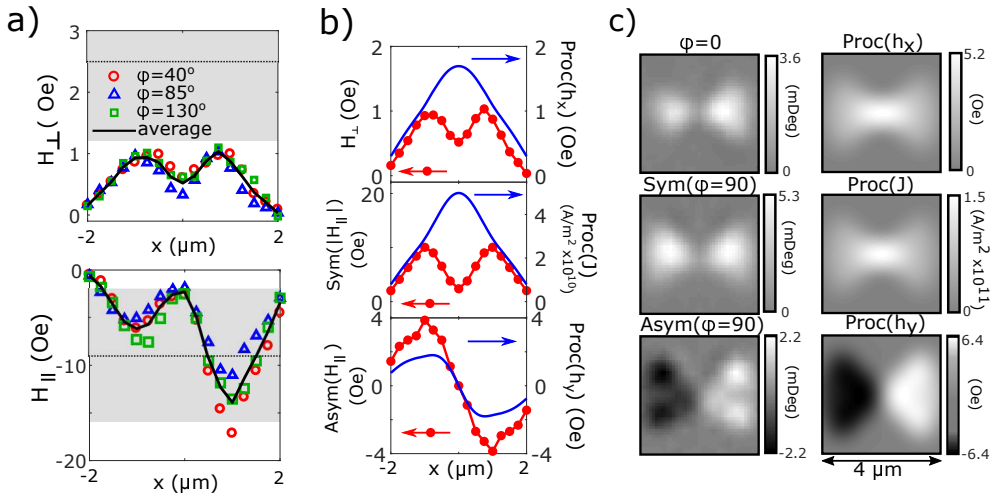

Figure 4.4: a) Spatial variation of $H_{\perp}$ and $H_{||}$ along the horizontal line passing through the middle of the disk. Values obtained from electrical STT-FMR are shown by the dashed line with the error indicated by the gray shading. The injected RF current had frequency f = 2 GHz and amplitude I_{RF} = 1.3 mA, while the static field was applied at θ_H = 90°. b) $H_{\perp}$ and the antisymmetric/symmetric parts of $H_{||}$ are plotted together with the current and Oersted field from Figure 4.1. c) Polar Kerr image acquired for $\varphi = 0°$, I_{RF} = 4 mA and H_{ext} = 75 Oe is presented next to the calculated distribution of h_x. Symmetric and antisymmetric parts of the polar Kerr data acquired at $\varphi = 90°$, are presented next to the vertical component of the current density J_z and the out of plane Oersted field h_y. The calculated images were convolved with a Gaussian profile of 870 nm half maximum diameter. The NC separation d was 240 nm for a and b, and 140 nm for c.

4.4 Discussion

Since negligible field-like STT is expected, $H_{\perp}$ should be proportional to h_x and hence spatially symmetric. However, $H_{||}$ should contain both symmetric and antisymmetric components, (denoted as $Sym(|H_{||}|)$ and $Asym(H_{||})$) due to the anti-damping STT and h_y respectively. These components can be separated by calculating the mirror image (reflection about $x = 0$) of the $H_{||}$ data, calculating the sum and difference of the original data with its mirror image, and then dividing both by a factor of two. Both components are plotted in figure 4.4(b), together with convolutions of the Oersted field and current distributions of Figure 4.1 with a Gaussian function of 870 nm half maximum width (denoted Proc($h_{x,y}$)), to account for the finite size of the focused optical spot. In extracting field quantities from the experimental data, a value of Q = 0.3 mdeg cm^3 emu^{-1} was assumed so that the Oersted fields towards the edge of the disk were in agreement with those from Figure 4.1. However, the experimental $H_{\perp}$ and $Sym(|H_{||}|)$ curves are seen to exhibit a minimum at $x = 0$ μm, in strong disagreement with the calculated curves.

As explained above, for $\varphi = 0°$ and $90°$, time resolved images acquired at resonance reveal the spatial variation of $H_{\perp}$ and $H_{||}$ respectively. A similar procedure to that applied to the line scan in figure 4.4(b) was used to extract the symmetric and antisymmetric parts of the image acquired at $\varphi = 90°$. The resulting images of $H_{\perp}$, $Sym(|H_{||}|)$ and $Asym(H_{||})$ are plotted next to calculated images of h_x, J, and h_y in Figure 4.4c. Each calculated distribution has been convolved with a 2D Gaussian function of 870 nm half maximum diameter. The form of the $Asym(H_{||})$ and h_y images are in reasonable agreement. However the h_x and J images possess a maximum at the centre of the disk, whereas the $H_{\perp}$ and $Sym(|H_{||}|)$ images exhibit a minimum. The convolution with the spot profile takes into account the fact that the NCs partly obscure the underlying Py/Pt bilayer, so that the minimum corresponds to a reduction of the anti-damping STT and the torque due to the in-plane Oersted field.

The observed minimum initially seems at odds with observations of a self-localised bullet mode at the centre of this[104,105] and similar devices,[95] and is due to the spatial distribution of I_{RF} in the present study being quite different to that of I_{DC} used to excite the bullet. It is well established that the distributed reactance of a coplanar waveguide (CPW) gives rise to current crowding at the edges of the signal line.[106–108] The distribution of I_{RF} within the SHNO results from competition between the confining effect of the NCs and current spreading within the larger device structure that has the form of a short CPW. SHNO's have previously demonstrated a reduced frequency range for synchronising auto-oscillating spin waves to an applied RF current.[99] This observation may be explained by current spreading, which leads to a reduction of the torque at the centre of the device.

4.5 Summary

In summary, it has been shown that TRSKM can be used to probe the local FMR driven by a combination of STT and Oersted field torques, and comparison has been made with a simple theory. By directly probing the local magnetisation, this technique can be applied to magnetic materials or experimental configurations that exhibit a weak MR response. Furthermore the phase and spatial symmetry of the different torques allows them to be separated and mapped. The reactance of the device leads to spreading of the RF current so that the spatial distribution of the associated torques is significantly different to that generated by a DC current. Despite the focusing of current by the geometry, the torques due to the RF current exhibit a minimum at the centre of the device. This leads to an increased difficulty in the synchronisation of non-linear spin waves excited by DC current. TRSKM observations of spin waves synchronised in this way are the subject of chapter 5. The possibility of current spreading in spintronics has not been considered previously, but is of vital importance for the development of STOs as microwave oscillators.

CHAPTER 5

Time resolved imaging of the non-linear bullet mode within an injection-locked spin Hall nano-oscillator

5.1 Introduction

The work here builds upon that in chapter 4, and as a result, much of the background and motivation remains the same. Instead, this chapter will focus on a novel form of spin wave, dubbed the spin wave bullet. Section 2.5.2 outlined the established linear theories for spin waves. This chapter will discuss the spin wave 'bullet', a spin wave described by a non-linear theory provided by Slavin and Tiberkvich.[31]

The bullet possesses a number of attributes that highlight it for technological applications, distinct from other spin wave systems. As it represents the lowest threshold of spin wave excitation, great potential exists for low power oscillators. The bullet owes its name to parallels in optics, whereby light pulses which propa-

gate while preserving their spatial profile are given this name.[109] This soliton-like behaviour is of interest in magnon-based computing, where bullets could serve as information carriers.[6]

Experimentally, the bullet mode has been observed in numerous systems. Brillouin light scattering (BLS) enables the measurement of spin waves from the inelastic scattering of light,[73] this spectroscopic technique has shown the bullet mode to have a highly tunable frequency and remain highly localized to the active region under DC current.[95] Magneto-transport measurements under cryogenic temperatures have demonstrated that the system is highly sensitive to temperature. While a reduction in thermal fluctuations improves the power, a second higher frequency mode was produced.[98] Micromagnetic simulations have taken steps towards explaining this additional mode, whereby a minimum in the internal field enables a field-localized mode to coexist.[100,110] Additional BLS measurements have been carried out on devices with different materials as magnetic layers,[89–93] highlighting contrasting values for linewidth and output power across different materials. While not studied in this thesis, the bullet mode has also been observed in nano-constriction oscillators,[97,111] whereby an absence of material from a Pt/Py bilayer concentrates charge and spin currents. This concept can be expanded by including multiple constrictions in a sample, allowing for multiple bullets to be excited and synchronized.[94,112,113] While oscillations in these devices can be observed for lower currents, they are also more vulnerable to damage from capacitive discharge. Furthermore, as the constriction extends to the magnetic layer, the mode is pinned in place by the device shape.

The generation of magnetic auto-oscillations requires a critical spin current density to be exceeded. While many modes can be excited, those with a high group velocity escape the active region and are subsequently damped. However, once the critical current is obtained, damping within the active region is compensated for and a spin wave bullet forms, distinct from incoherent thermal magneti-

sation fluctuations. While the spectral characteristics of the dynamics have been explored, the time-evolution of the magnetisation has yet to be measured directly.

In the present work, time resolved scanning Kerr microscopy (TRSKM)[76,114] is used to observe the time dependent magnetisation within a SHNO that has been phase locked to an injected radio frequency (RF) current I_{RF}. Formation of the non-linear bullet mode is observed when the injected DC current I_{DC} exceeds a threshold value. Comparison with micromagnetic simulations shows that the diameter of the bullet is small compared to that of the optical spot. Nevertheless the apparent diameter of the bullet mode is observed to increase with I_{DC}, suggesting increased translational motion of the bullet.

5.2 Experimental method

SHNOs were fabricated by a combination of sputter deposition and electron-beam lithography. A 4μm Py(5 nm)/Pt(6 nm) bi-layer disk was first defined, before two triangular Au(150 nm) nanocontacts (NCs), with a tip separation of 200 nm, were overlaid as shown in figure 5.1a. The device is designed to concentrate electrical current within the Pt layer at the NC tips. Here the charge current is used to generate a spin current, by means of the SHE, that propagates normal to the plane of the device into the Py layer. Once the STT compensates the damping, a self-localized non-linear mode is formed, that has been described as a spin wave bullet. While other modes can be supported within the disk (reference [110] demonstrates propagating waves when the Py is magnetised normal to the plane), the bullet mode is of particular interest due to its narrow linewidth and tuneable frequency.

Initial microwave electrical measurements employed the magneto-transport equipment as described in section 3.3 to exploit the magnetoresistive response of the Py layer. A ground-signal-ground electrical probe was used to make electrical contact to a selected device and connect it to a bias-tee. The inductive and

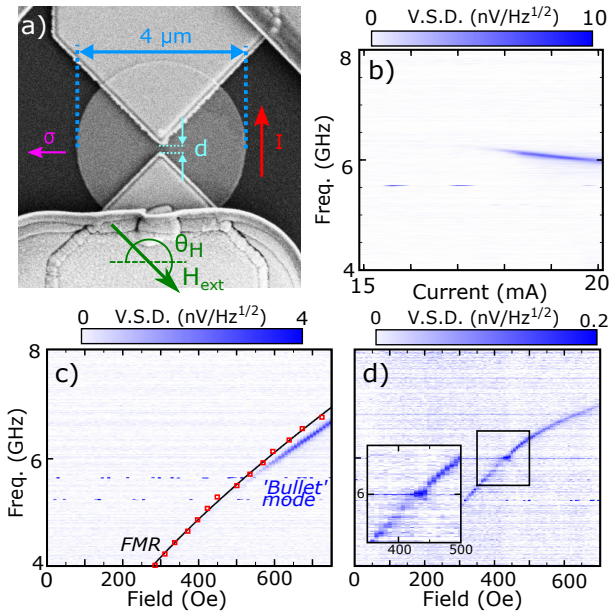

Figure 5.1: a) SEM image of a typical SHNO, where I is the injected current, σ the corresponding spin polarization, d the NC separation, and H the magnetic field applied at angle θ_H. b) Voltage Spectral Density (VSD) of microwave emission from a SHNO with d = 240 nm at fixed magnetic field H = 650 Oe and θ_H = 210° for different values of I_{DC}. c) Emission excited from a SHNO with d = 180 nm for I_{DC} = 18 mA, with magnetic field H orientated at θ_H =150°. Red squares show resonance fields from STT-FMR, solid black curve shows the fit to the Kittel equation, acquired from the same device. d) Emission for a device with d = 240 nm when I_{DC} = 18.5 mA and I_{RF} has amplitude of 3.5 mA and frequency of 12 GHz. Enhancement of locking region shown as inset.

capacitative arms were used to supply I_{DC} and I_{RF} respectively, while the RF signal returned from the device was directed into a spectrum analyzer via a circulator and +24 dB pre-amplifier. TRSKM measurements utilized the experiment described in section 3.5.2. For the dynamics to be observed in a stroboscopic fashion, they must be synchronised, via the injected I_{RF}, to an exact multiple of the 80 MHz laser repetition rate. The phase of I_{RF} can then be adjusted relative to the laser pulses so that the time evolution of the magnetisation dynamics can be observed. Measurements were performed with phase modulation of I_{RF} to enhance the signal to noise ratio. The laser pulses had 800 nm wavelength, and were focused to a spot of ∼870 nm FWHM diameter by a microscope objective with 10.1 mm working distance and 0.55 numerical aperture.[115]

5.3 Results

5.3.1 Electrical Characterization

Microwave electrical measurements were performed to identify the bullet mode and confirm locking to I_{RF}. Figure 5.1b shows the emission from a SHNO for fixed field and increasing I_{DC}. The onset of emission is observed at I_{DC} ~18 mA. The frequency red-shifts with increasing I_{DC} and emission is still present at I_{DC} = 20 mA. Figure 5.1c shows the field and frequency dependence of both the Ferromagnetic Resonance (FMR), determined from separate STT-FMR measurements (consistent with previous work[66,98]), and the microwave emission for the same device. For a given frequency, microwave emission is observed at a field close to but greater than that of the FMR mode. The dependence of the frequency upon H and I_{DC} is consistent with previous observations of the bullet mode.[100]

These measurements can be used to demonstrate the symmetry of the SHE. Figure 5.2 shows that in order to support the bullet mode, an angle of 60°-120° between the current and external field is required. If the current is reversed the polarisation of injected spin is likewise reversed, and hence the external field must also be reversed if a bullet mode is to be supported. It should be noted that the AMR vanishes for field angles close to 90° (and 0°), suppressing the electrical emission (despite the fact the bullet is still excited). Furthermore, due to the SHE, switching the Pt and Py layers within the stack reverses this effect, in such a device a +ve current would require θ_H ~0° for operation.

Stroboscopic TRSKM measurements require the bullet mode to be synchronised to I_{RF}. Figure 5.1d demonstrates that a bullet mode of 6 GHz frequency can be locked to an I_{RF} of 12 GHz frequency, a process known as harmonic injection locking. As H is varied, the frequency of emission approaches 6 GHz and is 'pulled' towards the locking regime. Within this region an increase in output power and reduction in linewidth is observed. Outside this regime an intermodulation mode can be seen, decreasing in frequency with increasing field. A large I_{RF} of

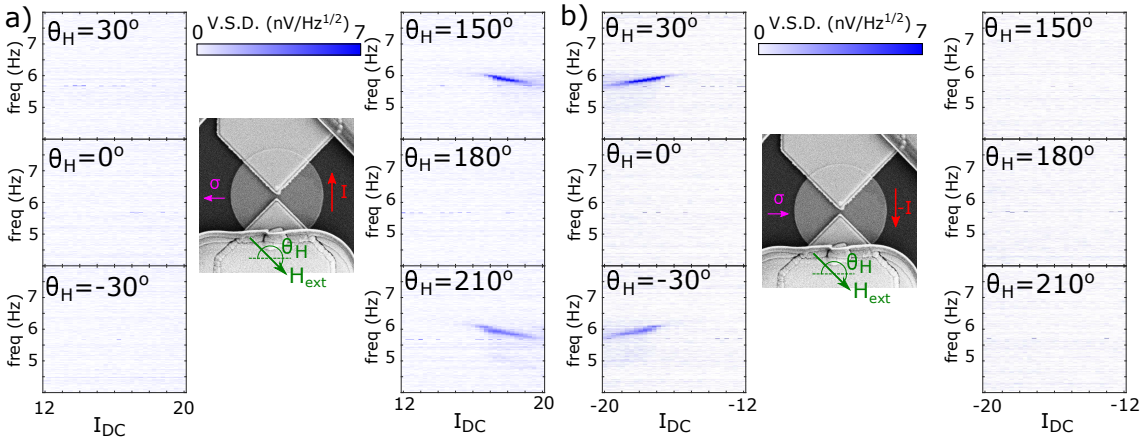

Figure 5.2: Magneto-transport measurements illustrating the symmetry of the bullet mode, emission shown for a) positive I_{DC} and b) negative I_{DC}. Excitation of the bullet mode requires the external field to be applied close to 90° to the direction of current. In addition, the vanishing AMR and angles θ_H ∼0° and 180° suppresses the RF emission, hence precession is only observed for intermediate field angles.

∼ 3.5 mA amplitude was required to achieve even a narrow locking range, which has been attributed to thermal noise enhanced by the spin current.[99]

Chapter 4 employed optically-detected STT-FMR to demonstrate that an FMR mode is driven in the extended disk, and that reactance of the device geometry causes spatial spreading of I_{RF} laterally through the Pt layer. To reduce the amplitude of these dynamics it is necessary to minimize the amplitude of I_{RF}, which can be done by locking at the fundamental frequency of 6 GHz. Figure 5.3 shows the device emission from fundamental injection locking.

A residual component of the injected 6 GHz signal is detected due to imperfect impedance matching and the finite rejection efficiency of the microwave circulator used. While the background recorded for zero magnetic field has been subtracted from each spectrum in figure 5.3, increased noise is observed at 6 GHz that obscures the emission of the locked oscillator. Nevertheless, locking can be identified from the frequency pulling as the frequency of emission approaches 6 GHz. The red line in figure 5.3 indicates the frequency of emission for I_{RF} = 0. The emission clearly deviates from the red line when RF current is injected and the width of the locking region increases with the I_{RF} value.

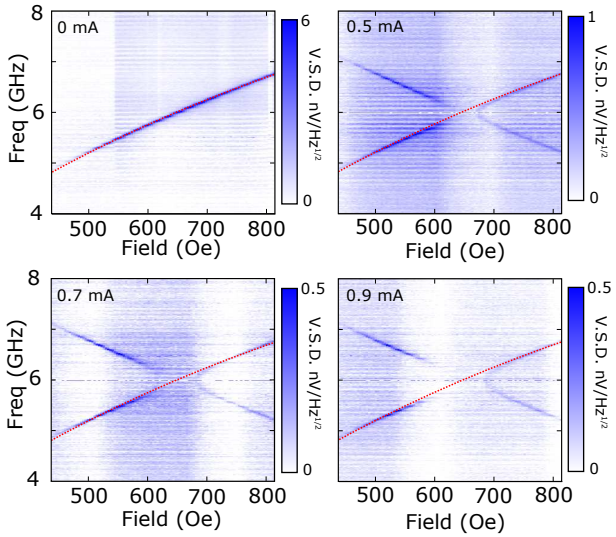

Figure 5.3: Microwave emission observed when Injection locking at 6 GHz for different I_{RF} values (shown at top left of each plot). The red dashed line shows the maximum emission for I_{RF} = 0 mA.

5.3.2 TRSKM Measurements of the full magnetic response

Figure 5.4a shows TRSKM images acquired with the bullet mode locked to I_{RF}, and when I_{RF} is still present but I_{DC} = 0 mA. In the latter case, I_{RF} drives the FMR with H detuned from the line centre. The addition of I_{DC} leads to additional dynamics in all three magnetic channels. In the polar magnetisation channel, localized precession is observed between the NC tips, with a different phase to the dynamics in the extended disk. By subtracting the images acquired with and without I_{DC}, the dynamic response due to I_{DC} may be estimated, shown in figure 5.4b. The subtracted images for the two in-plane (horizontal and vertical) channels each exhibit a spatially antisymmetric structure centred on the peak observed in the polar contrast, but occupying a somewhat larger area of $\sim 2\mu m$ diameter. The subtraction yields negligible residual contrast in the extended region of the disk, confirming that the bullet mode is tightly confined at the centre of the disk.

Further measurements at different time delays are shown in figure 5.5, demonstrating that the contrast in the magnetic channels oscillates with I_{RF}. However the contrast in the three channels is observed to oscillate with the same relative phase, which is not expected if the magnetisation undergoes a circular or elliptical

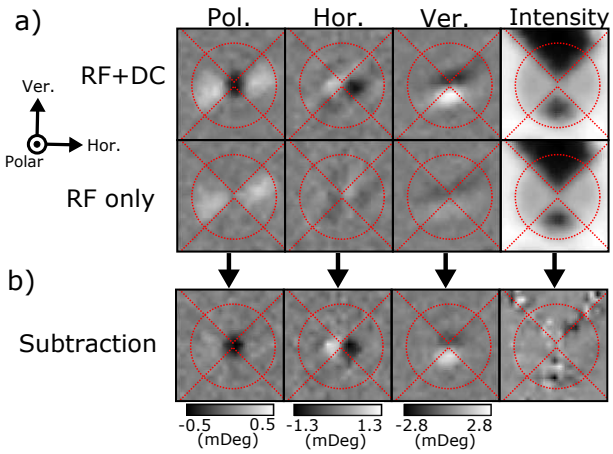

Figure 5.4: a) TRSKM images acquired from the polar (out of plane), horizontal, vertical and reflected intensity channels of the vector bridge detector for a SHNO with d = 200 nm, H = 650 Oe, $\theta_H = 210°$, and I_{RF} = 1.4 mA at 6 GHz frequency. I_{DC} = 16 mA and 0 mA in the upper and lower panels respectively. (b) The difference of the upper and lower images from (a) is shown, revealing contrast due to the presence of I_{DC} only. Each image shows a 5 μm square region.

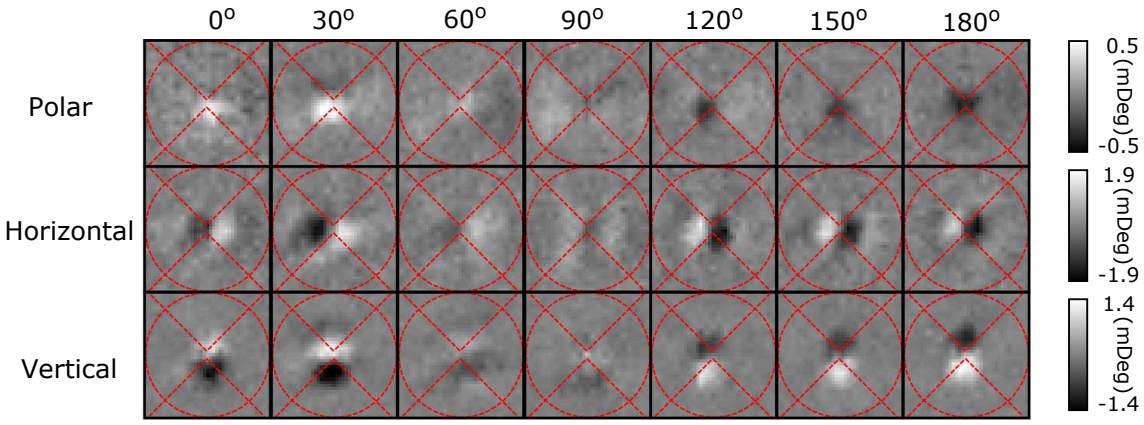

Figure 5.5: a) TRSKM images acquired for different values of the phase of the injected RF current for a SHNO device with tip separation d = 240 nm. In each case an image acquired at I_{DC} = 15 mA has been subtracted from an imaged acquired at I_{DC} = 18 mA. In each case I_{RF} = 0.8 mA, while a static field of H = 650 Oe was applied at an angle θ_H=210° as defined within the main text. Each image shows a 4 μm square field of view.

precession. Furthermore, since θ_H = 30°, the amplitude of the dynamic magnetisation detected in the TRSKM experiment is expected to be significantly greater in the vertical as compared to the horizontal direction, while in fact these two components were found to have comparable amplitude. To aid interpretation of the experimental data, micromagnetic simulations were performed, using the MuMax 3 package after the current distribution and associated Oersted field had been calculated in COMSOL.[81,82]

5.3.3 Micromagnetics

COMSOL simulations for the current distribution and Oersted field are plotted in figure 4.1 of chapter 4, while the simulations that follow use a higher amplitude current, the spatial distribution is identical.

The simulations shown here were carried out for a 4 um disk, using cubic cells of 5 nm size. The simulations assumed values of 0.02 for α the Gilbert damping parameter, 13 $\times$ 10^{-12} J/m for the exchange constant, 1.85555 $\times$ 10^{11} rad/Ts for the gyromagnetic ratio, and 650 $\times$ 10^3 A/m for the saturation magnetisation of the Py layer. The spin current density (in charge units) perpendicular to the plane (with polarization as shown in figure 5.1a was taken to be equal to the local charge current density within the Pt layer multiplied by a spin Hall angle of 0.08.

Simulations were performed for different values of I_{DC} with the values of the STT and Oersted field scaled appropriately. Once a critical value of I_{DC} was reached, unstable dynamics were excited, and persisted to the highest current values tested. In this case a cyclic process was observed. A bullet mode was excited at the centre of the disk, which then escaped the active region and was damped in the extended disk. Figure 5.6 demonstrates this process. After the bullet has been damped, another is later excited in the same region.

In order to pin the mode it was necessary to include a discontinuity in the saturation magnetisation. This could be done by emulating magnetic grains, de-

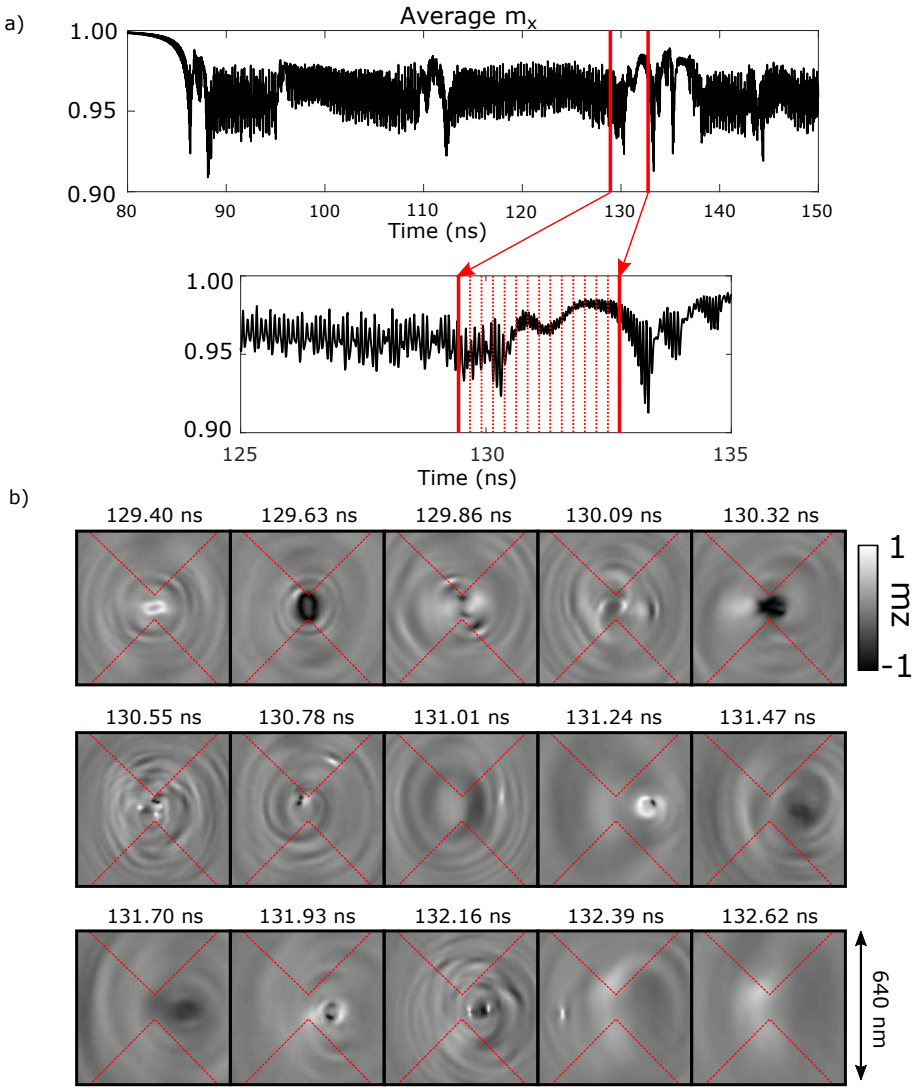

Figure 5.6: a) Typical time trace from a simulation of the spatially averaged horizontal magnetisation component. Vertical red lines indicate periods of instability. b) Selected time resolved images of the out of plane magnetisation component from the period of instability shown in (a).

fined using the Voronoi tessellation algorithm,[81] whereby a grain with increased or decreased saturation magnetisation were found to pin the mode. However, a gradual reduction of the saturation magnetisation due to heating near the NC tips was deemed more likely. COMSOL simulations suggested a temperature rise of 20° for a 20 mA current, with the RF current possibly providing an additional contribution. Such calculations are very sensitive to the assumed thermal properties of the stack, the parameters of which are poorly known. The reduction of the magnetisation was therefore assumed to have a peak value of 5% at the centre of the disk, with a spatial distribution described by the function

$$f(r) = e^{\frac{-r^2}{2\sigma^2}} \tag{5.1}$$

where r is the distance from the centre of the disk, and $\sigma = 100$ nm.

With the Gaussian magnetisation profile, the bullet mode was successfully pinned within the active region of the device for I_{DC} = 20 to 22 mA, close to the measured values of 16-19 mA (note the difference in applied field magnitude in figures 4.1 and 5.7). However instead of a single mode, two modes were found to be excited in the simulation, at ∼6.5 GHz and ∼8.6 GHz as can be seen in figure 5.7. The amplitude and frequency of both of these modes were observed to depend on I_{DC} and the applied magnetic field.

The frequencies of the modes observed here are in agreement with those observed in previous studies.[98,100,110] Figure 5.8 shows spatial power maps for the two modes, demonstrating their different structure. The larger amplitude mode occupies an area of ∼100 nm diameter, consistent with previous observations, and is identified as the bullet mode. In contrast, the higher frequency mode occupies a larger region, surrounding that occupied by the bullet mode and has been described as a field localized mode. This mode exists within a local field minimum generated by the total Oersted field, and hence has a spatial character that is highly dependent on the orientation of the static magnetic field.

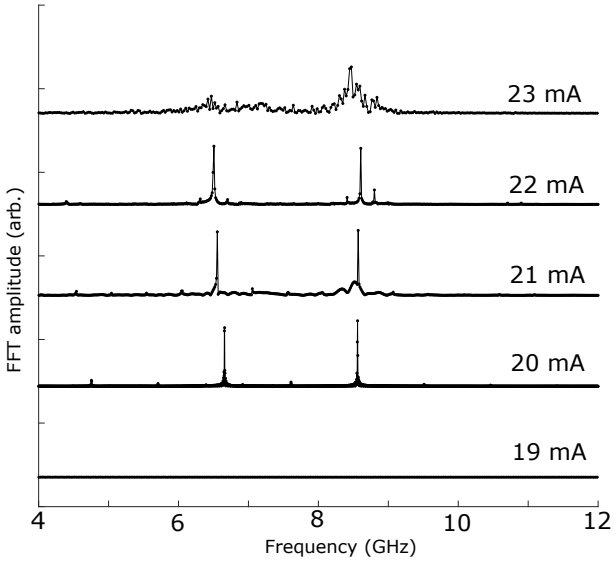

Figure 5.7: Power spectrum of the spatially averaged out of plane component of magnetisation for a SHNO with a field of 1 kOe applied θ_H=210°.

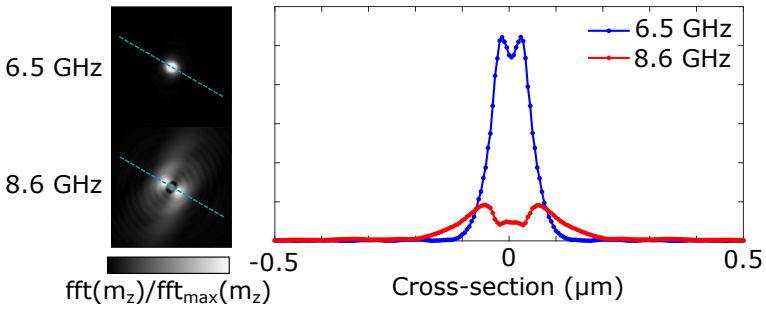

Figure 5.8: Spectral images of both bullet and field localized modes with cross-sections through the images (blue dashed lines).

Images of the simulated bullet mode are presented in figures 5.9 for the configuration in figure 5.4. While the bullet mode exhibits large angle precession, the images in figure 5.9a do not reproduce the spatially antisymmetric character observed in the measured horizontal and vertical components. The core of the bullet mode undergoes the largest angle of precession. Figure 5.9b shows the magnetisation trajectory for decreasing distance to the center of the bullet, divided into regions of interest, (i) outside the bullet and (ii) within the bullet's core. Outside the core region the magnetisation undergoes elliptical precession about an axis parallel to the applied field. At the edge of the core region, at x = -35 nm, the average magnetisation is close to zero with an in-plane precession angle

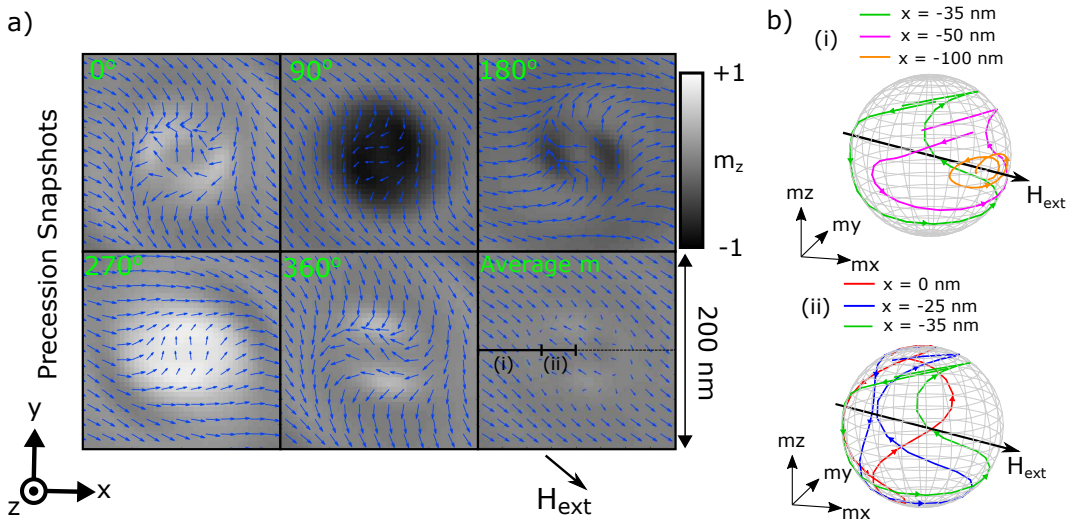

Figure 5.9: a) Simulated magnetisation profile at different phase values within the cycle of auto-oscillation. The arrows indicate the projection of the magnetisation within the plane, while the grayscale represents the out of plane component. The images show the bullet mode with $\sim$ 70 nm diameter at the centre of the device. Lower right panel contains the time-averaged and indicates two areas of interest, (i) the area immediately outside the bullet, and (ii) the bullet mode's core. b) Trajectories of the magnetisation for different points on the x axis as indicated in (a), arrows show direction of precession over 1 cycle of oscillation. Trace for x = -35 nm presented in both (i) and (ii) to aid comparison between precession inside and outside of the bullet.

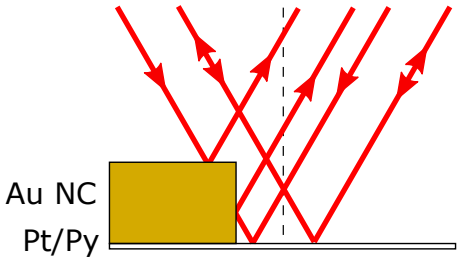

Figure 5.10: Schematic to illustrate the artefact that generates contrast in the horizontal and vertical channels. Arrows indicate the direction of propagation of rays.

of $\sim$270°. Within the core the precession amplitude increases further so that the magnetisation trajectory crosses over itself with the magnetisation effectively precessing about a direction anti-parallel to the applied field. The magnetisation precesses with the same phase at all positions within the disk. However it should be noted that the presence of the field-localized mode could not be suppressed, and hence the traces in figure 5.9b do not meet up. Simulations performed with an additional I_{RF} demonstrated slightly improved stability of the bullet, but otherwise the dynamics were of similar character.

The simulated magnetisation snapshots underwent additional processing for comparison with the experiment. As the TRSKM employs phase modulation and has a beam spot of size comparable to the dynamics, difference images were calculated from simulated images separated by 180° in phase and convolved with a 870 nm full width half maximum Gaussian profile. Again they did not reproduce the spatially antisymmetric contrast observed in the vertical and horizontal channels. Further tests were carried out with a reduced magnetic field, in order to identify if the contrast could be attributed to mechanical motion of the device, however these demonstrated that the antisymmetric contrast was observed only when the bullet mode was present.

Therefore it can be concluded that the in-plane contrast must be an artefact associated with the optical probe overlapping the edge of the 150 nm thick NCs, while in proximity to the bullet mode. Figure 5.10 provides a schematic representation of the likely mechanism. As the probe passes over the NCs the beam returning to the detector is partially obstructed. Crucially the symmetry between rays propagating in opposite directions within the cone is broken. The resulting difference in intensity of the two halves of the back-reflected beam, combined with a finite polar Kerr rotation due to the bullet mode, manifests as a signal similar to that due to the longitudinal MOKE from an in-plane component of magnetisation.[116] It follows from the NC geometry that a top-bottom antisymmetry is observed in the vertical channel and a left-right antisymmetry in the horizontal channel.

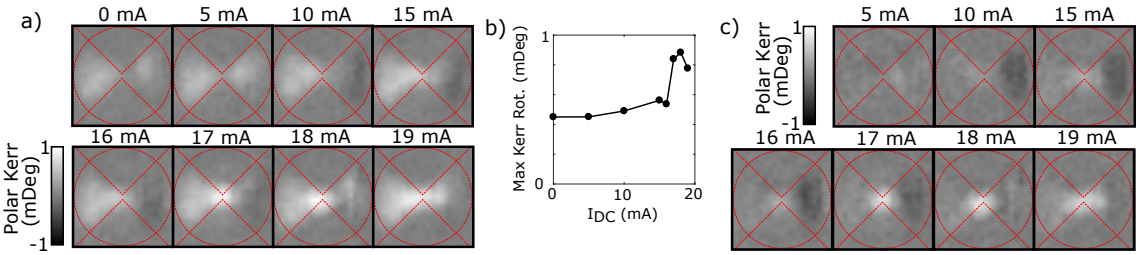

Figure 5.11: a) Polar TRSKM images acquired for different I_{DC} values with the phase of I_{RF} fixed. b) Maximum absolute values of polar Kerr rotation extracted from the images in (a). (c) TRSKM images from (a) after subtraction of the $I_{DC} =$ 0 mA image. All images were recorded from a SHNO with d = 240 nm, with I_{RF} = 0.8 mA, H = 650 Oe and $\theta_H = 210°$.

5.3.4 TRSKM Measurements with increased I_{DC}

The polar images are unaffected by the artefact. Figure 5.11a shows polar images acquired for different I_{DC} values, with the phase and amplitude of I_{RF} fixed. While the FMR mode is observed at all I_{DC}, an increased amplitude of Kerr rotation is present at the NC tips for the current range 17 to 19 mA. By extracting the maximum absolute Kerr rotation from figure 5.11a, a clear threshold behaviour can be observed at $I_{RF} =$ 17 mA, plotted in figure 5.11b. For small I_{DC} values the amplitude of the FMR mode increases gradually with increasing I_{DC} as the injection of DC spin current into the Py layer compensate the damping. In figure 5.11c the images from 5.11a have been replotted after subtracting the image for which I_{DC} = 0, in order to isolate the dynamics associated with the DC current. For $I_{DC} \geqslant$ 10 mA a region of negative contrast appears to the right of the NCs. The asymmetry of the FMR response about the centre of the device reflects the mixed symmetry of the torques present. The STT and the torque due to the in-plane Oersted field are symmetric about the centre while the torque due to out of plane Oersted field is antisymmetric, shown in chapter 4.

The microwave spectroscopy data of figure 5.1b revealed the presence of a bullet mode for I_{DC} between 18 and 20 mA. However figure 5.11 shows strong out of plane dynamics at the NC tips for I_{DC} = 17 mA, that is still present when I_{DC} = 19 mA. The reduction of the threshold value for I_{DC} is due to the presence

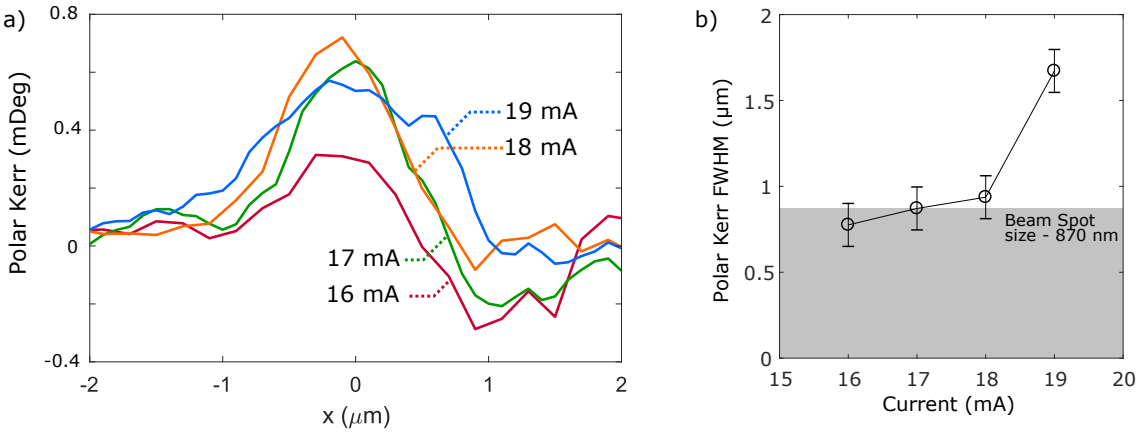

Figure 5.12: a) Cross sections through figure 5.11c b) estimated horizontal FWHM of the observed bullet, gray box indicates the optical beam spot size.

of the I_{RF}, as observed previously.[99] Figures 5.11a and c also demonstrate that the extent of localization of the bullet mode depends upon I_{DC}. Comparing the images for I_{DC} between 17 between 19 mA, the bullet mode is observed to occupy a larger region as I_{DC} is increased, with some reduction in the maximum Kerr amplitude. Since the diameter of this region is large compared to that of the bullet mode in figure 5.9a, this suggests that the bullet exhibits significant translational motion while being phase-locked to I_{RF}.

To further demonstrate this, figure 5.12a shows cross sections through the images in figure 5.11c, with the calculated FWHM in figure 5.12a as a function of current. For lower I_{DC} the bullet is observed to be of similar size to the optical beam spot. However, for I_{DC}= 19 mA there is a significant increase in the size of the area occupied by the bullet mode, without a significant reduction in Kerr amplitude.

To understand this, it is necessary to reconsider the results of chapter 4, whereby the torques present due to I_{RF} extended into the wider disk as a result of lateral current spreading. The bullet mode is therefore pulled towards where the STT is larger, and may either oscillate or gyrate about the centre. The bullet could either establish a stable trajectory, or escape and be damped in the extended disk, allowing another bullet to form at the centre and repeat the process. Increasing

I_{DC} is likely to increase the mobility of the bullet, allowing it to move further from the centre. Since the linewidth of the microwave emission in 5.1b is only weakly dependent on I_{DC}, formation of a stable trajectory seems the more likely scenario.

A similar behaviour was observed in micromagnetic simulations in figure 5.6, whereby the absence of a pinning site enabled the mode to move into the extended disk. Further work is required to understand the STT present due to the spatial spreading of I_{RF}. However for accurate simulations, precise knowledge of the spatial distribution of I_{RF} is required.

5.4 Summary

In summary, the dynamics of the bullet mode have been explored with experimental and micromagnetic methods. Fundamental and harmonic injection locking of the spin wave bullet can be achieved, synchronising the mode to an injected RF current. Under DC and RF an currents, the Py disk is observed to support both a bullet mode and off-resonance FMR precession in superposition. These responses could be separated, yielding polar and in-plane contrast associated with the bullet mode's presence. Simulations containing the DC current and Oersted field distributions demonstrated the bullet to be a highly mobile object, such that a pinning site was required for stable precession. These results led to the conclusion that the in-plane contrast was obscured by an artefact due to the edges of the thick electrical contacts. The localization of the bullet was found to decrease as the injected DC current was increased above the threshold value, and is attributed to spreading of the RF current from the centre of the device. Further work is now required to determine the trajectory of the bullet within this more complicated torque landscape.

CHAPTER 6

Current-induced picosecond magnetisation dynamics in Ta/CoFeB/MgO Hall Bars

6.1 Introduction

The generation of ever increasing amounts of data demands faster and more energy efficient device technologies, and a reevaluation of the traditional separation between processing and storage functions. Magnetic Random Access Memory (MRAM) promises lower write currents and reduced volatility compared to existing dynamic RAM (DRAM).[117] The latest generation of MRAM encodes information by using spin transfer torque (STT) to switch the magnetisation of the "free" layer in a magnetic tunnel junction (MTJ) structure, while the tunnel magnetoresistance (TMR)[118] allows the magnetic state of the free layer to be read back with high signal-to-noise ratio. Both TMR and current induced switching using STT have been the subject of extensive research.[101,119–128] MTJs with perpendicular magnetic anisotropy (PMA) are favoured for their high thermal stability and switching characteristics. While data may be written by passing current vertically through

the tunnel barrier, the necessary current densities lead to reduced device lifetimes. Therefore generation of STT by an in-plane current, by means of spin-orbit torques (SOTs) is particularly attractive. Heavy metal/ferromagnet/oxide trilayer structures may exhibit the spin Hall effect (SHE) as current flows through the heavy metal leading to the injection of spin current into the ferromagnet with a resulting STT. Due to its asymmetric interfaces, additional STT may be generated by means of the Rashba effect (RE) as current flows through the ferromagnetic layer, while the oxide layer may also serve as the tunnel barrier if the trilayer is incorporated into a MTJ stack.

Ta/CoFeB/MgO structures have shown particular promise for SOT induced switching.[129–136] Previous studies have used short electrical pulses (with duration from 300μs to 3 ns) to observe current driven and current assisted switching.[120,122,134] However, the response of the sample magnetisation has not been measured on the ps timescales on which switching is expected to occur. Furthermore, there is continued debate about whether the STT has components parallel or perpendicular to the plane defined by the magnetisation and the injected spin polarization vector, with layer thickness and fabrication conditions appearing to play a key role.[130,133] In the present work, measurements of the polar magneto optical Kerr effect (MOKE) with an in-plane applied magnetic field are made to explore the static and dynamic properties of Ta/CoFeB/MgO Hall bars that possess PMA. Hysteresis loops and the field-dependent precession frequency suggest that a higher order magnetic anisotropy influences the alignment of the static magnetisation. Time resolved scanning Kerr microscopy (TRSKM) measurements show that the magnetisation dynamics induced by a current pulse with ps rise time are well described by the Landau-Lifshitz -Gilbert (LLG) equation and dominated by the action of the in-plane STT.

6.2 Experimental Set-up

Hall bars of 20 x 140 μm^2 size with Au contacts, shown in Figure 6.1a, were formed from Si/Ta(4 nm)/$Co_{40}Fe_{40}B_{20}$(1 nm)/MgO(1.6 nm)/Ta(1 nm) thin films produced by magnetron sputtering. Details of the fabrication process and characterisation by static Kerr microscopy and Hall resistance measurements have been reported previously.[137] In the present study, the probe beam of the TRSKM was used to record the out-of-plane component of magnetisation, by means of the polar MOKE. Wire-bonds were used to connect the Hall bar to the end of a 50 Ω coplanar waveguide (CPW), so that high frequency electrical current could be passed along the length the Hall bar (in the $\hat{\boldsymbol{x}}$ direction). Current passing through the 4 nm Ta underlayer is expected to generate a spin current propagating perpendicular to the plane, into the CoFeB layer, by means of the SHE.[138] Low frequency current waveforms were previously shown to induce stochastic switching of the CoFeB magnetisation by propagation of domain walls from the edges of the device.[137] In the present work, stroboscopic TRSKM measurements are used to observe deterministic magnetisation precession, from which the nature of the driving torques can be inferred.

6.3 Theoretical Framework

A macrospin model may be used to describe the static and dynamic behaviour of the CoFeB magnetisation. The magnetic free energy density is assumed to have the form

$$E = -\boldsymbol{M} \cdot \boldsymbol{H} + 2\pi M^2 m_z^2 - K_1(\boldsymbol{m} \cdot \hat{\boldsymbol{z}})^2 - K_2(\boldsymbol{m} \cdot \hat{\boldsymbol{z}})^4, \tag{6.1}$$

where $\boldsymbol{M}$ is the magnetisation vector, $\boldsymbol{m}$ is a unit vector parallel to the magnetisation ($\boldsymbol{m} = \boldsymbol{M}/M$), $\boldsymbol{H}$ is the applied field, and K_1 and K_2 are the first and second order anisotropy constants that give rise to the PMA. The orientation of the static

magnetisation is obtained by minimising the energy density using a numerical non-linear equation solver. Hysteresis loops may be calculated by obtaining a solution at a particular field value, and then using the obtained value as the starting point for the next calculation at a somewhat different field value. Typically the calculation begins by assuming quasi-alignment of $\boldsymbol{M}$ with $\boldsymbol{H}$ at high field.

The dynamic response of the magnetisation to an injected current can be calculated from the LLG equation

$$\frac{d\boldsymbol{M}}{dt} = -|\gamma|(\boldsymbol{M} \times \boldsymbol{H}_{eff}) + \frac{\alpha}{M}\boldsymbol{M} \times \frac{d\boldsymbol{M}}{dt} - |\gamma|A\boldsymbol{M} \times (\boldsymbol{M} \times \hat{\boldsymbol{y}}) + |\gamma|B(\boldsymbol{M} \times \hat{\boldsymbol{y}}) \quad (6.2)$$

where the third and fourth terms on the right hand side are the "in-plane" (in the plane defined by $\boldsymbol{M}$ and $\hat{\boldsymbol{y}}$) anti-damping torque proposed by Slonczewski, and the "out-of-plane" field-like torque. Here γ is the gyromagnetic ratio, $\boldsymbol{H}_{eff}$ is the effective field calculated from the gradient of the energy density with respect to the magnetisation, α is the Gilbert damping constant, and A and B define the amplitudes of the anti-damping and field-like torques respectively. An ordinary differential equation solver[139] may be used to calculate the trajectory of the magnetisation in response to a time dependent current and/or magnetic field.

6.4 Experiment and Modelling

Hysteresis loops of normalized out-of-plane magnetisation m_z in response to an in-plane static field were first acquired to both explore the equilibrium orientation of the magnetisation, and identify anisotropy constants. Individual and averaged loops obtained for $\boldsymbol{H}||\hat{\boldsymbol{x}}$ and $\boldsymbol{H}||\hat{\boldsymbol{y}}$ are plotted in figures 6.1b & c. For $\boldsymbol{H}||\hat{\boldsymbol{y}}$ the switching process is highly repeatable. While propagation of domain walls may lead to switching at the coercive field, it is likely that the other sections of the loop are associated with coherent rotation of the magnetisation.

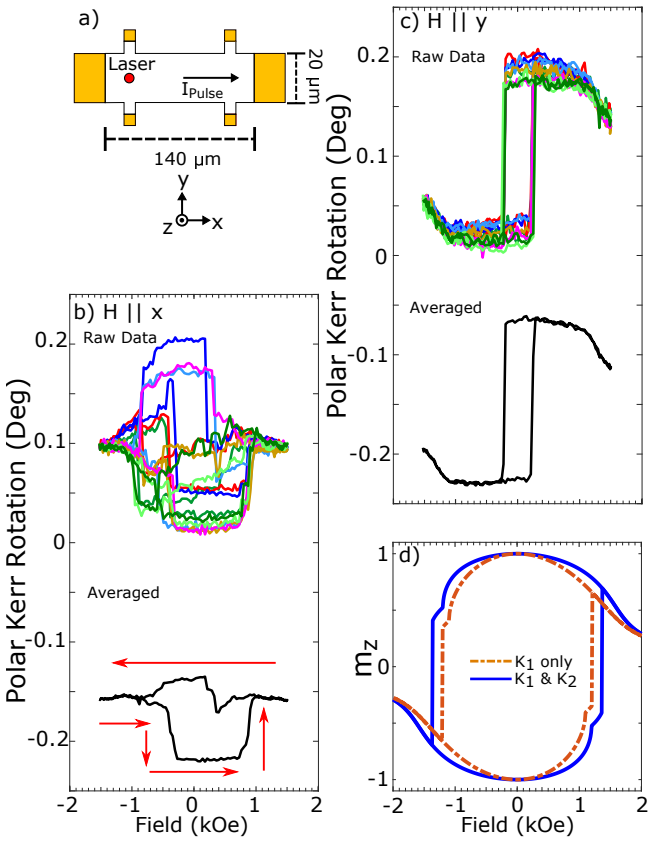

Figure 6.1: a) Schematic of the Hall bar and co-ordinate system used, with beam spot position and direction of positive current indicated. Individual and averaged measured hysteresis loops for b) $\boldsymbol{H}||\hat{\boldsymbol{x}}$, and c) $\boldsymbol{H}||\hat{\boldsymbol{y}}$. d) Calculated loops are shown for $\boldsymbol{H}$ canted out of the plane by an angle of 5°, assuming M = 1000 emu/cm^3, K_1 = 7.0 $\times 10^6$ erg/cm^3, and K_2 = 0 and 0.15$\times 10^6$ erg/cm^3.

A different behavior is observed for $\boldsymbol{H}||\hat{\boldsymbol{x}}$, where loops repeated under similar conditions exhibit different shapes. While some of the individual loops may exhibit regions of coherent rotation, there are also numerous sharp transitions to intermediate values of the out-of-plane magnetisation. With $\boldsymbol{H}$ applied in-plane and for H less than the saturation value, the magnetisation may be canted into or out of plane with equal probability so that a domain structure is expected. Therefore the observed stochastic behaviour is most likely associated with domain walls entering and leaving the area of the focused optical probe spot that had $\sim$ 600 nm diameter. The loops in figure 6.1c demonstrate a higher level of repeatability as the field is swept from negative to positive values. Similar behaviour within CoFeB Hall bars has previously been attributed to nucleation of domain walls

with a particular chirality due to the Dzyaloshinskii-Moriya interaction (DMI),[125,140] although the DMI is expected to be small in the present case.[141,142]

The different behaviours observed in figure 6.1b and 6.1c may be attributed to either an in-plane magnetic anisotropy or to $\boldsymbol{H}$ being misaligned relative to the plane of the film by different amounts. Measurements made previously with an out-of-plane magnetic field yielded a coercivity of about 10 Oe. Given the coercivity of 280 Oe observed in figure 6.1c, $\boldsymbol{H}$ would have to be canted by about $\sim 2^{\circ}$ from the plane to yield an out of plane field component of similar magnitude. Misalignment of this order can be expected due to the construction of the quadrupole electromagnet used in the TRSKM. A canting angle of 5° was assumed for both the $\boldsymbol{H}||\hat{\boldsymbol{x}}$ and $\boldsymbol{H}||\hat{\boldsymbol{y}}$ cases for the purposes of macrospin modelling, so as to better reproduce the field dependence of the precession frequencies that will be discussed later.

The measured hysteresis loops exhibit a degree of 'squareness' to them, in the case of figure 6.1b this can likely be attributed to the role of domain wall processes. However, the coherent rotation in the loops of figure 6.1c suggest a single domain state is present and so the 'squareness' in these loops must be due to higher order anisotropy. Represented by the K_2 parameter.

A calculated hysteresis loop is shown in figure 6.1d. The macrospin calculations are not expected to reproduce the measured coercivity values which instead depend upon domain wall propagation. It should be noted that the inclusion of the higher order anisotropy term does not affect the saturation field when $\boldsymbol{H}$ is applied parallel to the sample plane, rather a positive value of K_2 tends to flatten the top of the loop. On the other hand the detailed shape of the MOKE loops may not accurately reflect the field dependence of the out of plane magnetisation component. The detailed shape of the averaged loop in 6.1c is different for positive and negative field values, and the top of the loop is less curved than that of an anomalous Hall effect (AHE) loop obtained from the same sample.[137] The AHE loop may contain contributions from the planar Hall effect, while higher

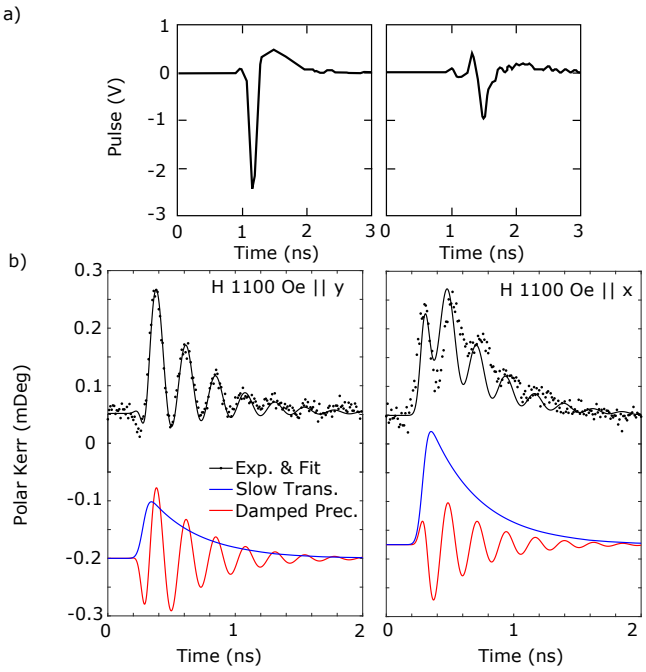

Figure 6.2: a) Pulse reflected from the Hall bar device (right), and from the end of the open circuit connecting cable when detached from the device (left). b) Time dependent polar MOKE for static field $\boldsymbol{H}||\hat{\boldsymbol{x}}$ and $\boldsymbol{H}||\hat{\boldsymbol{y}}$. The black dots are the experimental points while the black line is a guide to the eye composed of a transient background (blue line) and a damped oscillation (red line). The black curve has the form $f_{pulse}(t)[asin(2\pi ft+\phi)+b]$ with amplitudes a and b, frequency f, and phase ϕ. The pulse profile has the form $f_{pulse}(t) = erf(t/T_1)exp(-t/T_2)$ with rise and decay times T_1 = 50 ps and T_2 = 290 ps respectively. For $\boldsymbol{H}||\hat{\boldsymbol{y}}$, $a =$ 0.08, $b =$ 0.06, and $\phi =$ 42°, while for $\boldsymbol{H}||\hat{\boldsymbol{x}}$, $a =$ 0.06, $b =$ 0.12, and $\phi =$ -145°.

order contributions can modify the MOKE loops,[143] so that caution is required in interpreting the detailed shape of each type of loop. Assuming a value of M = 1000 emu/cm^3,[127,138] values of K_1=7.0$\times$10^6 erg/cm^3 and K_2=0.15$\times$10^6 erg/cm^3 were found to best describe the time resolved data to be presented later, while providing an adequate description of the loop shape.

A small amplitude precession was excited by passing a current pulse of 70 ps full width half maximum (FWHM) duration parallel to the long axis of the Hall bar. The pulse reflected from the device was directed into an oscilloscope by means of a directional coupler. Figure 6.2 compares the pulse reflected from the device with that reflected from the cable to the device after it had been detached from the device fixture (the open circuit cable fully reflects the pulse). The amplitude of the

pulse reflected from the device is smaller by a factor ∼2.5 and is broadened with some additional structure visible. This suggests imperfect impedance matching between the device and the connecting cable, and loss within the device, such that the detailed form of the pulse at the Hall bar sample is not known precisely.

Examples of the resulting time dependent polar Kerr rotation signals are shown in figure 6.2b for $\boldsymbol{H}||\hat{\boldsymbol{x}}$ and $\boldsymbol{H}||\hat{\boldsymbol{y}}$, together with a guide to the eye, which consists of a damped oscillatory term and a transient background. The temporal form of the transient background is the same for both measurements and is inferred to be similar to that of the current pulse within the Hall bar. The oscillations are well described by the damped sinusoid for $\boldsymbol{H}||\hat{\boldsymbol{y}}$, while an irregular variation of the amplitude of successive cycles of oscillation is observed for $\boldsymbol{H}||\hat{\boldsymbol{x}}$. This latter behaviour can be attributed to additional finer scale structure within the current pulse profile that can cause coherent suppression, or enhancement, of precession at certain frequencies.[144,145]

The time resolved data can be described by a numerical solution of equation 6.2. The simulations assumed the same values of M, K_1, K_2, and field canting angle as for the hysteresis loop represented by the dashed curve in figure 6.1d. A value of α = 0.05 was found to give a reasonable description of the damping of the observed oscillations, this relatively large value being attributed to spin pumping into the Ta layer. The pulse generator produces a pulse of 7V amplitude and 70 ps FWHM duration. From figure 6.2a the pulse reflected from the device appears stretched in time to ∼1 ns and has its amplitude reduced by ∼ 60%. As a result, a peak current amplitude of about 6 mA and hence a peak charge current density of 6×10^6A/cm^2 are expected within the Ta layer of the Hall bar. This in turn leads to an in-plane Oersted field of 1.8 Oe along the y axis at the middle of the Hall bar where the probe spot was positioned. While the edges of the Hall bar are known to posses an out of plane Oersted field, these measurements are focused on the center of the device where the Oersted field mostly lies in the y direction.[137] The peak amplitude of the spin current density J_s, in charge units, was assumed to

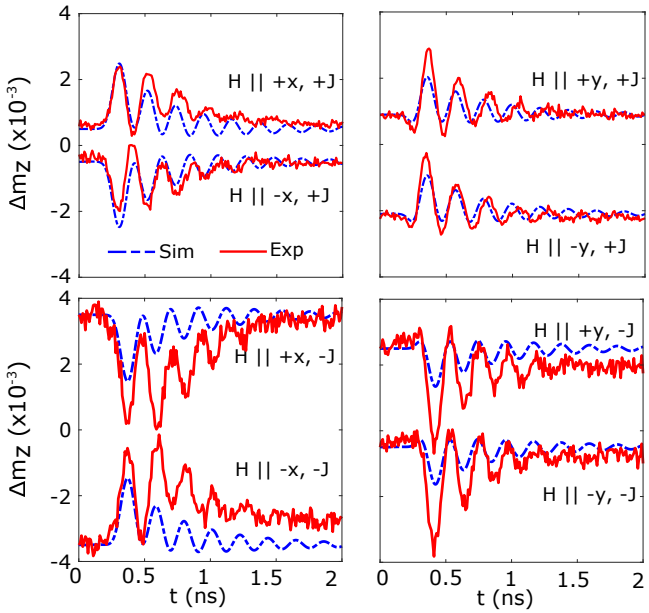

Figure 6.3: Comparison of experimental (red) and simulated (blue) out of plane magnetisation component with a static field H = 900 Oe, applied along either the $\hat{\boldsymbol{x}}$ or $\hat{\boldsymbol{y}}$ axes, for all possible combinations of field and current polarity. The parameter values used within the simulations are described within the main text.

be equal to that of the charge current density multiplied by a spin Hall angle of $\sim$0.08[138] and an additional factor of 0.25 was required for improved agreement, which may occur from finite spin transmission at the Ta/CoFeB interface (value was identified by comparison of experimental and simulated results). The amplitude of the in-plane STT term has the form $A = \hbar J_s/(2eMd)$ where d is the thickness of the CoFeB layer, leading to an effective field amplitude of $AM \sim 4 \times 10^3$ Oe. The amplitude of the out of plane STT is expected to be small in the present material and similar works have found good agreement without its inclusion.[146,147] As a result, the value of B was set equal to zero in the present study. The Oersted field produces a torque of equivalent analytical form to the out of plane STT but its amplitude is small compared to that of the in-plane STT.

The measured and simulated components of the normalized out of plane component of magnetisation m_z are shown in Figure 6.3 for the case that a field H = 900 Oe is applied along either the $\hat{\boldsymbol{x}}$ axis or the $\hat{\boldsymbol{y}}$ axis, for all possible combinations of field and current polarity. For H = 900 Oe the calculated hysteresis loop

of figure 6.1c shows that $\boldsymbol{M}$ is in a canted state so that tracking the orientation of the different field and torque vectors is complicated. The simulations assumed that H was reduced from +1400 Oe to the stated value in each case. For the case of $\boldsymbol{H}||\pm\hat{\boldsymbol{x}}$ with negative current density it was necessary to multiply the measured signal by a factor of -1 in order to obtain agreement with simulation. This is attributed to the lockin amplifier having been re-phased before this pair of measurements. For a particular field direction, the phase of the simulated oscillations may vary by up to about π/2 rads between the 4 different cases of field and current polarity. The absolute phase of the measured oscillations is uncertain due to drift (often of thermal origin) and a possible change in path length when the sign of the current was reversed. Therefore the simulated traces were shifted in order to achieve better agreement with simulation, the simulated traces for negative currents underwent an additional shift of 55 ps (owing to the electrical path length). Nevertheless a single set of material and experimental parameters is seen to be reasonably successful in predicting the frequency and phase of the observed oscillations and the polarity of the transient background.

The dependence of the observed and simulated m_z signals upon H is presented in figure 6.4. Again the same set of simulation parameters used in figure 6.3 is seen to provide good agreement between experiment and simulation. The largest differences are observed for $\boldsymbol{H}||\hat{\boldsymbol{x}}$ at the largest field values. The amplitude of oscillation is suppressed, presumably due to fine structure in the profile of the current pulse, as suggested previously in relation to figure 6.2b. This accentuates the appearance of the transient background which is seen to increase as H is increased. This background is about a factor of two greater for $\boldsymbol{H}||\hat{\boldsymbol{x}}$ compared to $\boldsymbol{H}||\hat{\boldsymbol{y}}$.

The slow transient can be understood from considering the effective field due to the in-plane STT, which lies parallel to $\boldsymbol{M}\times\hat{\boldsymbol{y}}$. Figure 6.5 shows the direction of the $\boldsymbol{M}\times\hat{\boldsymbol{y}}$ effective field for select cases of figure 6.4. For large H values $\boldsymbol{M}$ lies close to $\boldsymbol{H}$ so that for $\boldsymbol{H}||\hat{\boldsymbol{x}}$, the effective field lies normal to the plane of the

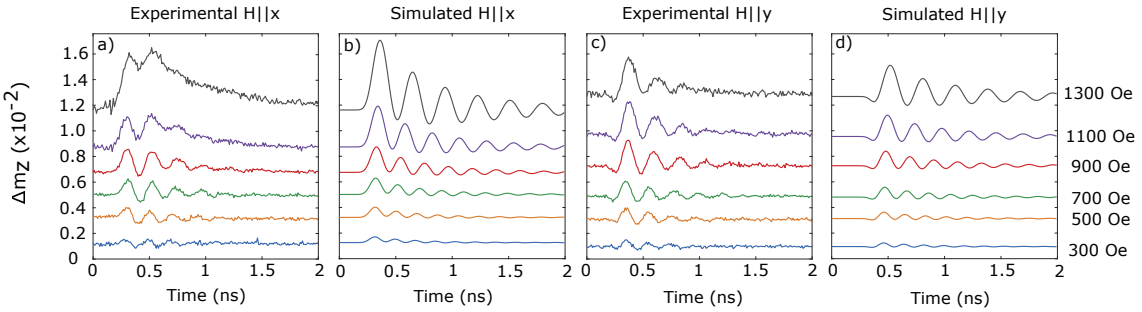

Figure 6.4: Comparison of simulated and experimental normalized out of plane magnetisation component m_z for different values of H, the static applied field. a) experiment and b) simulation for $\boldsymbol{H}||\hat{\boldsymbol{x}}$. c) experiment and d) simulation for $\boldsymbol{H}||\hat{\boldsymbol{y}}$ direction. The simulations assume the same material parameter values as used in figure 6.3, and that are described within the main text.

sample and causes the transient deflection of $\boldsymbol{M}$ out of the plane. Alternatively for $\boldsymbol{H}||\hat{\boldsymbol{y}}$, both the Oersted field and static field lie in the $\hat{\boldsymbol{y}}$ direction while $\boldsymbol{M}$ lies in the yz plane. Upon injection of the electrical pulse, the Oersted field will temporarily either pull $\boldsymbol{M}$ further in-plane or out-of-plane (dependant on the relative orientations of Oersted and static fields). This serves to displace the equilibrium about which the magnetisation precesses. As can be seen from the gradient of the hysteresis loops, this only translates to a significant out-of-plane component for higher fields. Indeed when removing the Oersted field from simulations, the slow transient is completely suppressed. The reason for the reduced slow transient in this geometry is that the Oersted field is much weaker than the STT effective field.

The macrospin model can also be used to describe the magnetisation reversal induced by larger pulsed currents. Assuming identical material parameters and an identical temporal profile for the current to that used to describe the small amplitude precession, the current amplitude was increased until m_z was observed to change sign. The minimum peak current density required for switching (J_{switch}) for each static field value is plotted in figure 6.6a. The relationship between J_{switch} and H is observed to be close to linear, while a somewhat lower value of J_{switch} is observed for $\boldsymbol{H}||\hat{\boldsymbol{x}}$, suggesting that the enhanced transient background observed in figure 6.4 aids the switching process.

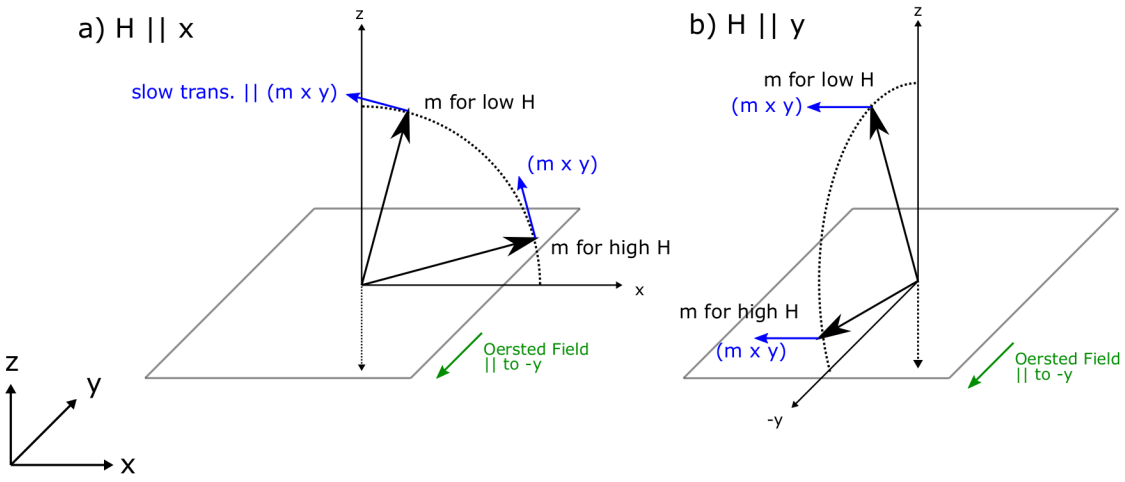

Figure 6.5: Schematic depicting orientation of slow transient background (which lies in the $\boldsymbol{M} \times \hat{\boldsymbol{y}}$ direction), for high and low H in both the $\hat{\boldsymbol{x}}$ and $\hat{\boldsymbol{y}}$ directions. Demonstrating that significant out-of-plane slow transient only occurs for high fields close to the $\hat{\boldsymbol{x}}$ axis. Oersted field from pulsed current is also shown, and lies in the the $-\hat{\boldsymbol{y}}$ direction for all cases.

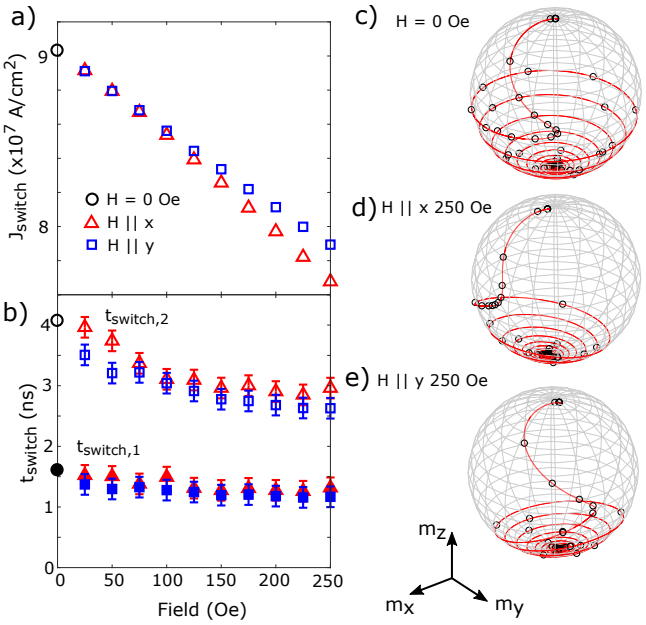

Figure 6.6: Macrospin simulations of current-induced magnetisation reversal. a) Minimum current density required for magnetisation reversal for the case of no bias field (black circle), $\boldsymbol{H}||\hat{\boldsymbol{x}}$ (red triangles), and $\boldsymbol{H}||\hat{\boldsymbol{y}}$ (blue squares). b) Switching times $t_{switch,1}$ and $t_{switch,2}$ associated with the minimum current density in (a). Magnetisation trajectories are plotted for the case of c) no bias field, (d) H = 250 Oe applied parallel to $\hat{\boldsymbol{x}}$ and (e) H = 250 Oe applied parallel to $\hat{\boldsymbol{y}}$. Open symbols are placed at intervals of 0.2 ns.

Two measures of the time required for switching are plotted in figure 6.6b. The first, $t_{switch,1}$, considers the time taken for m_z to change sign (i.e. to move from it's equilibrium position to crossing the xy plane) while the second, $t_{switch,2}$, considers the time taken for $\boldsymbol{M}$ to switch from one equilibrium position (for +ve m_z) to within 5% of the other equilibrium position (for -ve m_z). Increasing in-plane bias field is observed to lead to a reduction $t_{switch,2}$ by $\sim$31$\pm$8$\%$ and a slight reduction in $t_{switch,1}$ of 23$\pm$9$\%$, while the orientation of the in-plane field has little effect. Examples of the magnetisation trajectory have been plotted in figures 6.2c, d and e. It may be seen that $\boldsymbol{M}$ moves to the xy plane during the first half-cycle of precession and then relaxes to the new equilibrium position over the course of a number of further cycles. In the absence of a bias field the magnetisation spends more time near the xy plane before precessing towards the new equilibrium position. At any particular value of the bias field, increasing J_{switch} causes both t_{switch} values to be reduced. The single domain model may provide a reasonable description of sub-micron elements used in MRAM applications. The present simulations show that the use of in-plane bias field can potentially decrease the time taken for full magnetisation reversal by about 25 percent.

Additional simulations were carried out in order to further explore the switching process. By employing two electrical pulses it is possible to 'write' and 'reset' the magnetisation state. This was done in the absence of static field, and for H = 250 Oe applied in the $\hat{\boldsymbol{x}}$ and $\hat{\boldsymbol{y}}$ directions, shown in figure 6.7. These simulations demonstrate different requirements on pulse polarity exist for different orientations of $\boldsymbol{M}$, shown in figure 6.7. For $\boldsymbol{M}$ close to the $\hat{\boldsymbol{z}}$ axis (as in figure 6.7a) the 'write'-'reset' switching process is most efficient (i.e the lowest current amplitude) for pulses of opposite polarity. This holds true for $\boldsymbol{M}$ canted in the xz plane (as in figure 6.7b), but not for $\boldsymbol{M}$ canted in the yz plane (as in figure 6.7c). For $\boldsymbol{M}$ within the yz plane the 'write' and 'reset' processes is instead most efficient for pulses of the same polarity.

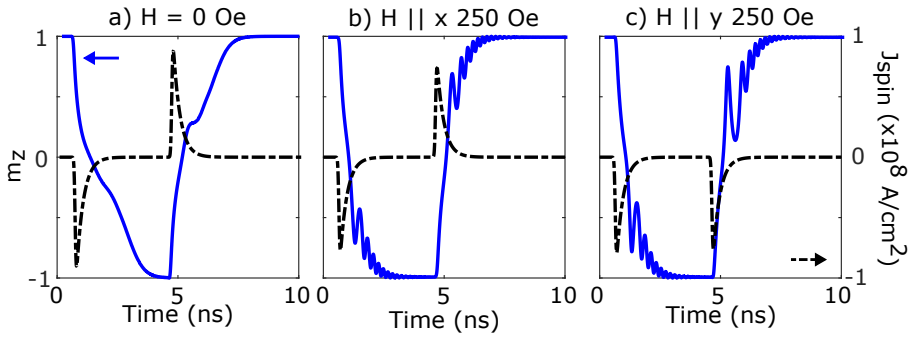

Figure 6.7: Macrospin simulations of current-induced magnetisation reversal, for the injection of a second electrical pulse with the same temporal profile. Solid blue line shows the m_z component of magnetisation, dashed black line shows the amplitude of spin current injected. Simulations were carried out for three static field configurations a) H = 0 Oe, b) $\boldsymbol{H}||\hat{\boldsymbol{x}}$ with a magnitude of 250 Oe, and c) $\boldsymbol{H}||\hat{\boldsymbol{y}}$ with a magnitude of 250 Oe.

It should be possible to understand this qualitative difference in 'write'-'reset' switching processes from considering the torques (or rather the effective fields) present in each state. Drawing on the the slow transient discussed earlier, figure 6.8 shows the effective fields present for two magnetic states that lie in the xz and yz planes (for -ve current pulses). With $\boldsymbol{M}$ in the xz plane, the slow transient is driven by the STT effective field, the vertical component of which is the same for both states. Hence if the slow transient aids in switching opposite pulse polarities are required for 'write' and 'reset' processes. With $\boldsymbol{M}$ in the yz plane the Oersted field drives the slow transient, which does not follow the same symmetry. However, as the Oersted field possesses no z component it is not immediately clear how this drives switching, requiring further work in order to be understood.

6.5 Summary

In summary, TRSKM measurements have been performed upon a Ta(4 nm)/ $Co_{40}Fe_{40}B_{20}$(1 nm)/MgO(1.6 nm)/Ta(1 nm) Hall bar to gain understanding of the spin-orbit torques present. Including higher order anisotropy term was found to improve the agreement of model and experiment for hysteresis loops with an in-

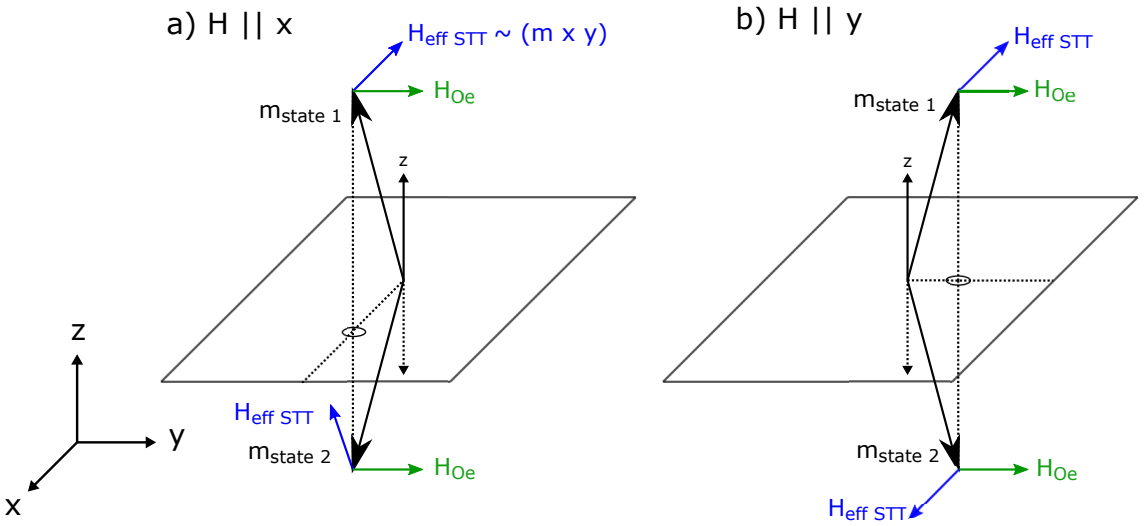

Figure 6.8: Schematic depicting the direction of effective fields due to anti-damping STT and Oersted fields. For two stable states (m_{state1} and m_{state2}) canted away from the vertical due to a static field applied in the a) $\hat{\boldsymbol{x}}$, and b) $\hat{\boldsymbol{y}}$ directions.

plane field, and to reproduce the frequency of precession. Macrospin simulations provide a good description of the frequency and phase of precession as the field strength and current polarity is varied. To do so required the inclusion the calculated Oersted field and in-plane spin-orbit torque, justifying that the out-of-plane STT is negligible in this system. Extending the simulations to the coherent magnetisation reversal expected within MRAM elements, the inclusion of a modest in-plane bias field is found to reduce both the switching current and the time required for switching. Furthermore, the pulse polarities required for 'writing' and 'resetting' are dependent on the static field orientation, which is of immediate practical interest.

CHAPTER 7

Magnetisation Dynamics in Ta/CoFeB/MgO Elements driven by Unipolar and Bipolar Current Pulses

7.1 Introduction

Current-induced switching in spin orbit torque (SOT) devices, is expected to be driven by two mechanisms. For extended structures (i.e. those larger than the domain wall width) the quasistatic switching process is driven by domain wall nucleation and propagation.[140] For smaller devices, nucleation may be suppressed and switching is obtained via coherent processes. The cross-over from domain-driven to coherent processes leads to an increase in threshold switching current,[134,147] yet with potential for faster swtiching.[148]

The work detailed in this chapter builds on that of chapter 6, but instead of extended Hall bars smaller elements will be considered. These elements have been specifically designed for high frequency measurement by TRSKM, with a

device layout enabling the injected pulse to be measured by an oscilloscope. Chapter 6 used TRSKM to infer the torques present in a Ta/CoFeB/MgO Hall bar, and through macrospin modelling determined that static bias fields applied parallel to the direction of current are most conducive to magnetisation reversal.

In this chapter the static and dynamic properties of CoFeB elements will be explored. These structures bear closer resemblance to those considered for MRAM applications and their response to DC currents over long timescales (long compared to the ns write times expected for MRAM) has been well studied. Here, static Kerr microscopy will explore the evolution of the domain structure within the elements, to better understand the ground state of such devices. The dynamic behaviour excited by single electrical pulses will be observed in TRSKM, demonstrating the importance of understanding the underlying domain structure. By supplying a bi-polar electrical pulse, observation of time-resolved switching processes by TRSKM will be attempted. Finally XPEEM measurements will be used to explore variations in the ground state between nominally identical devices.

7.2 Device Specification

The devices described here were designed specifically for TRSKM measurements in order to overcome some of the difficulties encountered in chapter 6. To minimize loss due to impedance matching, current was delivered via picoprobes to CPWs with a 50 Ω characteristic impedance. The size of the CPWs was designed specifically for the picoprobe configuration used in the TRSKM.

A silicon substrate supported a Ta underlayer on which both the elements and gold waveguides were grown. The elements themselves consisted of a $Co_{40}Fe_{40}B_{20}$(1 nm)/MgO (1.6 nm)/Ta (1 nm) stack. Thick gold CPWs were deposited over the Ta underlayer so as to create an overlap as in figure 7.1. Four wafers were grown that combined Si of higher and lower resistivity ($\rho \geqslant 1000$ Ω cm & $\rho \geqslant 500$ Ω cm) and a Ta underlayer thickness of 4 or 8 nm. In this chapter

only the 4 nm Ta underlayer will be considered, while full details of the fabrication processes and design choices can be found in [149].

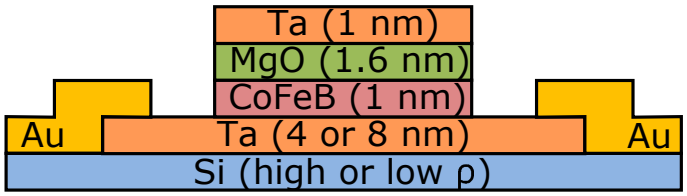

Figure 7.1: Stack structure where Au contacts overlap with the Ta under layer to ensure a low resistance electrical connection. Wafers were fabricated for all combinations of Si resistivity and Ta underlayer thickness, as described within main text.

A large variety of element sizes and shapes were fabricated on Ta underlayers of varying width. However TRSKM studies focused on the device depicted in figure 7.2. The three large tracks connect to the ground-signal-ground layout of the picoprobes. The CoFeB elements (inset of figure 7.2) sit in the center of the signal line. For this device, the elements had a square shape with side length in the range of 10 - 0.2 μm. When electrical current is applied to the device, each element should be exposed to the same spin current density, to aid the comparison between element sizes. Measurements showed that the samples on the low ρ wafer yielded a larger amplitude Kerr signal, and so these wafers were chosen for Kerr microscopy measurements.

7.3 Static measurements

Static polar MOKE microscopy was carried out to identify the ground state present in the CoFeB elements, as well as to demonstrate domain nucleation and expulsion. The 10 μm element (the largest fabricated) was first saturated by a field H of -1500 Oe applied in either the $\hat{x}$ or $\hat{y}$ directions, to remove any domains present. Then, starting from H = 0 Oe, the domain structure was observed as the field was increased to H = 500 Oe and then decreased again. Static Kerr microscopy results are plotted in figure 7.3. As these samples possess a large PMA, the

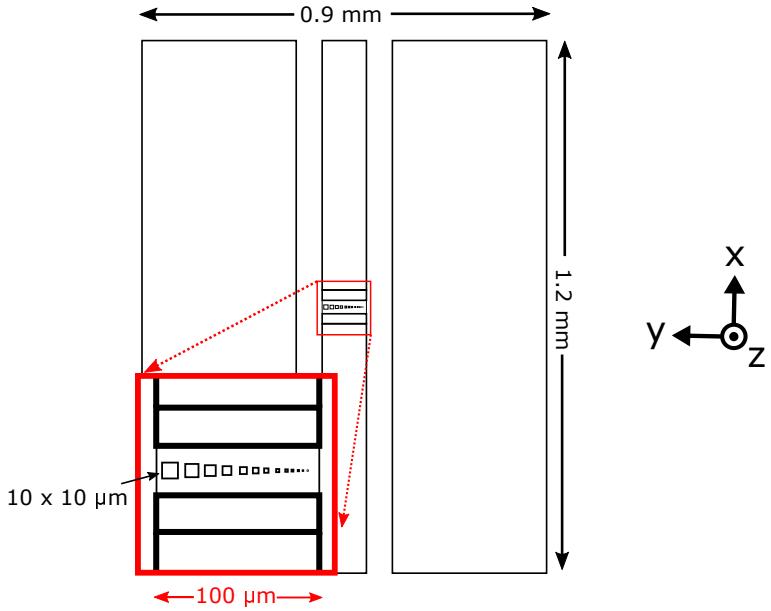

Figure 7.2: Schematic of the device on which TRSKM measurements were made. Large gold tracks connect to high frequency probes to deliver current to the CoFeB elements (inset). For this device, elements consist of squares of different length.

contrast observed in the absence of an applied field can be interpreted in terms of large domains with opposing out of plane magnetisation. As field is applied the domains reduce in size and a striped domain structure forms at $H \sim 150$ Oe. The domains continued to reduce in width and the polar MOKE signal decreased with increasing field. Extrapolating from measurements made at $H = 0 \rightarrow 150$ Oe, the anticipated domain width at $H = 200$ Oe is comparable to the beam spot size. As the higher fields pulled the magnetisation in-plane the polar MOKE signal was reduced, and as a result it is difficult to determine if domains are present at fields of 200 Oe or greater. Nevertheless, the lack of measurable change between domain images at $H = 400$ Oe and 500 Oe - for both increasing and decreasing field - suggested the presence of a single domain state, with magnetisation either saturated in-plane or slightly canted out-of-plane.

Interestingly, by comparing the low-field domain structures it is possible to identify domain pinning sites. For example, the lower left edge of the square was observed to posses a 'dark' domain which persisted for all applied field values.

The presence of such pinning sites implies that this system is relatively insensitive to field history.

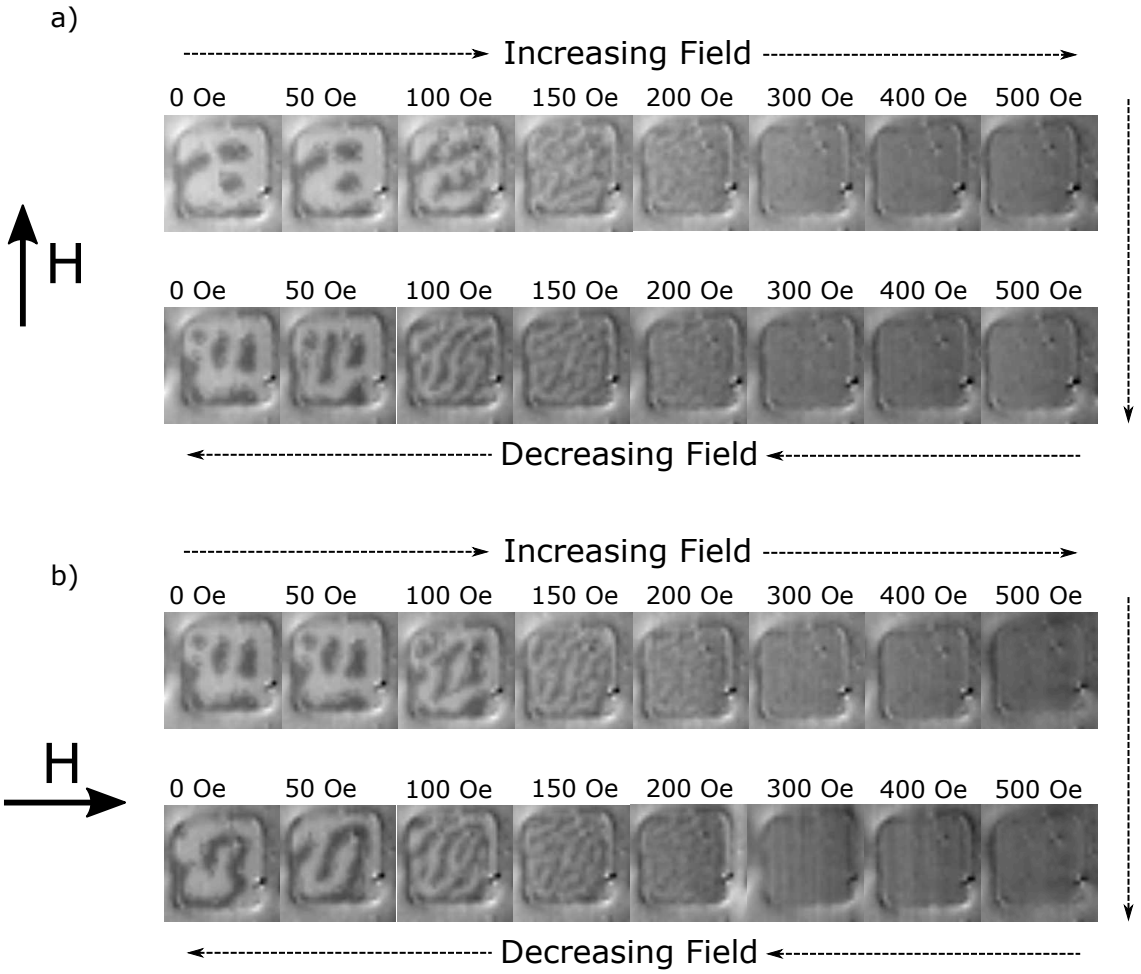

Figure 7.3: Magnetic domain nucleation and expulsion in 10×10 μm square element for increasing and decreasing fields applied in the a) $\hat{x}$ and b) $\hat{y}$ directions. Prior to measurement, a saturation field of -1500 Oe was applied in the same direction. Dashed arrows indicated the order of applied field values. (Also found in reference [149])

To understand the static behaviour and to make comparison with the Hall bars discussed in chapter 6, vector hysteresis loops were acquired with the field applied in the $\hat{x}$ and $\hat{y}$ directions, as shown in figure 7.4. The loops suggest a very different behaviour to those acquired from the Hall bars in chapter 6. From the M_z loops (c & f subfigures) it is difficult to discern whether a higher order PMA term is present. The same loops also suggest that the magnetisation was fully in-plane at H = 75 Oe. However this is not consistent with figure 7.3 where

domains can be seen up to H = 200 Oe. This is likely due to the reduction of domain width with applied field, such that multiple domains of opposite polarity lie within the optical probe spot averaging out to a near-zero Kerr rotation. The magnitude of the switching field however demonstrated a slight asymmetry, being larger for positive fields than negative fields, however this can likely be attributed to an offset in the Hall probe.

For the in-plane loops (subfigures a, b, d, & e) it is more challenging to determine the component of magnetisation parallel to the applied field. The M_z loops suggest that the magnetisation should be in-plane for fields greater than 75 Oe. However with the field applied along one of the in-plane directions the magnetisation component along that direction continued to increase rather than saturate with increasing field. Given that a single domain state should exist for fields greater than 300 Oe, the continued increase in Kerr rotation could be caused by mechanical motion of the sample at high fields (this would also explain why the background slope switches channel with field angle).

Similar polar MOKE microscopy measurements were performed on elements of different sizes in the absence of field, as shown in figure 7.5. The majority of elements tested demonstrated a multi-domain structure similar to that of the largest element. In order to further explore this behaviour it would be necessary to generate a saturating out-of-plane magnetic field, which is not possible in the current microscope set-up. As the element size decreased the elements appeared more circular than square, likely due to limitations in the photo-lithography process used in the fabrication.

The smallest element measured in figure 7.5 appeared to occupy a single domain state. The significance of this is that the element could potentially undergo reversal via coherent rotation as opposed to domain-wall processes, with any element smaller than this also being in a single domain state. Elements that switch this way require greater currents to do so, but have improved thermal stability. However such elements also have size comparable to or smaller than

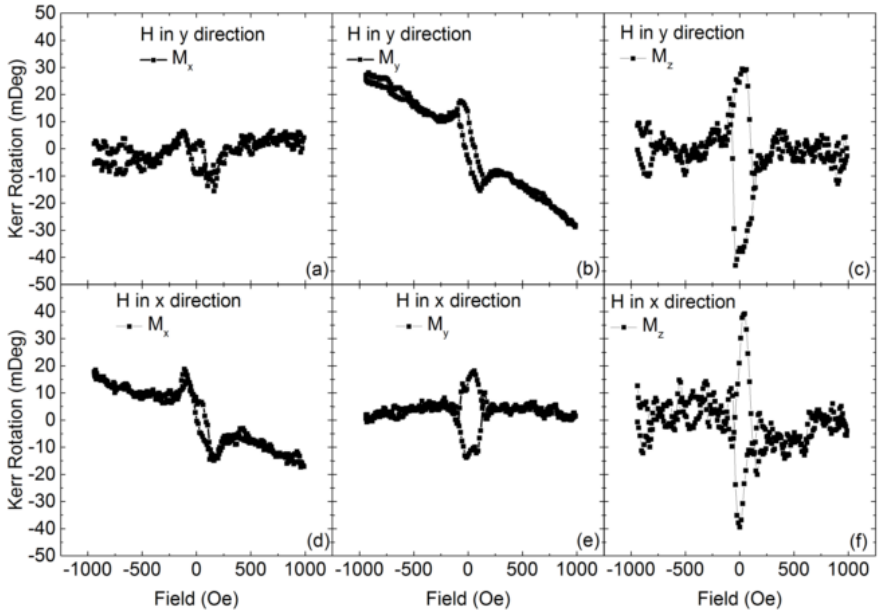

Figure 7.4: Vector resolved hysteresis loops for the 10 μm element, where the CPW signal line lies in the $\hat{x}$ direction. For a, b & c $\boldsymbol{H}$ lies in the $\hat{y}$ direction, whereas in c) d) & e) $\boldsymbol{H}$ lies in the $\hat{x}$ direction. Measurements were carried out with the optical spot in the center of the device. (Also found in reference [149])

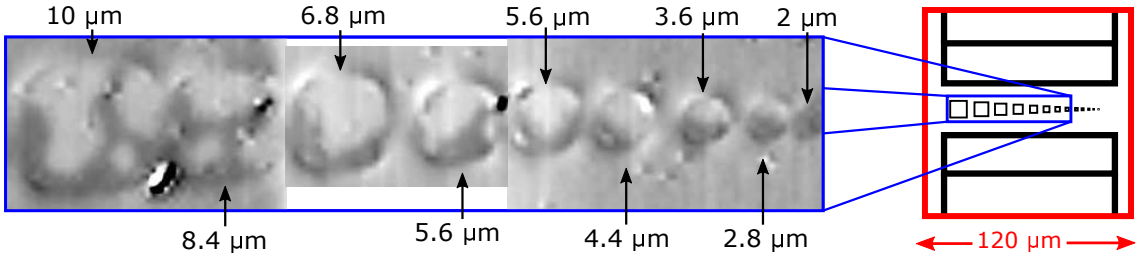

Figure 7.5: Remanent domain states observed in nominally square shaped elements of different size. Multi-domain states can be observed for elements down to 2.8 μm length, after which the magnetisation appears uniform.

that of the beam spot (870 nm). As the ground state is better understood for the 10 $\times$ 10 μm element, it was selected for the following TRSKM measurements.

7.4 Unipolar Pulse

Before attempting to switch the element back and forth it is important to understand the dynamics that might be induced by a single electrical pulse. For these measurements the experimental configuration was the same as in chapter 6 (see

section 3.5.2), except that pico-probes were used to connect to the sample instead of wire bonds. Preliminary measurements indicated that a field of 500 Oe in the $\hat{\boldsymbol{x}}$ direction yielded the largest amplitude in-plane dynamics, while static measurements already demonstrated that the sample can be expected to be in a single domain state. Even so, the dynamics induced by the electrical pulse were found to be spatially inhomogeneous. Figure 7.6 shows the dynamics observed at the center, and the top and left edges of the element with a field applied in the $\hat{\boldsymbol{x}}$ direction, and at the center for a 500 Oe field parallel to the $\hat{\boldsymbol{y}}$ direction.

There is a marked difference in the temporal profile of the dynamics at the center and edges of the element, whereby the magnetisation at the center undergoes damped precession while that at the edge undergoes a unipolar deflection. Furthermore the amplitude of each in-plane component depends upon the edge at which it is observed.

Previously in chapter 6, the slow transient response followed the current pulse profile, which was stretched in time due to poor impedance matching. Here, the injected pulse can be expected to largely retain its original shape with full width half maximum of 70 ps, but the observed deflection of the magnetisation appears somewhat slower, perhaps due to dispersion originating from loss in the Si substrate.

To better understand this behaviour, TRSKM images were acquired for $\boldsymbol{H} \parallel \hat{\boldsymbol{x}}$ and $\boldsymbol{H} \parallel \hat{\boldsymbol{y}}$, at the fixed time delay values indicated in figure 7.6, and plotted in figure 7.7. For each magnetisation component the contrast was normalized to the maximum absolute value observed across all time delays.

The vertical banding in the intensity images was the result of a drift in laser power intensity, which was well correlated with the cycle of air conditioning in the lab. The amplitude of this change was 7.5 $\pm$ 2.5 % of the intensity. This was observed during many of the following TRSKM measurements but does not affect the magnetic images, as the optical polarisation bridge detector is immune to variations in laser intensity to first order.

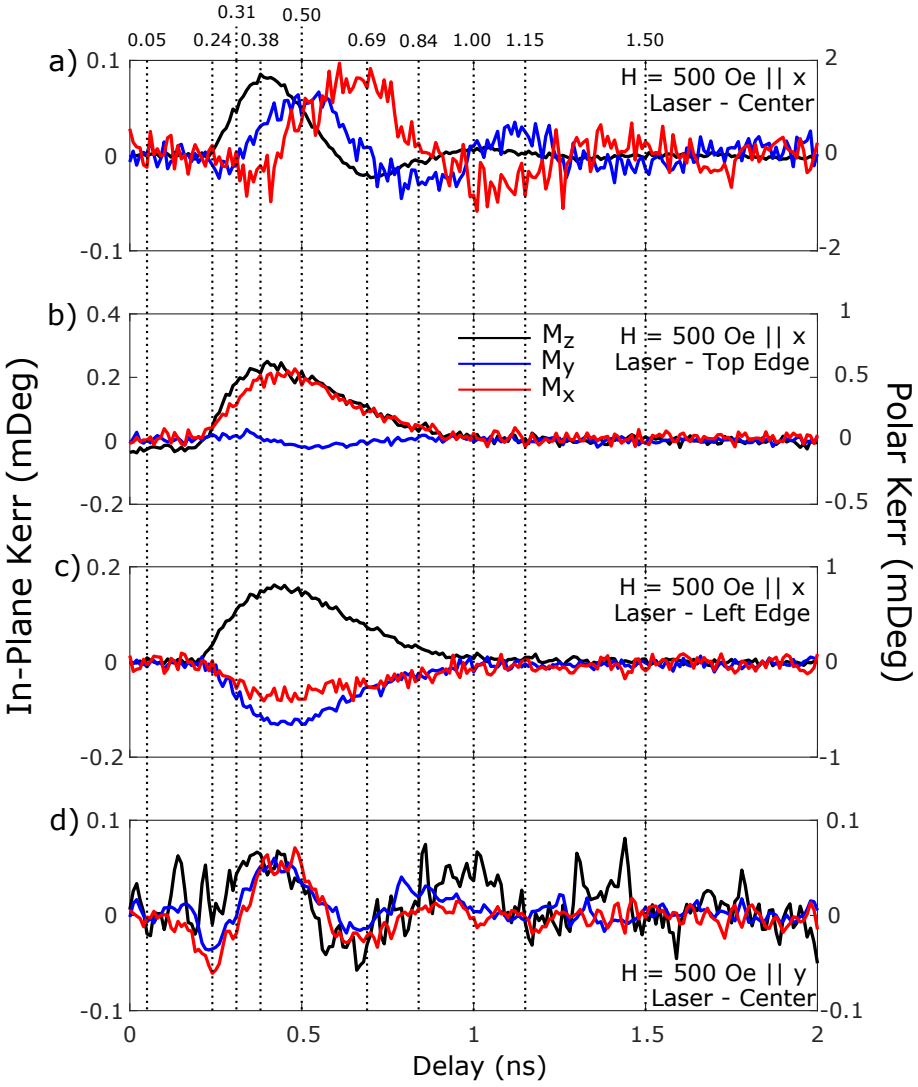

Figure 7.6: Vector TRSKM measurements for the beam positioned at a) the center, b) top edge and c) left edge of the element. With a static field of 500 Oe applied in the $\hat{x}$ direction. For for d the field was applied in the $\hat{y}$ direction with the laser probe at the center of the element. Dashed lines indicate time delays corresponding to TRSKM images in figure 7.7. (Also found in reference [149])

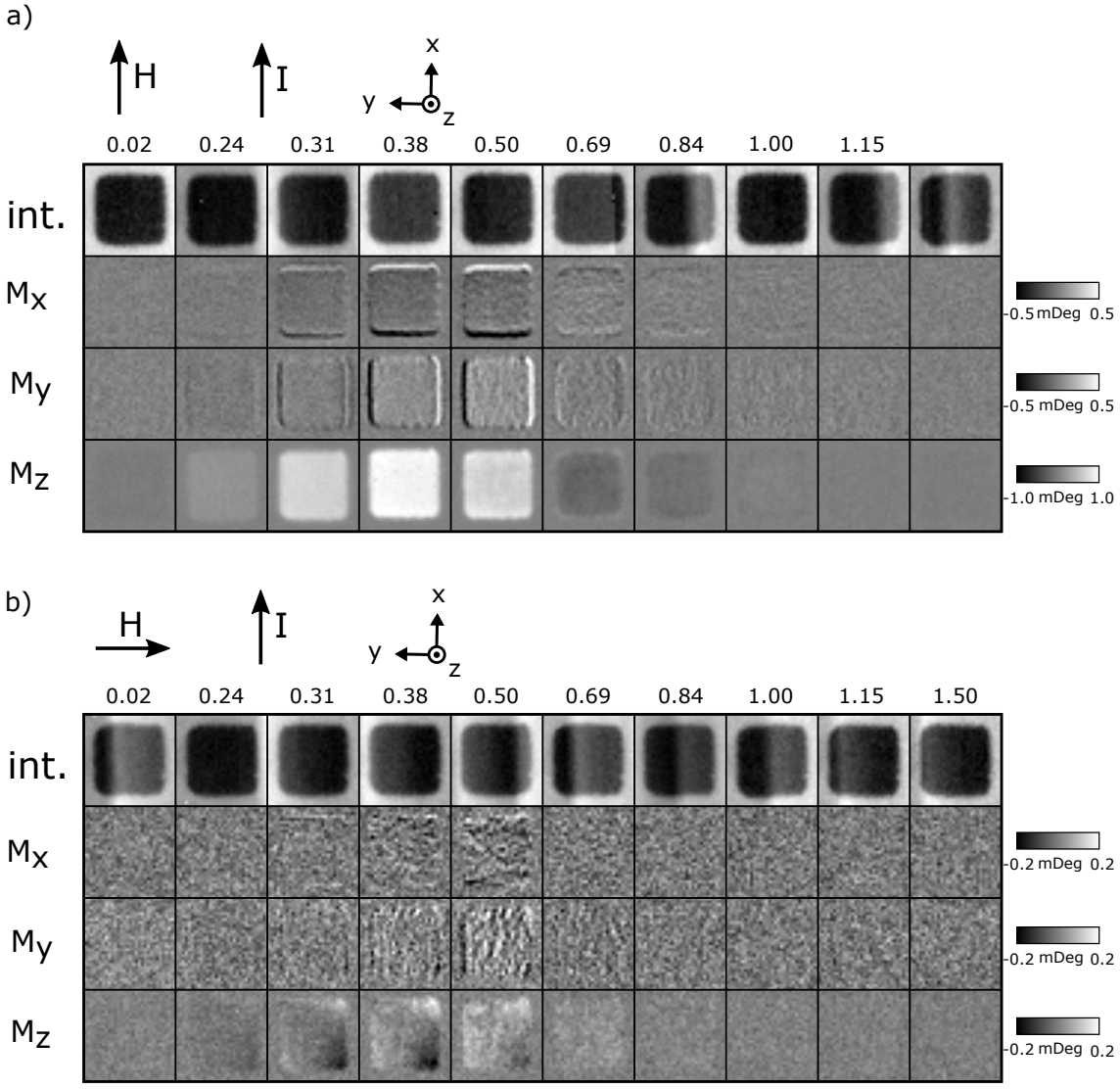

Figure 7.7: TRSKM observations of the dynamics present within 10 $\times$ 10 μm CoFeB elements at the fixed time delays shown (in ns) for a field of 500 Oe applied parallel to a) $\hat{x}$ and b) $\hat{y}$. (Also found in reference [149])

For all regions of the element, the dynamics have a larger amplitude for the field applied parallel to $\hat{\boldsymbol{x}}$ than to $\hat{\boldsymbol{y}}$. Considering first the $\boldsymbol{H} \parallel \hat{\boldsymbol{x}}$ case, the response of M_z appears spatially uniform up to the first maximum at a time delay of $\sim$0.38 ns. Then the sign of the response of the central region reverses, by a time delay of $\sim$0.69 ns, while the edges of the element seem to have relaxed towards the equilibrium orientation. This can be interpreted as the magnetisation initially being deflected away from the plane, with the magnetisation at the center precessing while that at the edges slowly returns to the static orientation.

In comparison, the in-plane dynamics were observed to be spatially non-uniform for all time delays, with the largest amplitude present at the edges. The largest amplitude dynamics occurred at 0.38 ns when both in-plane channels exhibited opposite contrast at opposing edges. At first sight the spatial variation bears some resemblance to the optical artefact discussed in chapter 5. However in the present case this is expected to be genuine magnetic contrast for the following reasons.

In chapter 5 the artefact arose from gold contacts with thickness of 150 nm obstructing the optical probe, while here the height of the elements above the underlayer is significantly smaller ($<$4 nm), so that the shadowing effect should be negligible. To rule out mechanical motion induced by the current passing through the sample in the presence of a static magnetic field, separate TRSKM measurements were carried out at non-magnetic edges (such as the Au/Ta boundary). While contrast was observed, it possessed very different characteristics to that in figure 7.7a. In particular, such contrast was present irrespective of the time delay value, including negative time delay values. The contrast at the non-magnetic edges can likely be attributed a very strong scattering from the highly reflective Au. With non-magnetic origins discounted, the contrast in figure 7.7a can be interpreted as a genuine magneto-optical effect.

It is possible that the magnetic parameters of the material are different at the edges of the device, as a result of the fabrication process. For example, if

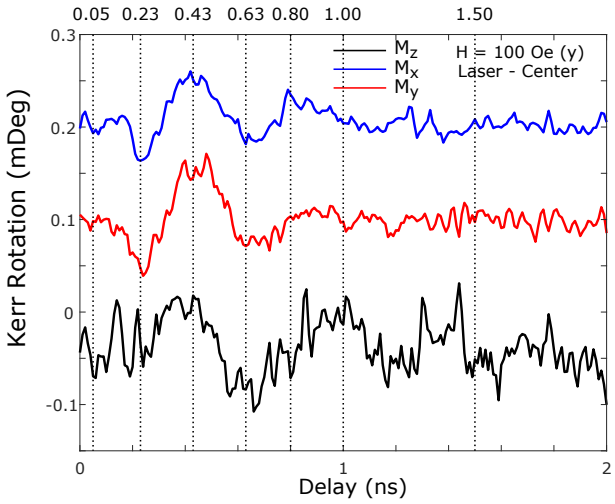

Figure 7.8: TRSKM measurments from the center of the 10 $\times$ 10 μm element for a field of 100 Oe || $\hat{\boldsymbol{y}}$. This measurement was used to identify noteworthy features (dashed lines) for later TRSKM imaging measurements in figure 7.9. (Also found in reference [149])

the PMA is different at the edges, the static magnetisation may have different orientation at the edges and the center of the element. Since the directions of the field-like and anti-damping torques depend upon $\boldsymbol{M}$, non-uniformities of the static magnetisation would result in different torques acting on the magnetisation in different parts of the element. If the center of the sample is saturated in-plane (as suggested by static measurements) a modification of the PMA could be enough to pull the magnetisation out of the sample plane and lead to asymmetric dynamics at the edge. However it was difficult to identify from the static measurements in figure 7.3 whether the magnetisation at the sample edge lies out of the plane.

Figure 7.7b demonstrates that very different dynamics are present for $\boldsymbol{H}$ || $\hat{\boldsymbol{y}}$. In addition to a lower amplitude, the dynamics were more spatially inhomogeneous with opposite polarity of M_z observed at the top and bottom right corners of the element. The in-plane channels instead exhibit an indistinct horizontal (for M_x) and vertical (for M_y) banding. As minimal torque can be expected for $\boldsymbol{M}$ and $\boldsymbol{H}$ || $\hat{\boldsymbol{y}}$, the observed dynamics suggest that the magnetisation was not perfectly parallel to $\hat{\boldsymbol{y}}$ and has some component in another direction.

By reducing the magnitude of the applied field it was possible to observe how

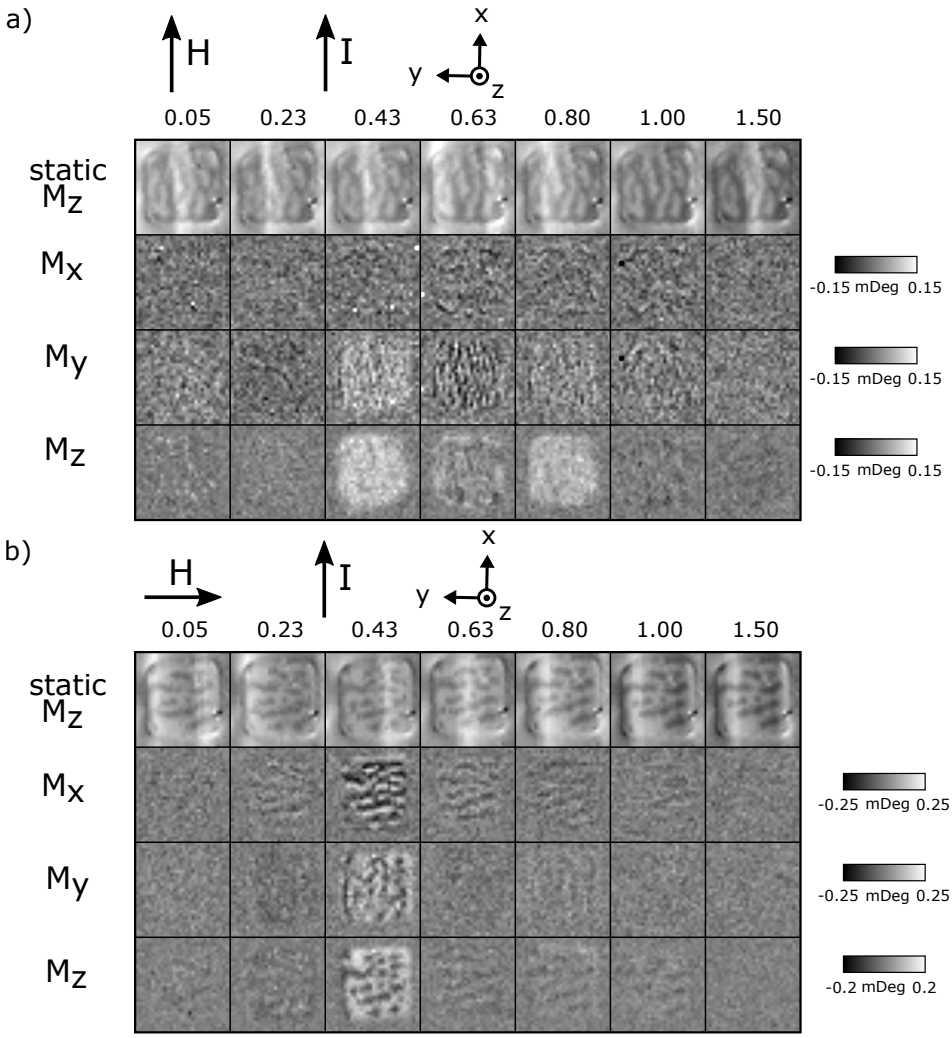

Figure 7.9: Static and dynamic magnetic images of Ta/CoFeB/MgO 10×10 μm elements at the stated delay times (in ns) also indicated in figure 7.8, for a 100 Oe field applied parallel to a) $\hat{x}$ and b) $\hat{y}$. For each time delay, a static polar Kerr image was simultaneously obtained showing the domain structure present during measurement. (Also found in reference [149])

the pulsed current interacts with the domain walls. Dynamics evaluated at a single point on the element for a field of 100 Oe applied parallel to $\hat{y}$ are shown in figure 7.8. While the presence of domains means this measurement is not representative of the entire element it was possible to identify interesting time delays for TRSKM imaging (dashed lines in figure 7.8).

The dynamics excited by the same unipolar pulse are shown in figure 7.9 for a field of 100 Oe applied parallel to $\hat{x}$ and then to $\hat{y}$. The equilibrium state, reached after a large number of electrical pulses, was measured simultaneously revealing

a domain state. Interestingly, the equilibrium states present in figures 7.9a and b are different from each other and from those observed earlier in figure 7.3. The domains observed in the absence of current exhibit a diagonal orientation from the top right to the bottom left corners of the element, whereas the injection of spin current enables the domains to re-orientate to lie parallel to the applied field.

Section 2.4 discussed the structure of domain walls within materials with PMA. For thin films, the Bloch wall represents the lowest energy structure. However, as the film thickness increases so too does the stray field, leading to an in-plane canting of the magnetisation. At the upper and lower sample surfaces, these 'twisted' domain walls can form Néel walls of opposite in-plane orientation. While this remains an active area of research, minimal domain wall twisting is expected in the present case due to the ultrathin nature of the CoFeB layer. As a result, Bloch walls are expected to be present in the long edges of the domains in figure 7.9, whereby the magnetisation within the wall lies parallel to the static field for both $\boldsymbol{H}$ || $\hat{\boldsymbol{x}}$ and $\hat{\boldsymbol{y}}$ directions. For the short domain edges (i.e. the walls orthogonal to the static field) it is not clear if Néel or Bloch walls are preferred (or some intermediate orientation). Further work is required to understand the static state, which will aid interpretation of the magnetisation dynamics.

There has been debate as to the role of the Dzyaloshinskii–Moriya interaction (DMI)[150,151] within CoFeB/Ta systems.[140] The presence of DMI in these systems would reduce the energy of domain walls of one chirality, potentially leading to the formation of Néel walls in thin films.[103] While still an active area of research, measurements of domain wall velocity (driven by spin currents) suggest that the DMI is not significant.[141] Furthermore, recent Magnetic Force Microscopy measurements of the stray field indicate the presence of Bloch walls,[22,142] with minimal twisting. As a result, the presence of Bloch walls can be expected in the present case. Given that the long edges of the domains lie parallel to field, the magnetisation within the wall is likely to lie in this direction also.

	$\hat{\boldsymbol{m}}$	$\hat{\boldsymbol{y}}$	$\hat{\boldsymbol{m}} \times \hat{\boldsymbol{y}}$	$\hat{\boldsymbol{m}} \times (\hat{\boldsymbol{m}} \times \hat{\boldsymbol{y}})$
$\boldsymbol{H} \parallel \hat{\boldsymbol{x}}$	$[1/2 \quad 0 \quad \sqrt{3}/2]$	$[0\ 1\ 0]$	$[-\sqrt{3}/2 \quad 0 \quad 1/2]$	$[0 \quad -1 \quad 0]$
$\boldsymbol{H} \parallel \hat{\boldsymbol{x}}$	$[1/2 \quad 0 \quad -\sqrt{3}/2]$	$[0\ 1\ 0]$	$[\sqrt{3}/2 \quad 0 \quad 1/2]$	$[0 \quad -1 \quad 0]$
$\boldsymbol{H} \parallel \hat{\boldsymbol{y}}$	$[0 \quad 1/2 \quad \sqrt{3}/2]$	$[0\ 1\ 0]$	$[-\sqrt{3}/2 \quad 0 \quad 0]$	$[0 \quad -3/4 \quad \sqrt{3}/4]$
$\boldsymbol{H} \parallel \hat{\boldsymbol{y}}$	$[0 \quad 1/2 \quad -\sqrt{3}/2]$	$[0\ 1\ 0]$	$[-\sqrt{3}/2 \quad 0 \quad 0]$	$[0 \quad -3/4 \quad -\sqrt{3}/4]$

Table 7.1: Orientation of initial field-like and anti-damping torques for representative values of $\hat{\boldsymbol{m}}$ (canted 30° from $\hat{\boldsymbol{z}}$), when a small static field is applied parallel the $\hat{\boldsymbol{x}}$ and $\hat{\boldsymbol{y}}$ directions. (Adjusted from reference [149])

In contrast to the observations at H = 500 Oe, the amplitude of dynamics at H = 100 Oe is largest for $\boldsymbol{H} \parallel \hat{\boldsymbol{y}}$. For $\boldsymbol{H} \parallel \hat{\boldsymbol{x}}$, spatially uniform dynamics are observed despite a non-uniform static magnetisation, as can be seen in figure 7.9a for delays of 0.43-0.80 ns. To drive uniform precession across in this way, the out of plane torque must have the same polarity for both types of domains. Table 7.1 calculates the orientation of field-like and anti-damping torques for a selected orientation of $\hat{\boldsymbol{m}}$ analogous to the canted magnetisation present in each type of domain in figure 7.9, figure 7.10 represents these values schematically. From this, it can be seen that the field-like torque has orientation out of the sample plane regardless of the domain polarity. As chapter 6 established the field-like STT to be negligible, the out of plane dynamics can be attributed to the pulsed Oersted field (which in effect also follows $\hat{\boldsymbol{m}} \times \hat{\boldsymbol{y}}$).

However, for $\boldsymbol{H} \parallel \hat{\boldsymbol{y}}$ the observed dynamics appear to be closely correlated with the domain structure present. To demonstrate this, in figure 7.11 the TRSKM images that exhibit the strongest contrast (0.43 ns) are shown with the static domain structure overlaid (red curves) for $\boldsymbol{H} \parallel \hat{\boldsymbol{x}}$ and $\boldsymbol{H} \parallel \hat{\boldsymbol{y}}$.

For $\boldsymbol{H} \parallel \hat{\boldsymbol{y}}$, the dynamics can clearly be associated with the domain walls within the element. The highlighting reveals that the static M_z state corresponds directly to the contrast in the image of the M_z dynamics. This can be understood by considering the anti-damping torque for this geometry, as in table 7.1. For this geometry, the anti-damping STT is the only member of the table to possess a component which changes sign with domain polarity. As a result, the domain

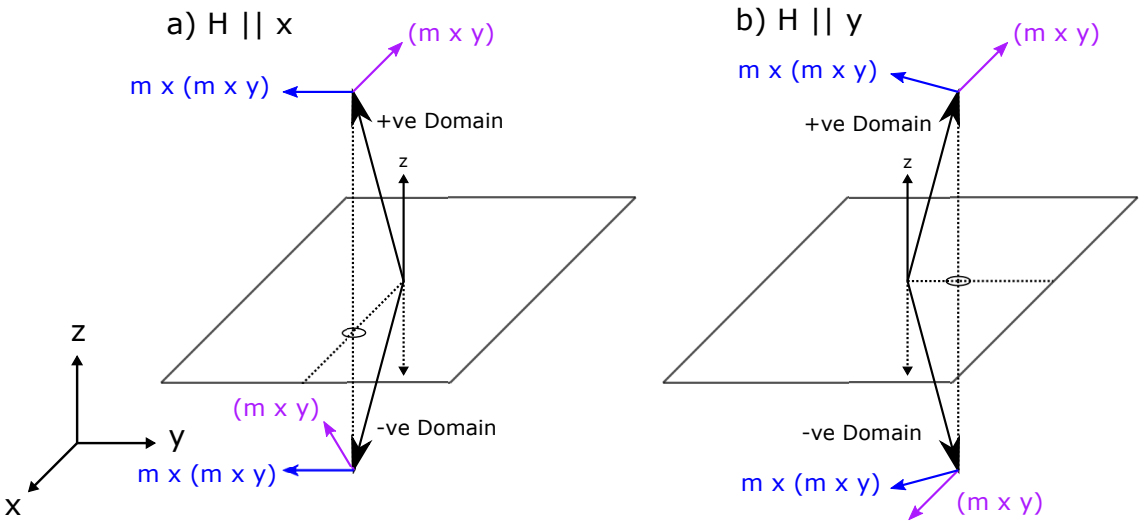

Figure 7.10: Schematic representation of torques calculated within table 7.1.

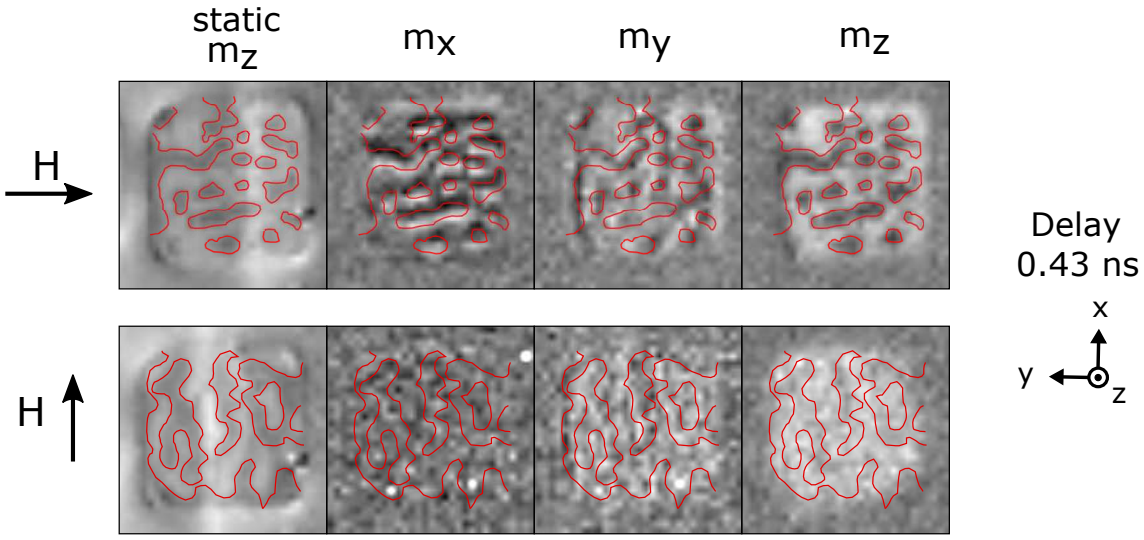

Figure 7.11: TRSKM measurements at a time delay of 0.43 ns, from figure 7.11, for $\boldsymbol{H} \parallel \hat{x}$ & $\hat{y}$. The static domain structure is highlighted in red within all images. (Also found in reference [149])

pattern observed in the dynamic M_z of figure 7.11 must be due to injected spin current. This structure persists to a time delay of 1 ns. Figure 7.9 shows that all three magnetisation components exhibit small amplitude oscillations. This is most evident in the M_z images at 0.43 $\rightarrow$ 0.80 ns time delay values.

In contrast, when the field was applied parallel to the $\hat{\boldsymbol{x}}$ direction, no correlation was observed between the domain structure and the M_z dynamics. Table 7.1 indicates that only the field-like torque acts in the positive $\hat{z}$ direction, regardless of domain polarity. However, as observed in chapter 6, the magnitude of the anti-damping torque is much larger than that of the Oersted field torque. So in order for the Oersted field to describe the M_z dynamics, $\boldsymbol{M}$ must lie exactly within the xz plane where the anti-damping torque vanishes. Furthermore, this configuration exhibits oscillations of the M_z and M_y components, which appear to be in phase and spatially uniform.

The dynamics of the in-plane magnetisation components are more complicated to interpret. For $\boldsymbol{H} \parallel \hat{\boldsymbol{y}}$ the regions of largest amplitude response are centred on the domain walls, with opposite polarity for walls on opposite sides of a particular domain. Furthermore, the dynamic m_x component has largest amplitude along the long edges of the domain while the dynamic m_y component has greatest amplitude along the short edges. Given that the magnetisation within the domain wall at the long edges lies in the $\hat{\boldsymbol{y}}$ direction, the field-like and anti-damping torques acting on the magnetisation within the wall should vanish. This in-plane contrast oscillates with time, as can be seen from delays 0.23 $\rightarrow$ 0.63 and from figure 7.8.

The same is not true for $\boldsymbol{H} \parallel \hat{\boldsymbol{x}}$, where the dynamics in m_x and m_y are not strongly correlated with the domain structure. Although the magnetisation within walls at the long edge of the domains is expected to lie in the $\hat{\boldsymbol{x}}$ direction (where spin torques are maximized), no significant dynamics are observed. The suppression of dynamics and lack of correlation with the domain structure is at odds with the expected torques, and requires further work in order to be understood.

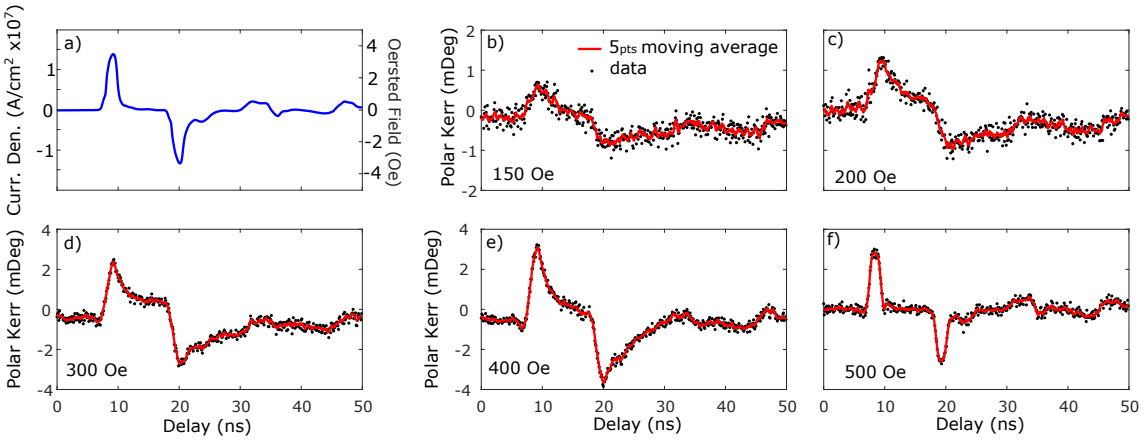

Figure 7.12: a) Electrical pulse profile determined by measurement of the transmitted pulse, with calculated current density and Oersted field. The resulting magnetisation dynamics were measured for static fields of b) 150 Oe, c) 200 Oe, d) 300 Oe, e) 400 Oe, f) 500 Oe applied in the $\hat{x}$ direction.

7.5 Bi-polar pulse

Since magnetisation reversal has been demonstrated in Hall bars in response to a continuous DC current, switching should also be possible in response to pulsed currents of appropriate amplitude and duration. To observe such switching in TRSKM it is necessary to supply both a 'write' and a 'reset' pulse to the sample, as described in section 3.5.2. Stochastic domain wall processes have repeatedly been demonstrated to play a role in magnetisation reversal.[125,137,140,147,152] However as TRSKM measurements probe dynamics averaged over many cycles, stochastic reversal processes cannot be observed reliably. Instead, such measurements should yield average switching times.

Figure 7.12a shows the bi-polar electrical pulse used to stimulate the sample, expressed in terms of the calculated current density and Oersted field. The 'write' and 'reset' pulses feature rise times of 2.519 ns and 2.59 ns with FWHM of 1.855 ns and 2.0 ns respectively. The 'reset' pulse peaks at 96% of the 'write' pulse peak amplitude and is delayed by 11.0 ns (pulse separation was limited by the total length of cable available). In addition to the two main pulses, low amplitude peaks can be observed at a later time delay, caused by reflections within the electrical

cables and components.

The dynamics induced by the bi-polar pulse are presented in figures 7.12b-f, for increasing values of magnetic field applied in the $\hat{\boldsymbol{x}}$ direction. For these measurements the optical probe was positioned at the center of the 10 μm square element. Little response was observed for fields below 150 Oe, which could be due to the presence of domains through which the signal spatially averages out to zero. For $\boldsymbol{H}$ = 150-200 Oe the magnetisation is deflected in response to the both the 'write' and 'reset' pulses, whereby an initial positive deflection is followed $\sim$10 ns later by a negative deflection. Between these pulses the magnetisation slowly relaxes towards its original orientation.

For a bias field of 300 Oe the bi-polar pulse drives a switching-like behaviour. The 'write' pulse drives a large out-of-plane deflection,after which the magnetisation appears to relax to a meta-stable intermediate state. The magnetisation appears to follow the profile of the 'reset' pulse, but is slower to relax to the original state at negative time delay. Further increasing the field to 400 Oe, relaxation after the 'write' pulse is more gradual and it is unclear whether this leads to a meta-stable state. At 500 Oe the magnetisation closely follows the bi-polar pulse.

In order to gain further insight, preliminary simulations of the magnetisation dynamics were carried out using the macrospin model detailed in chapter 6. Assuming the form of the current profile in figure 7.12a and employing the same or similar parameters to those used in chapter 6, the magnetisation closely follows the profile of the current pulse. In the experiment this behaviour is only observed for a field of 500 Oe, where lower fields exhibit a slow relaxation or meta-stable state. By fine tuning the simulation parameters, it was possible to obtain dynamics that resemble those observed experimentally. While the parameters used for this simulation are not considered to be realistic for this sample, the simulated dynamics can be used to interpret those observed in the experiment. Figure 7.13a shows the hysteresis loop calculated for the modified values, where two stable states are present for values of H up to 1400 Oe. Figure 7.13b shows the response of

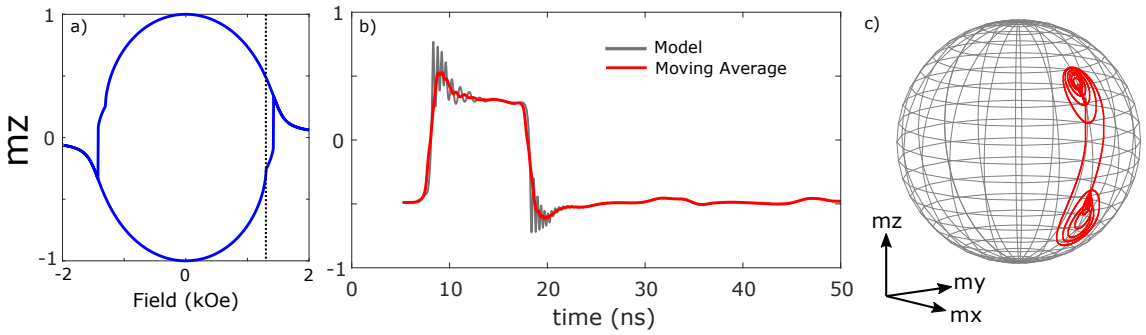

Figure 7.13: Simulations to replicate meta-stable state behaviour, assuming K_1=7.0×10^6 erg/cm^3, K_2=1×10^4 erg/cm^3 for H = 1.3 kOe applied parallel to the the $\hat{x}$ direction. a) hysteresis loop with dashed line to indicate 1.3 kOe, b) change of m_z in response to bi-polar pulse of twice the amplitude in figure 7.12a. The gray line shows the full time-dependant response, with the red line showing a moving average, c) dynamic response projected onto a sphere.

the magnetisation to a bi-polar pulse with twice the amplitude of that used in the experiment, where a meta-stable state similar to that observed in the experiment can be achieved. The full magnetisation trajectory can be projected onto a sphere as shown in figure 7.13c.

Comparing the calculated and experimental meta-stable states, the most noticeable difference is the value of m_z before and after the 'reset' pulse. This measured metastable signal level in figure 7.12d is 1 mDeg, which from comparison with the hysteresis loops in figure 7.4 equates to a Δm_z of $\sim$0.01. In comparison, the calculated states are separated by $\Delta m_z \simeq$0.7. Furthermore, the field and pulse amplitudes are larger than those required in the experiment. Hence the calculation should be used for illustrative purposes only.

In response to the 'write' pulse, the magnetisation switches from its initial state and undergoes precession as it settles into the meta-stable state. The meta-stable state arises from the fact that the sample is not saturated fully in-plane and hence has two stable orientations with m_z values of opposite sign. However, since there is small but finite canting of the static field relative to the sample plane, the small field component in the $\hat{z}$ direction defines a preference for one of these states. In the absence of a 'reset' pulse the magnetisation will eventually switch back to

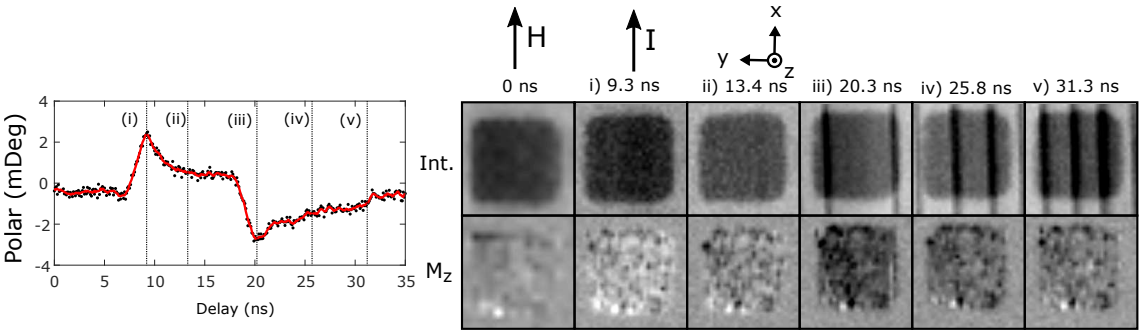

Figure 7.14: TRSKM images of the out-of-plane dynamics within the 10 μm element for a field of 300 Oe applied in the $\hat{x}$ direction.

it's original orientation.An additional feature of the experiment not observed in the simulation is the slow relaxation following the 'reset' pulse. This may be due to the nucleation of domains in the absence of current, with width below the resolution of the TRSKM.

TRSKM images of the meta-stable state are shown in figure 7.14. With the laser operating at a reduced intensity (due to the pulse-picker) and the intensity banding noted previously it is difficult to observe any particular spatial structure to the dynamics. However, by drawing comparison with the images from the uni-polar pulse for this field orientation (figures 7.7a and 7.9a) the dynamics are either spatially uniform across the element or the structure cannot be resolved by the optical probe. This can perhaps be seen most clearly in the 9.3 ns and 20.3 ns time delay images, where the entire element under goes a transition from 'light' to 'dark', albeit with some fine scale structure that is not properly resolved.

The response of smaller elements to the bi-polar pulse was also tested, plotted in figure 7.15. It was hoped that the reduced domain structure would improve the likelihood of coherent rotation, and that a larger signal could be obtained in the event of switching if a reduced field was used. While a slightly increased signal amplitude was observed for the smaller elements there was no evidence of switching to the meta-stable state.

While the experiments presented here revealed switching to a meta-stable state under restricted conditions they do highlight important factors that may hin-

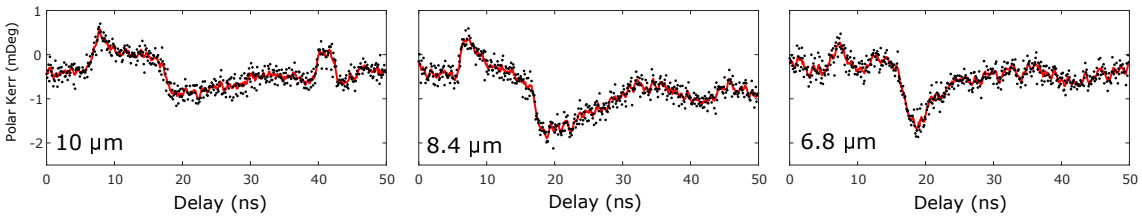

Figure 7.15: Polar MOKE signals acquired from elements of different size in response to the bi-polar pulse, with a static field of 150 Oe applied parallel to $\hat{x}$, and with the optical probe in the center of each element.

der the observation of ultra-fast switching. While an increased static magnetic field strength should lead to lower write currents, smaller MOKE (and electrical) signals are generated due to the reduced out of plane magnetisation component. Imperfect alignment of a large in-plane field will lead to an out of plane component that can reduce the stability of the switched state. However, reducing the field amplitude introduces domains within larger elements. Therefore future measurements should consider elements that are smaller and ideally support a single domain state.

7.6 XPEEM measurements

7.6.1 Motivation

The presence of domains within the CoFeB elements has been clearly demonstrated by static and time-resolved scanning Kerr microscopy. While the presence of domains is expected to lower the required 'write' current the switching process is not strictly repeatable. Furthermore, with the continuous miniaturization of technology realistic memory elements can be expected to be sufficiently small as to exist in a single domain state. While Kerr microscopy measurements suggest that the transition from multi-domain to single-domain elements takes place at $\sim$2 μm, this length scale is comparable to the optical resolution (870 nm).

A better understanding of domain formation within both large and small el-

ements would both assist the interpretation of existing TRSKM data and help identify new routes for current induced switching in future measurements.

In order to achieve this and overcome the spatial limitations of TRSKM, XPEEM measurements were performed to investigate the ground state present in the CoFeB square elements. The theory and methodology of these measurements are outlined in section 3.7. While these measurements will consider field driven reversal as opposed to current induced switching, similar domain processes can be expected for both cases. One of the key advantages of using XPEEM is that it is element specific, allowing the Fe and Co constituents to be probed separately beneath the Ta and MgO layers.

For these measurements two wafers were prepared. While the sample used previously in this chapter was preserved for future measurements (as XPEEM can be destructive to the sample), two nominally identical wafers were selected with both a high and low ρ Si substrate. In separate measurements, the high ρ wafers had proven unsuitable for TRSKM measurements due to their low Kerr rotation, hence they were considered for XPEEM instead. All samples measured had a nominally identical stack structure and patterned elements to that used for TRSKM measurements.

7.6.2 Results

High Resistivity Si Wafer

This sample was near identical to that used to obtain MOKE hysteresis loops and domain images previously, and as such was expected to show similar magnetic structure. To probe the domain state the wafer was placed on a sample cartridge with an integrated in-plane electromagnet.

However the resistivity of the substrate caused difficulties in the XPEEM measurement. Due to the limited conductance of the surface of the wafer, a 6 nm film of Al was deposited by sputtering to prevent charging. While it was possible to

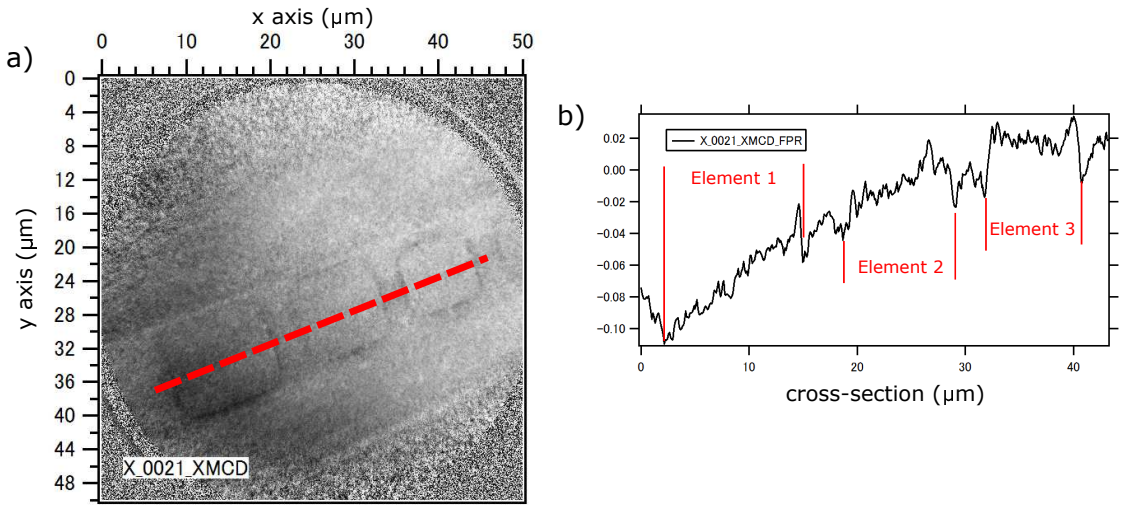

Figure 7.16: XPEEM data from samples grown on a high resistivity Si wafer. a) Difference of images acquired at x-ray energies of 700 eV and 707 eV. Square elements can be seen at the edge of a gold track b) cross-section taken along the long red line in a.

image the large gold tracks on the device, the elements showed substantially less contrast. The X-ray energy was scanned across the Co and Fe L_{III} edges but there was no clear sign of these materials in the recorded spectrum. In order to identify their presence a subtraction was performed between two images acquired on and off the Fe L_{III} edge (at 707 eV and 700 eV respectively). The result is plotted in figure 7.16a, with a cross-section taken and plotted in figure 7.16b. Despite having identified the square elements, the emission was too weak to deduce any magnetic information about the CoFeB layer.

Low resistivity Si Wafer

To overcome the charging problem, the sample grown on low ρ Si was mounted as before on the cartridge with an integrated in-plane electromagnet. The resistance across the upper surface of this sample was measured to be of the order $10^6\Omega$, which is sufficient to ground the sample and allow for X-ray absorption measurements to be carried out without the need for Al sputtering. It should be noted that charging was not fully eliminated and so measurements were carried out at a low

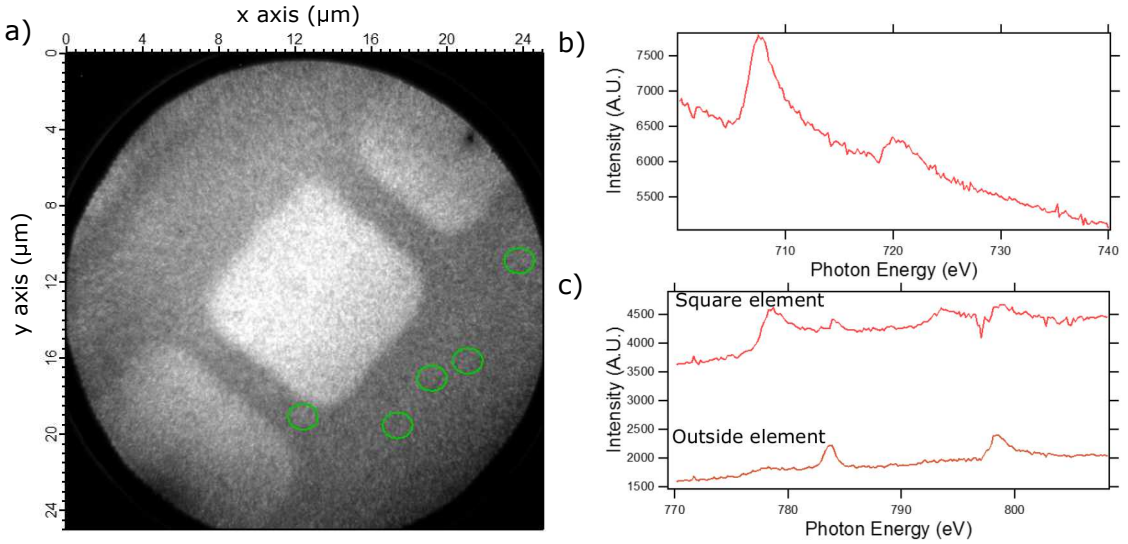

Figure 7.17: Data obtained from the sample grown on a low resistivity Si wafer. a) image at 707 eV depicting square elements. X-ray absorption spectrum at b) the Fe edge and c) Co edge (for two regions, inside the square element and from the circled regions in a. Spectra were obtained from the 8.4 μm square element.

X-ray intensity. Nevertheless the square elements could be clearly seen above background levels, as shown in figure 7.17a.

With the elements clearly visible, the X-ray energy could be varied to observe the chemical composition and estimate the XPEEM signal strength. Figure 7.17b shows the electron emission for X-ray energies near the Fe edge. A peak is clearly visible at ~707 eV representing the Fe L_{III} edge with a smaller peak at ~721 eV corresponding to the Fe L_{II} edge. The energy was increased to scan over the Co edge as shown in figure 7.17c. Here a peak at ~779 eV represents the expected Co L_{III} edge. However the images acquired at higher X-ray energy revealed some small regions outside the square elements that possess a different spectrum. Regions indicated by the green circles in figure 7.17a exhibit the spectrum shown by the lower line in figure 7.17c. The energies of ~784 eV and ~798 eV are close to but different from the Co L_{III} and L_{II} edges respectively. Since these peaks also appear within the spectrum for the square elements, they are likely due to contamination introduced during fabrication (Barium, Antimony and Tellurium all have absorption peaks near these energies but are not expected to be involved

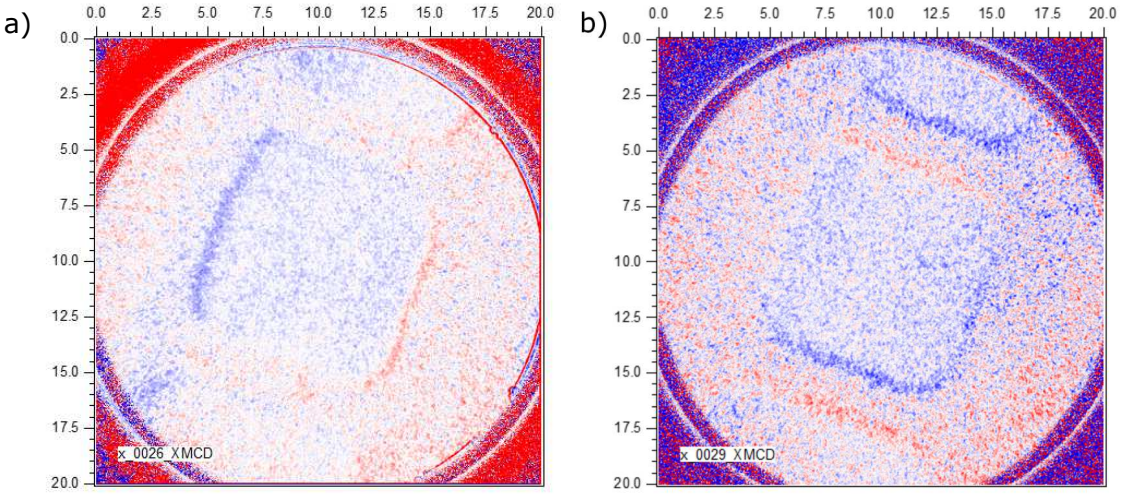

Figure 7.18: Preliminary XMCD images with 1 s exposure at the a) Co L_{III} b) Fe L_{III} edges. X-rays at normal incidence, sensitive to the out of plane magnetisation. Measurements for the 8.4 μm square element.

in any fabrication steps). Within these spectra the Fe peak has an edge jump of $\sim$17% while the Co has an edge jump of $\sim$25%. These small values for the edge jump suggest the weak signal from the 1 nm CoFeB layer is attenuated by the MgO and Ta capping layers. Assuming the smaller specks outside the elements are associated with pure Co, they show a larger edge jump than the elements at $\sim$30%, again suggesting that the MgO and Ta capping layers are interfering with the measurement of the patterned elements.

Despite the low edge jump, XPEEM measurements were carried out to identify any magnetic domains present in the square elements. Figure 7.18 shows preliminary XPEEM images at both the Co and Fe L_{III} edges with a 1 s exposure time. The contrast observed on opposite sides of each element is on the scale of the background noise, and is therefore likely due to sample drift between measurements and is not magnetic in nature. The contrast in the centre of the disk appears to be uniform in both Co and Fe images, suggesting a uniform domain state. However this is roughly at the level of the noise and so further averaging/exposure is required.

The noise seen in the preliminary measurements was then reduced by increas-

ing the exposure time to 5 s. Figures 7.19 a & b show the same square element over the Fe edge. With the sample now settled there is no sign of opposite contrast at opposite edges, instead the uniform contrast in the XPEEM image shows the element to be in a single domain state. Even after applying and removing an in-plane field of 165 Oe this state persisted. This result is surprising, since the only difference between samples studied in figures 7.3 and 7.19c is the resistivity of the substrate, which is not expected to impact the magnetic state. Similar measurements over the Co L_{III} edge yielded the same results.

Smaller elements were then tested to see whether they also contained only a single domain, as shown in figures 7.19 c & d. It can be seen that fabrication artefacts (due to the resolution of photo-lithography) arose at these length scales, which would be difficult to observe in an optical microscope. Regardless of the element shape and size they all possess a single domain state. These images show the elements with size 3.6 μm - 2.0 μm, hence the smallest elements in figure 7.5 can treated as circular perhaps with residual photoresist remaining at the centre.

After acquisition of the images, a spectrum was obtained at the Fe L_{III} edge. Through comparison with figure 7.17b it was confirmed that no degradation of the sample had taken place during measurements.

7.6.3 Discussion

The observed signal at the Fe L_{III} edge arises from the preferential absorption of X-rays of a certain helicity. The fact that any signal is observed implies that the CoFeB layer has finite magnetisation. The domain structure expected from previous measurements should provide clear contrast. since no identifiable out of plane structure could be observed the elements must be in a uniform state of magnetisation.

While it is conceivable that the magnetisation lies in-plane, to give rise to the

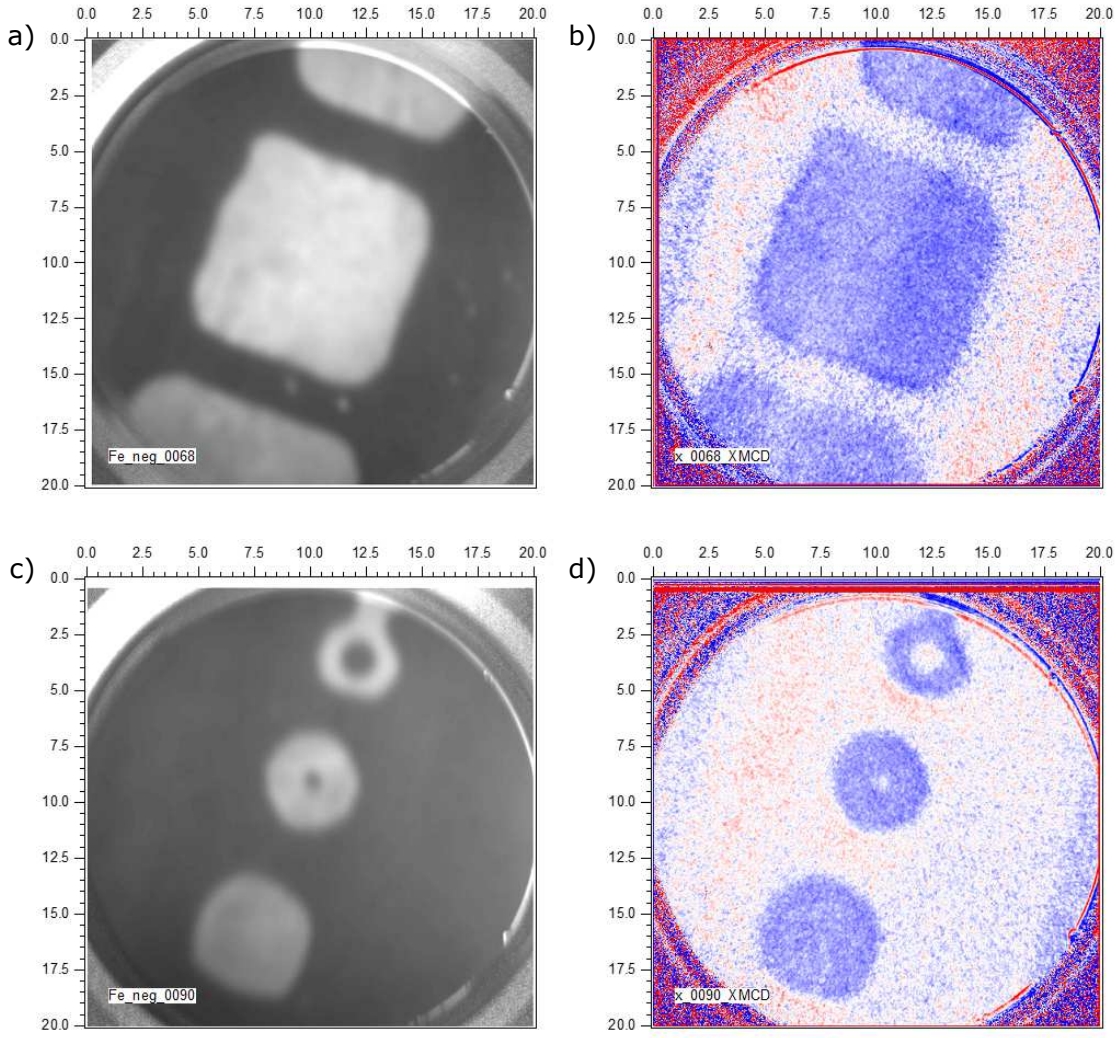

Figure 7.19: XPEEM images aquired at the Fe L_{III} edge with a 5 s exposure time. a) X-ray absorption image of larger square element with b) showing the corresponding XMCD image. c) X-ray absorption image of smaller elements and d) the corresponding XMCD image.

observed contrast the magnetisation would need to cant out of the sample plane while existing in a single domain state. It is more likely that the sample is in a uniform out-of plane state, with much of the already weak XPEEM signal lost in the MgO and Ta capping layers.

However if the magnetic contrast is genuine it should be possible to switch the magnetisation between out-of-plane states of different polarity. Despite sweeping an in-plane magnetic field to positive and negative 165 Oe (parallel to the direction of elements), the magnetic state could not be changed, despite the fact that the applied field was greater than both the in-plane and out of plane coercivity. Again it is possible that a combination of remanent magnetisation and sample tilt could repeatedly set the same state. To test this it would be necessary to apply a large out of plane field. However it was not possible to do this with the sample cartridges available.

While the observation of uniform magnetisation was not expected, it is still encouraging for future TRSKM measurements. Samples with a uniform state should exhibit repeatable and coherent switching, that should yield a stronger signal in TRSKM measurements.

7.7 Summary

The suitability of Ta/CoFeB/MgO/Ta elements for MRAM applications has been explored using a variety of methods. While static electrical measurements in these systems are well reported in the existing literature, this chapter has employed ultra-fast excitation and both spatially and time resolved measurements.

The primary tool has been scanning Kerr microscopy, in both static and ultra-fast time-resolved configurations. During these studies magnetic domains were observed to not only be present but to also impact the magnetisation dynamics. With a saturating field of 500 Oe parallel to the direction of current, qualitatively different behaviour can be observed between the edges and center of the square

elements. In response to a fast electrical pulse the center of the elements undergoes damped precession, whereas the magnetisation at the edges is simply deflected and returns gradually to equilibrium. With the bias field applied orthogonal to the current direction, lower amplitude dynamics are observed but again with greatest amplitude close to the edges. This may be evidence of different PMA at the edges, that also accounts for domain formation at the sample edges observed in static measurements.

A different behaviour entirely is observed for lower field amplitudes, revealing the formation of domains. For static field parallel to the pulsed current direction uniform precession is observed. However, for an orthogonal field the pulse drives motion of the domains themselves. The polar magnetisation can be understood by considering the geometry of the torques present, while accounting for the canting of the magnetisation within domains of each polarity. Repeated pulses also reorientate the domains to align parallel to the applied field, which is different to the structure observed with magnetic field alone.

When a bi-polar pulse is used to 'write' and 'reset' an element's magnetic state it is possible to induce a metastable state. This behaviour is analogous to the coherent switching expected, however an out-of-plane component of bias field is usually present that reduces the stability of this state. Hence, in the absence of a 'reset' pulse the magnetisation still relaxes to its original orientation. This can be alleviated by using lower field amplitudes and smaller elements that should occupy a single domain state.

To overcome the limited spatial resolution of TRSKM, XPEEM measurements were employed to better understand the ground state. However these measurements were performed on a different wafer which surprisingly showed that all elements were in a single domain state. While a lower Kerr rotation signal could be expected, these samples instead may provide a better route to observing ultrafast coherent switching.

CHAPTER 8

Summary and Future Work

This thesis presents the results of high frequency electrical and magneto-optical experimentation. The time-dependent behaviour of a number of thin film devices and structures was investigated in time-resolved scanning Kerr microscopy (TRSKM) experiments. These so-called pump-probe experiments induce dynamics by applying an electrical signal (pump) and subsequently measure the magneto-optical Kerr effect (MOKE) with an optical probe. By utilizing the longitudinal Kerr effect it was possible to measure in-plane components of magnetisation. The electrical pump took various forms depending on the dynamics of interest. By exploiting the Spin Hall effect (SHE) and Rashba effect (RE) a spin current could be generated with retaining the same temporal form as the injected current pulse.

In addition to these experiments, a number of simulation and analytical methods have been employed throughout. COMSOL simulations in SHNOs allowed the DC charge current and Oersted field to be calculated. These were subsequently imported to MuMax3 micromagnetic simulations to predict the expected dynamics. In contrast, a macrospin model was employed to aid the understanding of torques present in CoFeB structures.

The devices selected for study here possess a number of desirable attributes within their field of application. The highly tunable GHz emission present in Py/Pt

bilayer SHNOs makes them attractive as oscillators for communications and computing. In contrast, the perpendicular magnetic anisotropy in Ta/CoFeB/MgO would give MRAM memory elements high stability and low write currents. Both these device architectures exhibit a planar geometry and allow for easy optical access with the TRSKM.

Chapter 4 introduced the SHNO considered within this thesis. Finite element simulations of DC current profile demonstrated that the structure is designed to focus the charge current within a concentrated region of the Pt layer, whereby the SHE subsequently generates a pure spin current into a magnetic Py layer. By injecting an RF current, spin transfer torque ferromagnetic resonance (STT-FMR) was used to measure a spatial average of the torques from ferromagnetic resonance curves. The theory used to understand the electrical resonance curves has been employed to interpret similar resonance curves measured by TRSKM. Among other advantages, this approach allows local torques to be probed within the Py layer. In contrast to predictions from finite element simulations, the torques from anti-damping STT and Oersted field extend further into the Py disk. This spreading of the RF current arises from the self-inductance of the device geometry. Such effects are well understood in coplanar waveguides (CPWs) but have not been considered or explored within spintronic devices of the kind considered here.

Chapter 5 described a progression of the work in chapter 4, whereby an additional DC current was used to drive spin wave excitation. This spin wave has been dubbed the spin wave 'bullet' due to its self-localization and non-linearity. Synchronization of the bullet to the TRSKM can be achieved by injecting RF of a similar frequency. However, as this frequency was close to that of the FMR, TRSKM observations demonstrated that the SHNO supports both the bullet and FMR modes in superposition. After accounting for this, an increased DC current leads to reduced localization of the bullet. Micromagnetic modelling demonstrated that, in the absence of a pinning site, the 'bullet' is highly mobile within the central region of the disk. Given that the injected RF current generates a modified torque

distribution within the Py layer, the reduced localization can be interpreted as the 'bullet' undergoing additional translational motion.

Chapter 6 was devoted to understanding the dynamics observed in Ta/CoFeB/MgO Hall bars, whereby the injection of an electrical pulse drove precession of the magnetisation upon a slow transient background. A macrospin model considering a second order PMA term and anti-damping STT was found to replicate much of the static and dynamic behaviour. Extrapolating this model to larger current pulse values yielded improved conditions for switching.

Elements patterned from Ta/CoFeB/MgO were studied with TRSKM and XPEEM in chapter 7, in order to better understand the fast switching processes. Static Kerr microscopy measurements showed the presence of domains for fields less than 300 Oe. For unipolar electrical pulses, spatially asymmetric dynamics were found at the sample edges and domain walls. When applying a bipolar pulse the element was found to enter a metastable state for a field of 300 Oe. By comparison with a macrospin model, the reduced stability arises from an out of plane field component setting a preferred orientation of the magnetisation. XPEEM measurements of a nominally identical sample yielded different static magnetisation behaviour that requires further work to explain.

The continuation of this work may take multiple forms. In regard to oscillators, the observed spreading of the high-frequency RF current is of immediate interest. One proposed mechanism for mutual synchronization of spintronic oscillators is to utilize the RF current emission. Such emission can undergo current spreading, which could serve to either enhance or diminish this synchronization. Furthermore, the de-localization of the bullet mode suggest studies of structures where its motion within a magnetic layer can be manipulated. This could be achieved by designing a device in which regions of low damping are controlled by spin currents. This highlights the bullet's potential for use within magnon-based or neuromorphic computing. Finally, the potential for realizing ultrafast current induced switching still exists within the CoFeB elements. The effect of varying the signal line width

and element size and shape has yet to be fully explored but may offer easier routes to single domain elements, and hence improved switching probability.

In conclusion, the injection of pure spin currents has been observed to drive a rich variety of fast magnetisation dynamics. Realizing active spintronic devices is a challenging task requiring precise techniques for both fabrication and measurement. While the fabrication of spintronic devices has not been carried out within this work, the results within this thesis should elucidate the impacts of choices made in device design and fabrication.

Bibliography

[1] M. Laver, *An Introduction to the Uses of Computers* (1976) (cited on page 43).

[2] M. N. Baibich, J. M. Broto, A. Fert, F. N. Van Dau, F. Petroff, P. Etienne, G. Creuzet, A. Friederich, and J. Chazelas, "Giant Magnetoresistance of (001)Fe/(001)Cr Magnetic Superlattices", Physical Review Letters **61**, 2472–2475 (1988) (cited on page 44).

[3] Nobel Media AB, *The 2007 Nobel Prize in Physics - Popular Information* (cited on pages 44, 60).

[4] Y. Shiroishi, K. Fukuda, I. Tagawa, H. Iwasaki, S. Takenoiri, H. Tanaka, H. Mutoh, and N. Yoshikawa, "Future Options for HDD Storage", IEEE Transactions on Magnetics **45**, 3816–3822 (2009) (cited on pages 44, 60, 97).

[5] T. Chen, R. K. Dumas, A. Eklund, P. K. Muduli, A. Houshang, A. A. Awad, P. Durrenfeld, B. G. Malm, A. Rusu, and J. Akerman, "Spin-Torque and Spin-Hall Nano-Oscillators", Proceedings of the IEEE **104**, 1919–1945 (2016) (cited on pages 44, 69, 97).

[6] A. V. Chumak, V. I. Vasyuchka, A. A. Serga, and B. Hillebrands, "Magnon spintronics", Nature Physics **11**, 453–461 (2015) (cited on pages 44, 70, 97, 110).

[7] B. I. Bleaney and B. Bleaney, *Electricity and Magnetism* (Oxford at the Clarendon Press, 1959) (cited on page 49).

[8] D. Dugdale, *Essentails of Electromagnetism* (The Macmillan Press Ltd, 1993) (cited on page 49).

[9] E. Dobbs, *Basic Electromagnetism* (Chapman & Hall, 1993) (cited on page 49).

[10] Richard Feynman, *The Feynman Lectures on Physics, Volume II* () (cited on page 50).

[11] W. F. Brown, "Micromagnetics, Domains, and Resonance", Journal of Applied Physics, 10.1063/1.2185970 (1959) (cited on page 51).

[12] A. Aharoni, *Introduction to the theory of ferromagnetism* (Oxfort University Press, 2000) (cited on pages 52, 56).

[13] E. W. Lee, "Magnetostriction and magnetomechanical effects", Reports on Progress in Physics **18**, 184–229 (1955) (cited on page 52).

[14] R. S. Alex Hubert, *Magnetic Domains* (1998) (cited on pages 52, 55–57, 59, 63, 80).

[15] A. H. Morrish, *The Physical Principles of Magnetism* (1965), pages 1–700 (cited on page 52).

[16] J. Stöhr and H. C. Siegmann, *Magnetism*, Vol. 7, Springer Series in Solid-State Sciences (Springer Berlin Heidelberg, Berlin, Heidelberg, 2006) (cited on pages 52, 57, 62, 64, 67, 95).

[17] J. Crangle, *The Magnetic Properties of Solids* (Edward Arnold, 1977) (cited on page 57).

[18] E. Schlömann, "Twisted domain wall structure in bubble films", Applied Physics Letters **21**, 227–229 (1972) (cited on page 59).

[19] T. H. O'Dell, "Magnetic bubble domain devices", Reports on Progress in Physics **49**, 589–620 (1986) (cited on page 59).

[20] V. V. Volkov and V. a. Bokov, "Domain wall dynamics in ferromagnets", Physics of the Solid State **50**, 199–228 (2008) (cited on page 59).

[21] V. L. Sobolev, "Internal structure of a domain wall in ultrathin magnetic film", Journal of Magnetism and Magnetic Materials **177-181**, 195–196 (1998) (cited on page 59).

[22] J. P. Tetienne, T. Hingant, L. J. Martínez, S. Rohart, A. Thiaville, L. H. Diez, K. Garcia, J. P. Adam, J. V. Kim, J. F. Roch, I. M. Miron, G. Gaudin, L. Vila, B. Ocker, D. Ravelosona, and V. Jacques, "The nature of domain walls in ultrathin ferromagnets revealed by scanning nanomagnetometry", Nature Communications **6**, 1–6 (2015) (cited on pages 59, 156).

[23] T. Spicer, *Adding Wide Field Imaging to a Scanning Kerr Microscope - Dissertation*, 2014 (cited on page 60).

[24] S. S. P. Parkin, M. Hayashi, and L. Thomas, "Magnetic domain-wall racetrack memory", Science **320**, 190–194 (2008) (cited on page 60).

[25] Griffiths J. H. E., "Anomalous High-frequency Resistance of Ferromagnetic Metals", Nature **158**, 670–671 (1946) (cited on page 60).

[26] C. Kittel, "On the theory of ferromagnetic resonance absorption", Physical Review **73**, 155–161 (1948) (cited on pages 60 sq.).

[27] A. G. Gurevich and G. A. Melkov, *Magnetization Oscillations and Waves* (CRC Press, 1996) (cited on pages 61 sq., 68).

[28] B. K. Pugh, D. P. Kramer, and C. H. Chen, "Demagnetizing factors for various geometries precisely determined using 3-D electromagnetic field simulation", IEEE Transactions on Magnetics **47**, 4100–4103 (2011) (cited on page 62).

[29] R. Damon and J. Eshbach, "Magnetostatic modes of a ferromagnet slab", Journal of Physics and Chemistry of Solids **19**, 308–320 (1961) (cited on page 62).

[30] T. Holstein and H. Primakoff, "Field Dependence of the Intrinsic Domain Magnetization of a Ferromagnet", Physical Review **58**, 1098–1113 (1940) (cited on page 62).

[31] A. Slavin and V. Tiberkevich, "Spin wave mode excited by spin-polarized current in a magnetic nanocontact is a standing self-localized wave bullet", Physical Review Letters **95**, 2–5 (2005) (cited on pages 63, 109).

[32]V. S. L'vov, *Wave Turbulence Under Parametric Excitation*, Springer Series in Nonlinear Dynamics (Springer Berlin Heidelberg, Berlin, Heidelberg, 1994) (cited on page 63).

[33]I. D. M. Giorgio Bertotti and C. Serpico, *Nonlinear Magnetization Dynamics in Nanosystems* (Elsevier, 2009) (cited on page 63).

[34]W. Thomson, "On the Electro-Dynamic Qualities of Metals:–Effects of Magnetization on the Electric Conductivity of Nickel and of Iron", Proceedings of the Royal Society of London **8**, 546–550 (1856) (cited on page 63).

[35]E. De Ranieri, a. W. Rushforth, K. Výborný, U. Rana, E. Ahmad, R. P. Campion, C. T. Foxon, B. L. Gallagher, a. C. Irvine, J. Wunderlich, and T. Jungwirth, "Lithographically and electrically controlled strain effects on anisotropic magnetoresistance in (Ga,Mn)As", New Journal of Physics **10**, 065003 (2008) (cited on page 63).

[36]M. Tsoi, a. Jansen, J. Bass, W.-C. Chiang, M. Seck, V. Tsoi, and P. Wyder, "Excitation of a Magnetic Multilayer by an Electric Current", Physical Review Letters **80**, 4281–4284 (1998) (cited on page 63).

[37]W. H. Rippard, M. R. Pufall, S. Kaka, S. E. Russek, and T. J. Silva, "Direct-current induced dynamics in Co90 Fe10/Ni80 Fe20 point contacts.", Physical Review letters **92**, 027201 (2004) (cited on page 63).

[38]M. D. Stiles and J. Miltat, "Spin-transfer torque and dynamics", Topics in Applied Physics **101**, 225–308 (2006) (cited on pages 63, 69).

[39]T. Jungwirth, J. Wunderlich, and K. Olejník, "Spin Hall effect devices", Nature Materials **11**, 382–390 (2012) (cited on pages 63, 70, 97).

[40]M. B. Shalom, C. W. Tai, Y. Lereah, M. Sachs, E. Levy, D. Rakhmilevitch, A. Palevski, and Y. Dagan, "Anisotropic magneto-transport effects at SrTiO3\LaAlO3 interfaces", Physical Review B **80**, 140403 (2009) (cited on page 63).

[41]T. McGuire and R. Potter, "Anisotropic magnetoresistance in ferromagnetic 3d alloys", IEEE Transactions on Magnetics **11**, 1018–1038 (1975) (cited on page 64).

[42]J. Nickel, "Magnetoresistance Overview", HP Labs Technical Reports, HPL–95–60 (1995) (cited on page 64).

[43]Z. H. Xiong, D. Wu, Z. Valy Vardeny, and J. Shi, "Giant magnetoresistance in organic spin-valves", Nature **427**, 821–824 (2004) (cited on page 64).

[44]J. S. Moodera, L. R. Kinder, T. M. Wong, and R. Meservey, "Large Magnetoresistance at Room Temperature in Ferromagnetic Thin Film Tunnel Junctions", Physical Review Letters **74**, 3273–3276 (1995) (cited on page 64).

[45]E. H. Hall, "On a New Action of the Magnet on Electric Currents", American Journal of Mathematics **2**, 287 (1879) (cited on page 64).

[46]E. H. Hall, "On the "Rotational Coefficient" in Nickel and Cobalt", Proceedings of the Physical Society of London **4**, 325–342 (1880) (cited on page 64).

[47]N. Nagaosa, J. Sinova, S. Onoda, A. H. MacDonald, and N. P. Ong, "Anomalous Hall effect", Reviews of Modern Physics **82**, 1539–1592 (2010) (cited on pages 64 sq., 67).

[48]M. I. D'yakonov and V. I. Perel', "Possibility of orienting electron spins with current", JETP Letters **13**, 467–469 (1971) (cited on page 64).

[49]J. E. Hirsch, "Spin Hall effect", Phys. Rev. Lett. **83**, 1834 (1999) (cited on pages 65, 97).

[50]Y. K. Kato, R. C. Myers, a. C. Gossard, and D. D. Awschalom, "Observation of the spin Hall effect in semiconductors.", Science **306**, 1910–1913 (2004) (cited on pages 65, 91, 97).

[51]J. Wunderlich, B. Kaestner, J. Sinova, and T. Jungwirth, "Experimental Observation of the Spin-Hall Effect in a Two-Dimensional Spin-Orbit Coupled Semiconductor System", Physical Review Letters **94**, 047204 (2005) (cited on page 65).

[52]A. Hoffmann, "Spin Hall Effects in Metals", IEEE Transactions on Magnetics **49**, 5172–5193 (2013) (cited on pages 65 sq., 70, 97).

[53]C.-F. Pai, L. Liu, Y. Li, H. W. Tseng, D. C. Ralph, and R. a. Buhrman, "Spin transfer torque devices utilizing the giant spin Hall effect of tungsten", Applied Physics Letters **101**, 122404 (2012) (cited on page 65).

[54]G. Y. Guo, S. Murakami, T. W. Chen, and N. Nagaosa, "Intrinsic spin hall effect in platinum: First-principles calculations", Physical Review Letters **100**, 10.1103/PhysRevLett.100.096401 (2008) (cited on page 66).

[55]Y. A. Bychkov and E. I. Rashba, "Oscillatory Effects And the Magnetic-Susceptibility Of Carriers In Inversion-Layers", Journal Of Physics C-Solid State Physics **17**, 6039–6045 (1984) (cited on page 67).

[56]A. Manchon, H. C. Koo, J. Nitta, S. M. Frolov, and R. A. Duine, "New perspectives for Rashba spin-orbit coupling", Nature Materials **14**, 871–882 (2015) (cited on page 67).

[57]C. Song, B. Cui, F. Li, X. Zhou, and F. Pan, "Recent progress in voltage control of magnetism: Materials, mechanisms, and performance", Progress in Materials Science **87**, 33–82 (2017) (cited on page 68).

[58]L. Berger, "Emission of spin waves by a magnetic multilayer traversed by a current", Physical Review B **54**, 9353–9358 (1996) (cited on page 68).

[59]J. Slonczewski, "Current-driven excitation of magnetic multilayers", Journal of Magnetism and Magnetic Materials **159**, L1–L7 (1996) (cited on page 68).

[60]M. D. Stiles and A. Zangwill, "Anatomy of spin-transfer torque", Physical Review B **66**, 014407 (2002) (cited on page 68).

[61]A. Brataas, A. D. Kent, and H. Ohno, "Current-induced torques in magnetic materials", Nature Materials **11**, 372–381 (2012) (cited on pages 68, 70, 98).

[62]R. Dumas, S. Sani, S. Mohseni, E. Iacocca, Y. Pogoryelov, P. Muduli, S. Chung, P. Durrenfeld, and J. Akerman, "Recent Advances in Nanocontact Spin-Torque Oscillators", IEEE Transactions on Magnetics **50**, 1–7 (2014) (cited on pages 69, 98).

[63]a. a. Tulapurkar, Y. Suzuki, A. Fukushima, H. Kubota, H. Maehara, K. Tsunekawa, D. D. Djayaprawira, N. Watanabe, and S. Yuasa, “Spin-torque diode effect in magnetic tunnel junctions”, Nature **438**, 339–342 (2005) (cited on pages 71 sq., 74, 98).

[64]J. C. Sankey, P. M. Braganca, a. G. F. Garcia, I. N. Krivorotov, R. a. Buhrman, and D. C. Ralph, “Spin-Transfer-Driven Ferromagnetic Resonance of Individual Nanomagnets”, Physical Review Letters **96**, 227601 (2006) (cited on page 71).

[65]H. Kubota, A. Fukushima, K. Yakushiji, T. Nagahama, S. Yuasa, K. Ando, H. Maehara, Y. Nagamine, K. Tsunekawa, D. D. Djayaprawira, N. Watanabe, and Y. Suzuki, “Quantitative measurement of voltage dependence of spin-transfer torque in MgO-based magnetic tunnel junctions”, Nature Physics **4**, 37–41 (2008) (cited on pages 71, 98).

[66]L. Liu, T. Moriyama, D. C. Ralph, and R. A. Buhrman, “Spin-Torque Ferromagnetic Resonance Induced by the Spin Hall Effect”, Physical Review Letters **106**, 036601 (2011) (cited on pages 71 sq., 98, 113).

[67]J. C. Sankey, Y.-T. Cui, J. Z. Sun, J. C. Slonczewski, R. a. Buhrman, and D. C. Ralph, “Measurement of the spin-transfer-torque vector in magnetic tunnel junctions”, Nature Physics **4**, 67–71 (2008) (cited on pages 73, 98).

[68]M. Faraday, “Experimental Researches in Electricity. Fifth Series”, Philosophical Transactions of the Royal Society of London **123**, 675–710 (1833) (cited on page 80).

[69]J. Kerr, “On the Rotation of the Plane of Polarization of Light by Reflection from the Pole of a Magnet”, Proceedings of the Royal Society of London **25**, 447–450 (1876) (cited on page 80).

[70]H. Williams, F. Foster, and E. Wood, “Obervation of Magnetic Domains by the Kerr Effect”, Letters to the Editor, 119–120 (1951) (cited on page 80).

[71]J. McCord, “Progress in magnetic domain observation by advanced magneto-optical microscopy”, Journal of Physics D: Applied Physics **48**, 333001 (2015) (cited on pages 80 sq.).

[72]P. S. Keatley, “Time-Resolved Magneto-Optical Investigations of Picosecond Magnetisation Dynamics in Arrays of Non-Ellipsoidal Ferromagnetic Nano-Elements”, PhD thesis (2008) (cited on pages 85, 91).

[73]S. O. Demokritov and V. E. Demidov, “Micro-brillouin light scattering spectroscopy of magnetic nanostructures”, IEEE Transactions on Magnetics **44**, 6–12 (2008) (cited on pages 90, 110).

[74]J. Raabe, C. Quitmann, C. H. Back, F. Nolting, S. Johnson, and C. Buehler, “Quantitative analysis of magnetic excitations in landau flux-closure structures using synchrotron-radiation microscopy”, Physical Review Letters **94**, 1–4 (2005) (cited on page 90).

[75]M. E. Re and M. H. Kryder, “Magneto-optic investigation of thin-film recording heads”, Journal of Applied Physics **55**, 2245 (1984) (cited on page 91).

[76] P. Gangmei, P. S. Keatley, W. Yu, R. J. Hicken, M. a. Gubbins, P. J. Czoschke, and R. Lopusnik, "Time- and vector-resolved Kerr microscopy of hard disk writers", Applied Physics Letters **99**, 2009–2012 (2011) (cited on pages 91, 111).

[77] J. Fidler and T. Schrefl, "Micromagnetic modelling - the current state of the art", Journal of Physics D: Applied Physics **33**, R135–R156 (2000) (cited on page 91).

[78] J. Leliaert, M. Dvornik, J. Mulkers, J. De Clercq, M. V. Milošević, and B. Van Waeyenberge, "Fast micromagnetic simulations on GPU—recent advances made with MuMax3", Journal of Physics D: Applied Physics **51**, 123002 (2018) (cited on page 91).

[79] R. F. L. Evans, R. W. Chantrell, G. Han, G.-m. Chow, and J. Chen, "Atomistic Modeling of the Interlayer Coupling Behavior in Perpendicularly -FePt/Ag/ -FePt Pseudo Spin Valves Magnetized", **47**, 2646–2648 (2011) (cited on page 91).

[80] R. F. Evans, W. J. Fan, P. Chureemart, T. A. Ostler, M. O. Ellis, and R. W. Chantrell, "Atomistic spin model simulations of magnetic nanomaterials", Journal of Physics Condensed Matter **26**, 10.1088/0953-8984/26/10/103202 (2014) (cited on page 91).

[81] A. Vansteenkiste, J. Leliaert, M. Dvornik, M. Helsen, F. Garcia-Sanchez, and B. Van Waeyenberge, "The design and verification of MuMax3", AIP Advances **4**, 107133 (2014) (cited on pages 91, 117, 119).

[82] COMSOL Inc, *Introduction to COMSOL Multiphysics 5.2a* (2016) (cited on pages 93, 99, 117).

[83] M. Abbasi, B. Wang, S. Tamaru, H. Kubota, A. Fukushima, and D. S. Ricketts, "Accurate De-Embedding and Measurement of Spin-Torque Oscillators", IEEE Transactions on Magnetics **53**, 10.1109/TMAG.2017.2752004 (2017) (cited on page 94).

[84] R. M. Tromp, J. B. Hannon, a. W. Ellis, W. Wan, a. Berghaus, and O. Schaff, "Ultramicroscopy A new aberration-corrected , energy-filtered LEEM / PEEM instrument . I . Principles and design", Ultramicroscopy **110**, 1–10 (2010) (cited on page 95).

[85] A. Locatelli and E. Bauer, "Recent advances in chemical and magnetic imaging of surfaces and interfaces by XPEEM", Journal of Physics: Condensed Matter **20**, 093002 (2008) (cited on page 95).

[86] R. M. Tromp, J. B. Hannon, W. Wan, A. Berghaus, and O. Schaff, "A new aberration-corrected, energy-filtered LEEM/PEEM instrument II. Operation and results", Ultramicroscopy **127**, 25–39 (2013) (cited on page 95).

[87] R. van Gastel, I. Sikharulidze, S. Schramm, J. P. Abrahams, B. Poelsema, R. M. Tromp, and S. J. van der Molen, "Medipix 2 detector applied to low energy electron microscopy", Ultramicroscopy **110**, 33–35 (2009) (cited on page 96).

[88] J. Grollier, D. Querlioz, and M. D. Stiles, "Spintronic Nanodevices for Bioinspired Computing", Proceedings of the IEEE **104**, 2024–2039 (2016) (cited on page 97).

[89] M. Ranjbar, P. Durrenfeld, M. Haidar, E. Iacocca, M. Balinskiy, T. Q. Le, M. Fazlali, A. Houshang, A. A. Awad, R. K. Dumas, and J. Akerman, "CoFeB-Based Spin Hall Nano-Oscillators", IEEE Magnetics Letters **5**, 1–4 (2014) (cited on pages 97, 110).

[90] P. Dürrenfeld, F. Gerhard, M. Ranjbar, C. Gould, L. W. Molenkamp, and J. Åkerman, "Spin Hall effect-controlled magnetization dynamics in NiMnSb", Journal of Applied Physics **117**, 17E103 (2015) (cited on pages 97 sq., 110).

[91] H. Mazraati, S. Chung, A. Houshang, M. Dvornik, L. Piazza, F. Qejvanaj, S. Jiang, T. Q. Le, J. Weissenrieder, and J. Åkerman, "Low operational current spin Hall nano-oscillators based on NiFe/W bilayers", Applied Physics Letters **109**, 242402 (2016) (cited on pages 97, 110).

[92] M. Zahedinejad, H. Mazraati, H. Fulara, J. Yue, S. Jiang, A. A. Awad, and J. Åkerman, "CMOS compatible W/CoFeB/MgO spin Hall nano-oscillators with wide frequency tunability", arXiv Applied Physics, 1–6 (2018) (cited on pages 97, 110).

[93] A. Hamadeh, O. d'Allivy Kelly, C. Hahn, H. Meley, R. Bernard, A. H. Molpeceres, V. V. Naletov, M. Viret, A. Anane, V. Cros, S. O. Demokritov, J. L. Prieto, M. Muñoz, G. de Loubens, and O. Klein, "Full Control of the Spin-Wave Damping in a Magnetic Insulator Using Spin-Orbit Torque", Physical Review Letters **113**, 197203 (2014) (cited on pages 97, 110).

[94] M. Dvornik, A. A. Awad, and J. Åkerman, "Origin of Magnetization Auto-Oscillations in Constriction-Based Spin Hall Nano-Oscillators", Physical Review Applied **9**, 014017 (2018) (cited on pages 97, 110).

[95] V. E. Demidov, S. Urazhdin, H. Ulrichs, V. Tiberkevich, A. Slavin, D. Baither, G. Schmitz, and S. O. Demokritov, "Magnetic nano-oscillator driven by pure spin current", Nature Materials **11**, 1028–31 (2012) (cited on pages 98, 108, 110).

[96] A. A. Awad, P. Dürrenfeld, A. Houshang, M. Dvornik, E. Iacocca, R. K. Dumas, and J. Åkerman, "Long-range mutual synchronization of spin Hall nano-oscillators", Nature Physics **13**, 292–299 (2016) (cited on page 98).

[97] V. E. Demidov, S. Urazhdin, A. Zholud, A. V. Sadovnikov, and S. O. Demokritov, "Nanoconstriction-based spin-Hall nano-oscillator", Applied Physics Letters **105**, 172410 (2014) (cited on pages 98, 110).

[98] R. H. Liu, W. L. Lim, and S. Urazhdin, "Spectral characteristics of the microwave emission by the spin hall nano-oscillator", Physical Review Letters **110**, 147601 (2013) (cited on pages 98, 102, 110, 113, 119).

[99] V. E. Demidov, H. Ulrichs, S. V. Gurevich, S. O. Demokritov, V. S. Tiberkevich, a. N. Slavin, A. Zholud, and S. Urazhdin, "Synchronization of spin Hall nano-oscillators to external microwave signals.", Nature communications **5**, 3179 (2014) (cited on pages 98, 108, 114, 124).

[100] H. Ulrichs, V. E. Demidov, and S. O. Demokritov, "Micromagnetic study of auto-oscillation modes in spin-Hall nano-oscillators", Applied Physics Letters **104**, 042407 (2014) (cited on pages 98, 110, 113, 119).

[101] T. D. Skinner, M. Wang, A. T. Hindmarch, A. W. Rushforth, A. C. Irvine, D. Heiss, H. Kurebayashi, and A. J. Ferguson, "Spin-orbit torque opposing the Oersted torque in ultrathin Co/Pt bilayers", Applied Physics Letters **104**, 062401 (2014) (cited on pages 98, 127).

[102] S. S. Kalarickal, P. Krivosik, M. Wu, C. E. Patton, M. L. Schneider, P. Kabos, T. J. Silva, and J. P. Nibarger, "Ferromagnetic resonance linewidth in metallic thin films: Comparison of measurement methods", Journal of Applied Physics **99**, 10.1063/1.2197087 (2006) (cited on page 98).

[103] S. Emori, U. Bauer, S.-M. Ahn, E. Martinez, and G. S. D. Beach, "Current-driven dynamics of chiral ferromagnetic domain walls", Nature Materials **12**, 611–616 (2013) (cited on pages 99, 156).

[104] P. Dürrenfeld, "Spin Torque and Spin Hall Nano-Oscillators with Single Magnetic Layers", PhD thesis () (cited on pages 101, 108).

[105] T. M. Spicer, P. S. Keatley, M. Dvornik, T. H. J. Loughran, A. A. Awad, P. Dürrenfeld, A. Houshang, M. Ranjbar, J. Åkerman, V. V. Kruglyak, and R. J. Hicken, "Time resolved imaging of the non-linear bullet mode within an injection-locked nano-contact spin Hall nano-oscillator", Applied Physics Letters **113**, 192405 (2018) (cited on page 108).

[106] Chia-Nan Chang, Yu-Ching Wong, and Chun Hsiung Chen, "Full-wave analysis of coplanar waveguides by variational conformal mapping technique", IEEE Transactions on Microwave Theory and Techniques **38**, 1339–1344 (1990) (cited on page 108).

[107] E. Carlsson and S. Gevorgian, "Effect of enhanced current crowding in a CPW with a thin ferroelectric film", Electronics Letters **33**, 145 (1997) (cited on page 108).

[108] E. Carlsson and S. Gevorgian, "Conformal mapping of the field and charge distributions in multilayered substrate CPWs", IEEE Transactions on Microwave Theory and Techniques **47**, 1544–1552 (1999) (cited on page 108).

[109] Y. Silberberg, "Collapse of optical pulses", Optics Letters **15**, 1282 (1990) (cited on page 110).

[110] A. Giordano, M. Carpentieri, A. Laudani, G. Gubbiotti, B. Azzerboni, and G. Finocchio, "Spin-Hall nano-oscillator: A micromagnetic study", Applied Physics Letters **105**, 042412 (2014) (cited on pages 110 sq., 119).

[111] M. Zahedinejad, A. A. Awad, P. Durrenfeld, A. Houshang, Y. Yin, P. K. Muduli, and J. Akerman, "Current Modulation of Nanoconstriction Spin-Hall Nano-Oscillators", IEEE Magnetics Letters **8**, 1–4 (2017) (cited on page 110).

[112] T. Kendziorczyk and T. Kuhn, "Mutual synchronization of nanoconstriction-based spin Hall nano-oscillators through evanescent and propagating spin waves", Physical Review B - Condensed Matter and Materials Physics **93**, 1–6 (2016) (cited on page 110).

[113] B. Divinskiy, V. E. Demidov, A. Kozhanov, A. B. Rinkevich, S. O. Demokritov, and S. Urazhdin, "Nanoconstriction spin-Hall oscillator with perpendicular magnetic anisotropy", Applied Physics Letters **111**, 10.1063/1.4993910 (2017) (cited on page 110).

[114]R. A. J. Valkass, T. M. Spicer, E. Burgos Parra, R. J. Hicken, M. A. Bashir, M. A. Gubbins, P. J. Czoschke, and R. Lopusnik, "Time-resolved scanning Kerr microscopy of flux beam formation in hard disk write heads", Journal of Applied Physics **119**, 233903 (2016) (cited on page 111).

[115]P. S. Keatley, S. R. Sani, G. Hrkac, S. M. Mohseni, P. Dürrenfeld, J. Åkerman, and R. J. Hicken, "Imaging magnetisation dynamics in nano-contact spin-torque vortex oscillators exhibiting gyrotropic mode splitting", Journal of Physics D: Applied Physics **50**, 164003 (2017) (cited on page 112).

[116]P. S. Keatley, V. V. Kruglyak, R. J. Hicken, J. R. Childress, and J. A. Katine, "Acquisition of vector hysteresis loops from micro-arrays of nano-magnets", Journal of Magnetism and Magnetic Materials **306**, 298–301 (2006) (cited on page 122).

[117]S. Ikeda, J. Hayakawa, Y. M. Lee, F. Matsukura, Y. Ohno, T. Hanyu, and H. Ohno, "Magnetic Tunnel Junctions for Spintronic Memories and Beyond", IEEE Transactions on Electron Devices **54**, 991–1002 (2007) (cited on page 127).

[118]M. Julliere, "Tunneling between ferromagnetic films", Physics Letters A **54**, 225–226 (1975) (cited on page 127).

[119]M. Tsoi, "Magnetic tunnel junctions: Spin-torque measured up", Nature Physics **4**, 17–18 (2008) (cited on page 127).

[120]S. Ikeda, K. Miura, H. Yamamoto, K. Mizunuma, H. D. Gan, M. Endo, S. Kanai, J. Hayakawa, F. Matsukura, and H. Ohno, "A perpendicular-anisotropy CoFeB–MgO magnetic tunnel junction", Nature Materials **9**, 721–724 (2010) (cited on pages 127 sq.).

[121]D. C. Worledge, G. Hu, D. W. Abraham, J. Z. Sun, P. L. Trouilloud, J. Nowak, S. Brown, M. C. Gaidis, E. J. O'Sullivan, and R. P. Robertazzi, "Spin torque switching of perpendicular Ta/CoFeB/MgO-based magnetic tunnel junctions", Applied Physics Letters **98**, 022501 (2011) (cited on page 127).

[122]I. M. Miron, K. Garello, G. Gaudin, P.-J. Zermatten, M. V. Costache, S. Auffret, S. Bandiera, B. Rodmacq, A. Schuhl, and P. Gambardella, "Perpendicular switching of a single ferromagnetic layer induced by in-plane current injection", Nature **476**, 189–193 (2011) (cited on pages 127 sq.).

[123]L. Liu, C.-F. Pai, Y. Li, H. W. Tseng, D. C. Ralph, and R. A. Buhrman, "Spin-Torque Switching with the Giant Spin Hall Effect of Tantalum", Science **336**, 555–558 (2012) (cited on page 127).

[124]X. Fan, J. Wu, Y. Chen, M. J. Jerry, H. Zhang, and J. Q. Xiao, "Observation of the nonlocal spin-orbital effective field", Nature Communications **4**, 1799 (2013) (cited on page 127).

[125]G. Yu, P. Upadhyaya, K. L. Wong, W. Jiang, J. G. Alzate, J. Tang, P. K. Amiri, and K. L. Wang, "Magnetization switching through spin-Hall-effect-induced chiral domain wall propagation", Physical Review B **89**, 104421 (2014) (cited on pages 127, 132, 160).

[126]G. Yu, P. Upadhyaya, Y. Fan, J. G. Alzate, W. Jiang, K. L. Wong, S. Takei, S. A. Bender, L.-T. Chang, Y. Jiang, M. Lang, J. Tang, Y. Wang, Y. Tserkovnyak, P. K. Amiri, and K. L. Wang, "Switching of perpendicular magnetization by spin–orbit torques in the absence of external magnetic fields", Nature Nanotechnology **9**, 548–554 (2014) (cited on page 127).

[127]K.-S. Lee, S.-W. Lee, B.-c. Min, and K.-j. Lee, "Thermally activated switching of perpendicular magnet by spin-orbit spin torque", Applied Physics Letters **104**, 072413 (2014) (cited on pages 127, 133).

[128]S. Fukami and H. Ohno, "Magnetization switching schemes for nanoscale three-terminal spintronics devices", Japanese Journal of Applied Physics **56**, 10.7567/JJAP.56.0802A1 (2017) (cited on page 127).

[129]T. Suzuki, S. Fukami, N. Ishiwata, M. Yamanouchi, S. Ikeda, N. Kasai, and H. Ohno, "Current-induced effective field in perpendicularly magnetized Ta/CoFeB/MgO wire", Applied Physics Letters **98**, 1–4 (2011) (cited on page 128).

[130]J. Kim, J. Sinha, M. Hayashi, M. Yamanouchi, S. Fukami, T. Suzuki, S. Mitani, and H. Ohno, "Layer thickness dependence of the current-induced effective field vector in Ta/CoFeB/MgO", Nature Materials **12**, 240–245 (2012) (cited on page 128).

[131]C. Zhang, M. Yamanouchi, H. Sato, S. Fukami, S. Ikeda, F. Matsukura, and H. Ohno, "Magnetotransport measurements of current induced effective fields in Ta/CoFeB/MgO", Applied Physics Letters **103**, 1–4 (2013) (cited on page 128).

[132]K. Garello, I. M. Miron, C. O. Avci, F. Freimuth, Y. Mokrousov, S. Blügel, S. Auffret, O. Boulle, G. Gaudin, and P. Gambardella, "Symmetry and magnitude of spin–orbit torques in ferromagnetic heterostructures", Nature Nanotechnology **8**, 587–593 (2013) (cited on page 128).

[133]C. O. Avci, K. Garello, C. Nistor, S. Godey, B. Ballesteros, A. Mugarza, A. Barla, M. Valvidares, E. Pellegrin, A. Ghosh, I. M. Miron, O. Boulle, S. Auffret, G. Gaudin, and P. Gambardella, "Fieldlike and antidamping spin-orbit torques in as-grown and annealed Ta/CoFeB/MgO layers", Physical Review B - Condensed Matter and Materials Physics **89**, 1–13 (2014) (cited on page 128).

[134]C. Zhang, S. Fukami, H. Sato, F. Matsukura, and H. Ohno, "Spin-orbit torque induced magnetization switching in nano-scale Ta/CoFeB/MgO", Applied Physics Letters **107**, 012401 (2015) (cited on pages 128, 143).

[135]X. Qiu, P. Deorani, K. Narayanapillai, K.-S. Lee, K.-J. Lee, H.-W. Lee, and H. Yang, "Angular and temperature dependence of current induced spin-orbit effective fields in Ta/CoFeB/MgO nanowires", Scientific Reports **4**, 4491 (2015) (cited on page 128).

[136]J. Torrejon, F. Garcia-Sanchez, T. Taniguchi, J. Sinha, S. Mitani, J.-V. Kim, and M. Hayashi, "Current-driven asymmetric magnetization switching in perpendicularly magnetized CoFeB/MgO heterostructures", Physical Review B **91**, 214434 (2015) (cited on page 128).

[137]C. J. Durrant, R. J. Hicken, Q. Hao, and G. Xiao, "Scanning Kerr microscopy study of current-induced switching in Ta/CoFeB/MgO films with perpendicular magnetic anisotropy", Physical Review B **93**, 014414 (2016) (cited on pages 129, 132, 134, 160).

[138]Q. Hao and G. Xiao, "Giant spin Hall effect and magnetotransport in a Ta/CoFeB/MgO layered structure: A temperature dependence study", Physical Review B - Condensed Matter and Materials Physics **91**, 1–8 (2015) (cited on pages 129, 133, 135).

[139]L. F. Shampine and M. W. Reichelt, "The MATLAB ODE Suite", SIAM Journal on Scientific Computing **18**, 1–22 (1997) (cited on page 130).

[140]J. Cao, Y. Chen, T. Jin, W. Gan, Y. Wang, Y. Zheng, H. Lv, S. Cardoso, D. Wei, and W. S. Lew, "Spin orbit torques induced magnetization reversal through asymmetric domain wall propagation in Ta/CoFeB/MgO structures", Scientific Reports **8**, 1–9 (2018) (cited on pages 132, 143, 156, 160).

[141]J. Torrejon, J. Kim, J. Sinha, S. Mitani, M. Hayashi, M. Yamanouchi, and H. Ohno, "Interface control of the magnetic chirality in CoFeB/MgO heterostructures with heavy-metal underlayers", Nature Communications **5**, 1–8 (2014) (cited on pages 132, 156).

[142]I. Gross, L. J. Martínez, J. P. Tetienne, T. Hingant, J. F. Roch, K. Garcia, R. Soucaille, J. P. Adam, J. V. Kim, S. Rohart, A. Thiaville, J. Torrejon, M. Hayashi, and V. Jacques, "Direct measurement of interfacial Dzyaloshinskii-Moriya interaction in X|CoFeB|MgO heterostructures with a scanning NV magnetometer (X=Ta,TaN, and W) DIRECT MEASUREMENT of INTERFACIAL ... I. GROSS et al.", Physical Review B **94**, 1–8 (2016) (cited on pages 132, 156).

[143]X. Fan, A. R. Mellnik, W. Wang, N. Reynolds, T. Wang, H. Celik, V. O. Lorenz, D. C. Ralph, and J. Q. Xiao, "All-optical vector measurement of spin-orbit-induced torques using both polar and quadratic magneto-optic Kerr effects", Applied Physics Letters **109**, 122406 (2016) (cited on page 133).

[144]T. M. Crawford, P. Kabos, and T. J. Silva, "Coherent control of precessional dynamics in thin film permalloy", Applied Physics Letters **76**, 2113–2115 (2000) (cited on page 134).

[145]M. Bauer, R. Lopusnik, J. Fassbender, and B. Hillebrands, "Suppression of magnetic-field pulse-induced magnetization precession by pulse tailoring", Applied Physics Letters **76**, 2758–2760 (2000) (cited on page 134).

[146]M. Kazemi, G. E. Rowlands, S. Shi, R. A. Buhrman, and E. G. Friedman, "All-Spin-Orbit Switching of Perpendicular Magnetization", IEEE Transactions on Electron Devices **63**, 4499–4505 (2016) (cited on page 135).

[147]M. M. Decker, M. S. Wörnle, A. Meisinger, M. Vogel, H. S. Körner, G. Y. Shi, C. Song, M. Kronseder, and C. H. Back, "Time Resolved Measurements of the Switching Trajectory of Pt/Co Elements Induced by Spin-Orbit Torques", Physical Review Letters **118**, 1–5 (2017) (cited on pages 135, 143, 160).

[148]G. E. Rowlands, S. V. Aradhya, S. Shi, E. H. Yandel, J. Oh, D. C. Ralph, and R. A. Buhrman, “Nanosecond magnetization dynamics during spin Hall switching of in-plane magnetic tunnel junctions”, Applied Physics Letters **110**, 10.1063/1.4978661 (2017) (cited on page 143).

[149]C. J. Durrant, “Magnetisation Dynamics of Nanostructured Spintronic Devices”, PhD thesis (2016) (cited on pages 145, 147, 149, 151 sq., 154 sq., 157 sq.).

[150]I. Dzyaloshinsky, “A thermodynamic theory of “weak” ferromagnetism of antiferromagnetics”, Journal of Physics and Chemistry of Solids **4**, 241–255 (1958) (cited on page 156).

[151]T. Moriya, “Anisotropic Superexchange Interaction and Weak Ferromagnetism”, Physical Review **120**, 91–98 (1960) (cited on page 156).

[152]S. Shi, Y. Ou, S. V. Aradhya, D. C. Ralph, and R. A. Buhrman, “Fast low-current spin-orbit-torque switching of magnetic tunnel junctions through atomic modifications of the free-layer interfaces”, Physical Review Applied **9**, 11002 (2018) (cited on page 160).